Cardiff University
School of Psychology

Thesis submitted for the degree of
Doctor of Philosophy 2023

Diffusion MRI of the prostate at 300 mT/m

Malwina Molendowska, MSc, BSc
Supervised by Chantal M. W. Tax, PhD, Prof. Derek K. Jones,
Fabrizio Fasano

Cardiff, Wales, 2023

Contents

Po: Maybe I should just quit and go back to making noodles.

Oogway: Quit, don't quit... Noodles, don't noodles... You are too concerned about what was and what will be. There is a saying: yesterday is history, tomorrow is a mystery, but today is a gift. That is why it is called the *'present'*.

Kung Fu Panda

Abstract

Diffusion magnetic resonance imaging gained worldwide recognition as the chief non-invasive mean of mapping microstructural properties of biological tissue. By far, the most common clinical application of this method is diagnosing conditions such as stroke and cancer.

Prostate cancer is one of the leading cancer-related causes of deaths among men. Recently, MRI became a triage test in the diagnostic pathway for men suspected of having prostate cancer. While providing a very useful contrast, limited gradient power of clinical MR hardware prevents it from capturing the whole range of microstructural changes. For that reason, one research priority is to provide novel MRI-based biomarkers for increased efficacy of its early diagnosis. Assessing early microstructural changes in the prostate is of fundamental importance, as it can increase patients' chance of survival.

Novel technological developments can be used when trying to address the issues with limited spatial resolution, sensitivity and specificity of the clinical MRI scans. The work presented in this thesis focused on the use of one of the most powerful whole-body MRI scanners - in terms of the gradient amplitude - available worldwide to advance diffusion MRI of the prostate. Advanced image reconstruction, accounting for MR field perturbations, was exploited to address concerns regarding low image quality resulting from limited MR gradient fidelity. In addition, diffusion MRI was probed at sub-millimetre spatial resolution and effectively enhanced spatial resolution of the images which is crucial for accurate localisation of cancerous lesions.

The work presented in this thesis showcases the ways to obtain higher spatial resolution, and boosted signal-to-noise ratio in diffusion MRI images of the prostate, as well as increased sensitivity to subtle tissue alterations that can be observed early in prostate cancer. The preliminary results are promising, but further development of methods is required, including exploring more advanced microstructural imaging sequences and methods for analysing the data they allow to obtain.

Publications arising from this Thesis

- **Chapter 4** has been published as a technical note in *Magnetic Resonance in Medicine*

  Molendowska, M., Fasano, F., Rudrapatna, U., Kimmlingen, R., Jones, D. K., Kusmia, S., Tax, C. M. W. & Evans, C. J. (2022). Physiological effects of human body imaging with 300 mT/m gradients. Magnetic Resonance in Medicine, 87(5), 2512-2520.

- **Chapter 5** is about to be submitted as a original research manuscript to *Journal of Magnetic Resonance Imaging.*

- **Chapter 6** is about to be submitted as a original research manuscript to *Magnetic Resonance in Medicine.*

  In addition, the author was invited by the editor of the Siemens Healthineers journal *MAGNETOM Flash*, to write a manuscript summarising research presented in this work.

First and foremost, I would like to express my sincere gratitude to my supervisory team: Dr. Chantal Tax, Prof. Derek Jones, and Fabrizio Fasano for giving me the opportunity to work on this exciting project. Your expertise, encouragement, motivation and optimism were fundamental in the process of research that led to writing this thesis.

I would like to extend my appreciation to my collaborators in the clinic and thank them for the help with recruiting the patients.

I was extremely lucky to have a chance to work with Lars Müller and Maria Engel. Thank you for taking me on the adventurous road trip of sequence development and data reconstruction, flavoured with a fairly decent amount of cookies and cakes. Most of all, I am very grateful for your tireless support and patience in answering my countless questions.

I want to express my deep appreciation to Alexis Reymbaut, for always being there when I needed help, whether it was a personal or work-related struggle.

I would like to thank my Welsh family, who have welcomed me and taken care of me for over almost four years. I have never felt so much a part of a family, outside my own.

I would also like to give special thanks to the members of the 'Three Musketeers' group: Matteo Mancini, Marco Palombo, and Emre Kopanoglu, who brightened up many of the rainy and cloudy days in Wales. Without your uncanny insights into research and life I would not have grown so much. Grazie mille to M&Ms for teaching me how to be more Italian and how to properly do the 'pinecone' hand. Teşekkür ederim to Emre, for picking up on my 'Friends' references, and many intriguing nerdy chats. Guys, I will remember our comic situations *forever*. *Enkosi!*

Thanks to all past and current colleagues in and outside the CUBRIC: Elena Kleban (& Frank), Elisa Marchetto, Greg Parker, Andrew Morris, Andre Döring, Garin Hughes, John Evans, Carolyn McNabb (& Amar, Lewis), James Gholam, Katherine Blanter, Maëliss Jallais, Kadir Şimşek and many others, for countless chats, as well as standing by my side and encouraging me to move forward even in the darkest moments. I consider myself very lucky to have had the opportunity to be a part of the CUBRIC community. Diloch!

I also want to thank a bunch of my Polish friends, especially Agnieszka Rajca and Patryk Arsany, for their perpetual encouragement and for always helping me to believe in myself by believing in me.

Special thanks to Siemens Healthineers for funding this studentship which allowed me to have the opportunity to play with this special scanner and for giving me the technical support. Additional thanks to Skope for the support needed with running your instrumentation alongside the MR system.

Finally, endless love and gratitude to my parents, and my closest family.

Mamo, tato, siostro, najbliższa rodzino, dziękuję Wam za nauczenie mnie pasji, ambicji, wytrwałości, pokory i za wiarę we mnie. Bez tego ukończenie tej pracy nie byłoby możliwe.

Malwina Molendowska

Cardiff, Wales, United Kingdom, 10.02.2023

List of abbreviations

For the convenience of readers we collect below the various abbreviations employed in the manuscript.

2D	–	two-dimensional,
ADC	–	Apparent Diffusion Coefficient,
b-value	–	diffusion sensitizing parameter,
BW	–	bandwidth,
csPCa	–	clinically significant prostate cancer,
CoV	–	Coefficient of Variation,
CZ	–	central zone of the prostate,
dMRI	–	diffusion-weighted Magnetic Resonance Imaging,
DTI	–	Diffusion Tensor Imaging,
DTD	–	Diffusion Tensor Distribution,
EPI	–	Echo Planar Imaging,
FA	–	Fractional Anisotropy,
FFT	–	Fast Fourier Transform,
FID	–	Free Induction Decay,
FOV	–	Field Of View,
GRAPPA	–	GeneRalized Autocalibrating Partially Parallel Acquisition,
GRE	–	Gradient Echo,
GIRF	–	Gradient Impulse Response Function,
GNL	–	gradient non-linearities,
GS	–	Gleason Score,
k-space	–	spatial-frequency domain,
LTE	–	linear tensor encoding,
MD	–	Mean Diffusivity,
MddMRI	–	Multidimensional dMRI,
MK	–	Mean Kurtosis,
MK_a	–	anisotropic Mean Kurtosis,
MK_i	–	isotropic Mean Kurtosis,
mpMRI	–	multi-parametric Magnetic Resonance Imaging,
MRI	–	Magnetic Resonance Imaging,
NIST	–	National Institute of Standards and Technology,

NMR – Nuclear Magnetic Resonance,
PCa – prostate cancer,
PDF – Probability Density Function,
PGSE – Pulsed Gradient Spin-Echo,
PI-RADS – Prostate Imaging Reporting and Data System,
PI-QUAL – Prostate Imaging Quality,
PNS – Peripheral Nerve Stimulation,
PSA – Prostate Specific Antigen,
PVE – Partial Volume Effect,
PVP – polyvinylpyrrolidone,
PZ – peripheral zone of the prostate,
RF – Radiofrequency (pulse),
ROI – Region Of Interest,
SAR – Specific Absorption Ratio,
SAFE – Stimulation Approximation by Filtering and Evaluation,
SE – spin echo,
SENSE – SENSitivity Encoding ,
SNR – Signal-to-Noise Ratio,
SSIM – Structural Similarity Index Measure,
STE – spherical tensor encoding,
T_1 – longitudinal relaxation time,
T_2 – transverse relaxation time,
T_2^* – 'effective' transverse relaxation time,
TE – echo time,
TR – repetition time,
TRUS – Transrectal Ultrasound,
TSE – Turbo Spin Echo,
TZ – transitional zone of the prostate,
VERDICT – Vascular, Extracellular and Restricted Diffusion for Cytometry in Tumours,
μFA – microscopic Fractional Anisotropy.

Notation

δ – diffusion gradient pulse width,
Δ – diffusion gradient pulse separation,
τ – diffusion time,
ϕ – spin's phase,
b – b-value/strength of the diffusion encoding,
b_Δ – normalised b-tensor anisotropy,
B_0 – static magnetic field,
$\mathbf{B}_1$ – radiofrequency field,
$\mathbf{D}$ – diffusion tensor,
$\overline{\mathbf{D}}$ – apparent diffusion tensor,
D – diffusion coefficient,
G – gradient amplitude,
$\mathbf{G}(t)$ – linear gradient,
G_x – frequency-encoding gradient,
G_y – phase-encoding gradient,
G_z – slice selection gradient,
$\mathbf{q}$ – q-space vector,
$\mathbf{M}$ – macroscopic net magnetisation vector,
$\mathbf{n}$ – orientation of the diffusion gradient,
$P(\phi)$ – distribution of accrued phase by spins,
$P(\mathbf{D})$ – distribution of diffusion tensors,
$\mathbf{q}(t)$ – spin-dephasing vector,
$\mathbf{r}$ – n-dimensional displacement vector,
$\mathbf{r}(t)$ – spin displacement trajectory/vector,
r_{RMS} – root-mean-squared displacement,
$S(\mathbf{G})$ – diffusion-weighted signal,
$S(0)$ – non diffusion-weighted signal,

$\mathbf{v}(t)$ – spin velocity vector,
ω_0 – Larmor frequency,
$\mathbf{W}$ – apparent kurtosis tensor,
$\mathbf{u}$ – unitary vector.

List of Tables

List of Figures

Part I

Introduction and Background

Chapter 1

Thesis Overview

Contents

1.1 Motivation

The advent of magnetic resonance imaging (MRI) in the 1970s has significantly contributed to non-invasive characterisation of tissues. With clever manipulation of the magnetic field gradients and radiofrequency pulses, MRI allows for visualisation of living tissue and provides new markers of structure at macroscopic scales. Diffusion MRI (dMRI) signals carry information about the motion of water molecules which is modulated by the microstructure of the tissue. It is therefore feasible to infer information about different microscopic compartments, e.g., different cell types, including their size, shape and orientation, which helps us to understand ongoing processes in healthy and diseased tissues. However, the amount, accuracy and discriminative power of the information attainable relies additionally on the MR hardware used.

Recent years of MR hardware development have lead to the design of novel MR systems with ultra-strong gradients (e.g, [Kimmlingen, 2017]), enabling the exploration of microstructure in greater detail. However, despite their whole-body imaging capability, these systems have so far only been used in studies exploring brain tissue. In this work, the first results beyond imaging of the head are presented, and the feasibility of ultra-strong gradient diffusion imaging of the prostate is assessed. The motivation for pushing imaging-based diagnosis of prostate cancer is the significant disease burden. Prostate cancer is among the most common forms of cancer in men, with 1.4 million new cases diagnosed globally in 2020 and 375 304 related deaths reported it the same year [Wang et al., 2022].

Multiparametric MRI (mpMRI), is currently a standard clinical practice prior to prostate biopsy. In contrast to biopsy, however, mpMRI has unique potential to evaluate the prostate as a whole, non-invasively, thus providing clinicians with a vital diagnostic stepping-stone between non-specific blood-based markers and invasive biopsy. Synergistically with prostate specific antigen level monitoring, it composes an effective tool for detection of clinically significant prostate cancer (csPCa). Most importantly, dMRI has a role in mpMRI as one of two key contrasts for lesions depiction. A clinical dMRI protocol typically includes acquisition at low-to-moderate diffusion weightings with low signal-to-noise ratio and at low spatial resolution. Recent more advanced diffusion techniques hold great promise in biopsy reduction [Singh et al., 2022], but their acquisition on low-end clinical systems is hampered by the gradient hardware and imaging strategy. As a result, it is not possible to fully explore the frameworks of the latest research advances in everyday practice. Improving data quality as well as the sensitivity and specificity of dMRI signals to microstructural changes in prostate cancer is essential for improved screening in early detection of the disease and reducing unnecessary biopsies. Improving clinical prostate MRI is vital, as many of the cancerous lesions are not visible in standard MRI scans [van Houdt et al., 2020], especially low grade changes where early detection is important for the patient's chances of survival.

The work within this thesis tackles some of the challenges of prostate dMRI in clinical practice. By drawing inspiration from research studies advancing dMRI for imaging brain, we devise advanced, and most importantly safe, experimental strategies and present the first pilot scans of patients with prostate cancer from an Active Surveillance clinical group. By employing novel MRI strategies, we

boost the image quality and hence the reliability of quantitative measures in healthy and cancerous tissue. The methodology described in this work is a first step towards comprehensive characterisation of the prostate gland using the latest MR hardware and software.

1.2 Highlights of the work

The key highlights of this thesis are as follows:

- **Firstly**, the whole-body MR systems equipped with strong gradients capability, so far only used for investigating brain structure, can be safely used in imaging landmarks below the neck.
- **Secondly**, leveraging the capability of ultra strong gradients, i.e., exceeding clinically available 40-80 mT/m gradients, unlocks the acquisition of new diffusion contrasts at shorter diffusion times and echo times. Moreover, the achieved higher b-values can more effectively suppress signals from healthy tissue, enhancing tumour-to-normal tissue contrast and lead to hyperintense signals in the tumour. Such enhanced contrast can considerably improve the conspicuity of small lesions.
- **Thirdly**, deployment of non-Cartesian image readouts, including at high in-plane resolution, with image reconstruction expanded to include monitored MR field perturbations, provides diffusion weighted images of the prostate of excellent quality and higher signal-to-noise ratios compared to conventional readout. This, in turn, improves the data fidelity in comparison to structural images, and aids with the depiction of lesion edges.

The ultimate goal of this work was to achieve increased sensitivity to microstructural changes in the disease and enhanced cancerous lesion discernibility with improved spatial location. This has the potential to yield novel insights into the pathology, and therefore can form a solid basis for more advanced dMRI experiments beyond those explored and reported in the core part of this thesis (**Chapter 8** *Outlook*). Ultimately, based on this work, new imaging biomarkers can be developed, hopefully addressing the limitations of current mpMRI scans, advancing future clinical prostate MRI.

1.3 Thesis outline

Chapter 2 introduces the concept of relaxation and diffusion processes and reviews MR contrast creation and its encoding, and subsequent image reconstruction. Gradients for encoding diffusion weighted signals as well as spatial localisation of the signal are covered. Furthermore, a brief overview of MR hardware advancements is given, alongside a more detailed description of magnetic field perturbations, MR safety and sequence design considerations. The use of equations and technical language is kept to a minimum to make this overview more approachable.

The healthy and cancerous prostate tissue structure and composition is the scope of **Chapter 3**. Importantly, the diagnostic pathway of prostate cancer and relevant research studies advancing its microstructral characterisation are also summarised.

Patient safety during the scan with use of an MR machine is a topic of ongoing discussion in the MR society. Therefore, prior to any imaging below the neck being performed on the ultra-strong gradient MR system, the concerns about patients safety needed to be assessed. In **Chapter 4**, a report of the physiological effects of human body imaging with 300 mT/m gradients is given. The reported results on the likelihood of elicitation of magnetophosphenes provide new insights into the complex interaction of time varying magnetic fields and the human body.

The MR systems equipped with strong gradients, e.g., 300 mT/m, enable stronger diffusion weightings per unit time compared to conventional gradient designs. Consequently, the time needed for diffusion encoding gradients and thus the echo time, can be drastically shortened. This, in turn, brings the benefit of increased signal-to-noise ratio, and facilitates acquisitions of contrasts in the MR measurement space not accessible for exploration on systems with low gradient amplitude. Those can be leveraged in multi-contrast experiments, e.g., diffusion-relaxometry, for tumour characterisation. **Chapter 5** presents the feasibility of strong gradients applied in imaging the prostate. The signal-to-noise ratio gains and higher b-value achieved with shorter encoding time enabled improved tumour-to-lesion contrast with increased restricted diffusion signal present at shorter echo times. The achieved gains could benefit microstructural parameter estimation of low-grade lesions.

Despite the clear gains of strong diffusion gradients, their deployment in combination with the standard single shot echo planar imaging (EPI) readout leads to unnecessarily long echo times, especially at higher in-plane resolutions. As a result, a drop of signal-to-noise ratio and loss of sensitivity to shorter T_2 compartments is inevitable. Alternative encodings, such as spiral readout, can ameliorate these effects at the cost of a more complicated image reconstruction process. **Chapter 6** focuses on the feasibility of expanded encoding model reconstruction with MR field monitoring in imaging the prostate. With the flexibility and time efficiency of spiral readouts, further signal-to-noise ratio gains and finer spatial resolutions can be obtained. Besides those advantages, accounting for field perturbations at the reconstruction stage addresses the inherent problems of adverse artefacts in dMRI data, and thus enhances its quality, simplifying data post-processing pipelines.

Chapter 7 concludes the findings in this thesis and places them in the scope of potential translation to new advanced MR system being released worldwide.

Ultimately, potential future avenues that can be pursued in prostate cancer imaging, gratefully inspired by many discussions with scientists from the field, are formulated in **Chapter 8**. A proof of concept in vivo experiment with arbitrary diffusion encoding and spiral readout is reported. This exploratory experiment is a step towards mapping micro- and macroscopic features of the tissue with gradient waveforms beyond a single pair of pulsed-gradients using a strong gradient system and non-Cartesian readouts.

Chapter 2

Technical background: NMR Physics, MR Hardware and Software

Contents

2.1 Spin physics, bulk magnetisation and RF excitation

Atomic nuclei consisting of an odd number of protons or neutrons possess a spin angular momentum, J, often called *nuclear spin*, from which originates a *magnetic dipole moment*, μ. A nucleus-dependent constant called *gyromagnetic ratio*, γ, links those two properties as

$$\mu = \gamma J \,. \tag{2.1}$$

The magnitude of the magnetic dipole moment depends on the spin quantum number I, which is another intrinsic property of the nucleus. In MR research, the most common nucleus to study is that of the hydrogen atom (^{1}H, as it comprises a single proton) because of its high natural abundance in biological tissues. The gyromagnetic ratio of ^{1}H is 2.675 $\times$ 10^8 rad/s/T and its half-integer spin is $I = 1/2$.

The ensemble of protons present in a given tissue form a spin system. As thermal energy typically dominates over inter-spin interactions at body temperature, spins tend to be randomly oriented, leading to a zero net magnetisation. Under the influence of an external static magnetic field $\mathbf{B}_0$ pointing along the z-axis, spins tend to precess around $\mathbf{B}_0$ at an angular frequency commonly called the *Larmor frequency*, given by

$$\omega_0 = \gamma B_0 \,, \tag{2.2}$$

where $B_0 = \|\mathbf{B}_0\|$. While this precession can occur with a z component either parallel or anti-parallel to $\mathbf{B}_0$, the parallel configuration has slightly lower energy than the anti-parallel one. This implies that the spin system now presents a non-zero macroscopic net magnetisation vector $\mathbf{M}$ pointing along the $\mathbf{B}_0$ field. Being able to treat the behaviour of spins in terms of a net magnetisation allows for a classical description of NMR.

Once the magnetisation $\mathbf{M}$ is generated via the $\mathbf{B}_0$ field, an additional circularly oscillating external pulse at the resonance frequency ω_0 can be applied to evoke a rotating magnetic field $\mathbf{B}_1$ in the plane perpendicular to $\mathbf{B}_0$, i.e., the transverse plane. This process is called radiofrequency (RF) excitation and results in tipping the initial magnetisation $\mathbf{M}$ with respect to the z-axis by a prescribed angle that depends on the amplitude and duration of $\mathbf{B}_1$.

2.2 Relaxation

Application of an RF pulse disturbs or flips the magnetisation vector $\mathbf{M}$ out of alignment from the main magnetic field (i.e., out of the alignment with the z-axis). The amount of this rotation or flip depends on the strength and duration of the RF pulse. The magnetised spin system gradually returns to its equilibrium state. This phenomenon is called relaxation and can be decomposed into two processes:

- *Spin-lattice relaxation:* An energy exchange between the spins and their surrounding environment by heat transfer. In other words, the spins give the energy obtained from the RF pulse back to the surrounding lattice.

- *Spin-spin relaxation:* Loss of phase coherence of the magnetised spin system due to local field inhomogeneities, e.g., local fluctuations of the magnetic field induced by surrounding spins, which are superimposed to the main magnetic field.

On the one hand, spin-lattice relaxation leads to the gradual growth of the longitudinal component M_z of the magnetisation vector, characterised by the longitudinal relaxation time T_1. After application of an RF pulse, the longitudinal component of the magnetisation vector evolves in function of the time t as

$$M_z(t) = M_z(0^-)\left[1 - \exp\left(-\frac{t}{T_1}\right)\right], \tag{2.3}$$

with $M_z(0^-)$ the longitudinal magnetisation at equilibrium.

On the other hand, spin-spin relaxation translates as spatially varying precession frequencies, leading to spin dephasing. This is reflected in the MR signal as an exponential decay of the transverse components M_x and M_y of the magnetisation vector with a time constant T_2:

$$M_x(t) = M_x(0^+)\cos(\omega_0 t)\exp\left(-\frac{t}{T_2}\right), \tag{2.4}$$

$$M_y(t) = M_y(0^+)\sin(\omega_0 t)\exp\left(-\frac{t}{T_2}\right), \tag{2.5}$$

with $M_x(0^+)$ and $M_y(0^+)$ the x- and y-components of the magnetisation vector immediately after turning off the RF pulse [Bloch, 1946]. However, in any NMR experiment, the transverse magnetisation decays much faster than would be predicted by natural mechanisms and this rate is denoted by T_2^*. T_2^* is usually called 'observed' or 'effective' T_2 and is always less than or equal to T_2.

For example, the magnitude of the initial total transverse component $M_{xy}(0^+) = M_x(0^+) + iM_y(0^+)$ equals $M_z(0^-)$ if the applied RF pulse is 90°. Once rotated in the transverse plane, that magnetisation vector precesses around the z-axis with a constant angular frequency ω_0, while its magnitude decreases exponentially according to

$$M_{xy}(t) = M_{xy}(0^+)\exp\left(-\frac{t}{T_2}\right)\exp(i\omega_0 t)\,. \tag{2.6}$$

Positioning an electrically conducting coil in the transverse plane enables the measurement of a voltage (signal) created through induction by the time-varying transverse magnetisation. This oscillating signal of exponentially decaying magnitude is called free induction decay (FID).

2.3 Diffusion

Due to thermal energy, molecules in a fluid adopt a random translational motion called diffusion. The trajectory of diffusing molecules is typically depicted as a random walk where particles can suddenly change direction because of collisions with other particles in the medium (Figure 2.1). The described phenomenon is named Brownian motion as it was firstly discovered by Robert Brown [Brown, 1828] who observed the everlasting jittery motion of grains of pollen suspended in water

under a microscope. A theoretical framework was given by Albert Einstein [Einstein, 1905] in the case of an *isotropic* (i.e., direction-independent) diffusion medium wherein molecular motion can be statistically described with the following Gaussian Probability Distribution Function (PDF):

$$P(\mathbf{r}) = \frac{1}{\sqrt{(4\pi D\tau)^n}} \exp\left(-\frac{||\mathbf{r}||^2}{4D\tau}\right), \tag{2.7}$$

where $\mathbf{r}$ is the n-dimensional displacement vector, τ is the diffusion time and D is the diffusion coefficient, which quantifies the average capacity of molecules to diffuse. The root-mean-squared displacement, r_{RMS}, was also proposed by Einstein as a descriptor of the diffusion process:

$$r_{\mathrm{RMS}} = \sqrt{\langle||\mathbf{r}||^2\rangle} = \sqrt{2nD\tau}\,, \tag{2.8}$$

with the angled brackets denoting the statistical average over particle trajectories. The r_{RMS} is often called the characteristic diffusion length or Einstein length.

Einstein's formalism only applies in the case of a single isotropic medium wherein diffusion is unimpeded by physical barriers. This type of diffusion is referred to as *free diffusion*. When diffusing particles encounter obstacles, their motion can be either *restricted* if they are bound within a given structure or *hindered* if these obstacles can be circumvented upon changing direction. Given typical diffusion times in abdominal dMRI, free diffusion can only be expected in the bladder. However, complex biological tissues such as the prostate are highly heterogeneous, consisting of multiple types of cellular compartments (e.g., stroma, lumen, and epithelium), and therefore diffusion cannot be considered free. Typically, the diffusion of water molecules confined within the intra-cellular spaces, e.g., epithelial cells, is restricted (an example in Figure 2.1). Indeed, given a diffusion time of 50 ms, a freely diffusing water molecule would travel an average distance of 25 µm whereas the diameter of healthy epithelial cells is less than 20 µm. As a consequence of restriction/hindrance or the presence of multiple diffusion compartments, the measured signal deviates from free diffusion and may disclose tissue *anisotropy* [Cleveland et al., 1976, Tanner, 1979] (i.e., direction-dependence) or exhibit time-dependence [Latour et al., 1994, Mitra et al., 1992, Sen, 2004], among others.

For measurable diffusion times, the r_{RMS} and D strongly depend on the local cellular geometry. Nonetheless, the description of this problem can remain similar to that of the previous free diffusion, by substituting the intrinsic diffusivity, i.e., D, in Equations 2.7 and 2.8 by an apparent diffusion coefficient, D_{app} [Le Bihan et al., 1986], which may be direction-dependent. A more general PDF is needed to characterise this diffusion anisotropy

$$P(\mathbf{r}) = \frac{1}{\sqrt{(4\pi\tau)^3|\mathbf{D}|}} \exp\left(-\frac{\mathbf{r}^{-T}\cdot\mathbf{D}^{-1}\cdot\mathbf{r}}{4\tau}\right) \tag{2.9}$$

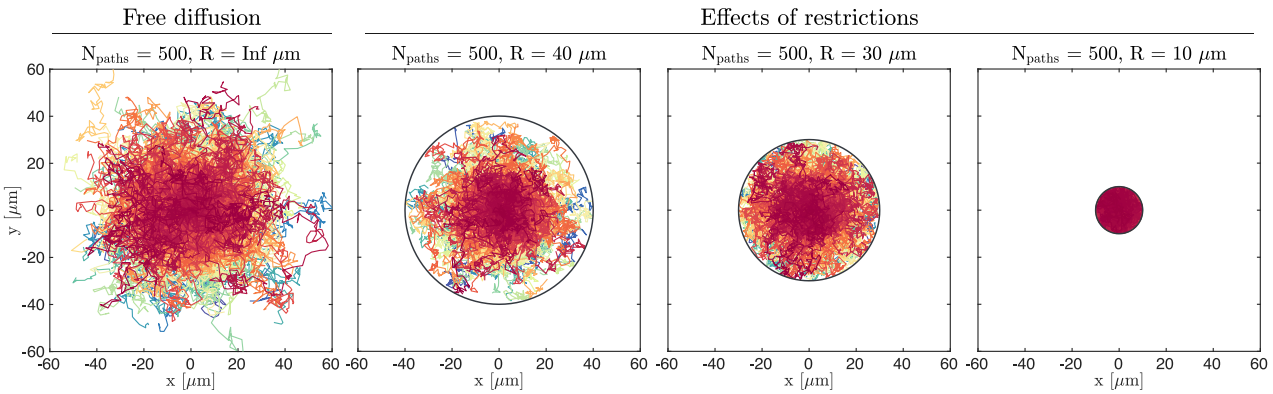

Figure 2.1: Different sets of N_{paths} two-dimensional random walks (1000 time steps for each random walk, driven by the intrinsic diffusivity $D = 1$ µm^2/ms) with different restriction radii R. Restriction increases with decreasing radius. Each coloured path corresponds to a distinct path starting from the central point, i.e., $(x, y) = (0, 0)$.

with the (apparent) diffusion tensor

$$\mathbf{D} = \begin{pmatrix} D_{xx} & D_{xy} & D_{xz} \\ D_{xy} & D_{yy} & D_{yz} \\ D_{xz} & D_{yz} & D_{zz} \end{pmatrix}, \tag{2.10}$$

which is a symmetric positive (semi)definite tensor with up to six independent tensor elements [Basser et al., 1994]. Note that the above apparent diffusion tensor does not explicitly depend on time, but is rather implicitly associated to a certain observational timescale.

Ultimately, accounting for anisotropy with a diffusion tensor (Equation 2.9 and 2.10) may not suffice to accurately describe non-Gaussian diffusion processes [Assaf and Cohen, 1998, Beaulieu and Allen, 1994, Stanisz et al., 1997] and more complex formulations have to be considered (Section 2.6).

2.4 Spatial localisation of the MR signal and spin-echo experiment

In order to spatially resolve the imaging volume of interest additional RF pulses and time-varying linear magnetic gradient fields are superimposed onto the main static uniform magnetic field $\mathbf{B}_0$ [Brown et al., 1982, Likes, 1981, Ljunggren, 1983].

2.4.1 Radiofrequency pulses and spin-echo experiment

Conventionally, the coordinate axes of the scanner for imaging in transverse plane are defined as: phase encoding - y-axis, readout - x-axis, and slice direction - z-axis. All the planes are interchangeable, however, for the remaining of the discourse aforementioned definition is used.

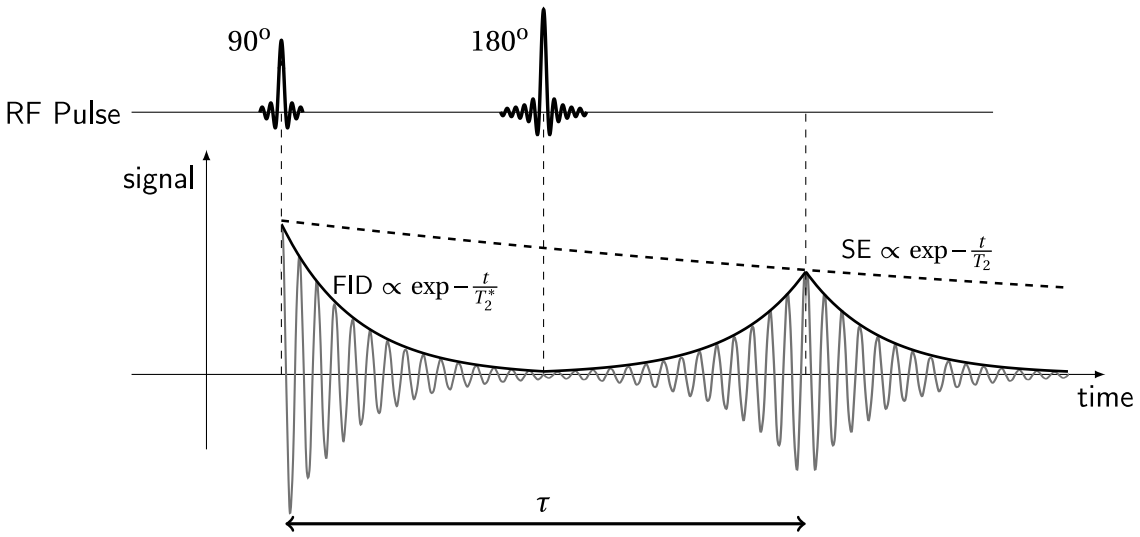

Figure 2.2: RF pulse effects on the signal formation. The spins rephase after application of an RF pulse, later forming a SE signal at the echo time TE = τ (here τ denotes time for SE, not diffusion time), as measured from the centre of the symmetric excitation pulse.

The slice selection gradient G_z makes the z-component of $\mathbf{B}_0$, $B_{0,z}$, vary linearly along the z-axis as

$$B_{0,z} = B_0 + G_z z \,. \tag{2.11}$$

As the magnetic field perceived by spins now varies along the z-axis, so do their resonance frequencies along this axis (initially all equal to ω_0 ignoring relaxation effects). Once the excitation RF pulse is applied at the mean frequency ω_0 with a specific bandwidth (BW), only the nuclei precessing over the range of frequencies associated with a specific slice thickness will be excited. This forms the principle of selectively exciting a slice, i.e., encoding the signal in the slice dimension. From this point, the transverse magnetisation precesses around the z-axis with the Larmor frequency, with the x- and y- time-dependent components being the real and imaginary parts of a complex number. In reality, due to the interactions of spins with surrounding spins (related to T_2) and microscopic field inhomogeneities (related to T_2^*), each individual spin precesses with a slightly different frequency (dephasing), causing magnitude of the transverse magnetisation to decay exponentially according to the T_2^* relaxation time (Figure 2.2).

To compensate for dephasing due to local field inhomogeneities, it is necessary to reverse the dephasing of the nuclear spins during their T_2^* relaxation. This can be done by applying an extra RF pulse [Hahn, 1950] called a 'refocusing' RF pulse after the excitation RF pulse. This reversal effectively rephases the spins again, generating a new MR signal called 'spin echo' (SE) (Figure 2.2, with typical 90° RF pulse for excitation and 180° RF for refocusing). The formation of the SE signal occurs at a time called 'echo time' (TE), which is equal to twice the time between the excitation and refocusing RF pulses. The resulting T_2-weighted signal can be described as

$$S = S_0 \exp\left(-\frac{\mathrm{TE}}{T_2}\right) , \tag{2.12}$$

where S_0 is the measured signal at TE = 0 ms.

2.4.2 K-space encoding

Additional gradients are also applied in the two other orthogonal spatial dimensions (the x- and y-axes), called the frequency- (G_x) and phase-encoding (G_y) gradients in 2D imaging. These gradients perturb the frequency and the phase of nuclear spins and therefore result in a spatially-frequency-encoded signal filling the volume in the spatial-frequency domain (k-space).

Specifically, k-space represents the spatial frequency information in two or three dimensions of an object. The data acquisition vector contains the sampled raw data, which, e.g., for the case of 2D imaging would stem from a single slice. The k-axes (k_x, k_y) represent spatial frequencies in the x- and y-directions, not to be confused with positions of the individual pixels (x, y) in the image. Each k-space point contains spatial frequency and phase information about the entire set of pixels in the final image. Conversely, each pixel in the image maps to every point in k-space. Image data and k-space data are mathematically related via the Fourier transformation.

The position in k-space is directly related to the time-varying gradient across the object being imaged as

$$\mathbf{k}(t) = \frac{\gamma}{2\pi} \int_0^t \mathbf{G}(t')\,\mathrm{d}t' \,. \tag{2.13}$$

K-space is populated with signal samples collected with time-varying gradients realising certain trajectories in k-space. These gradients are designed such that the k-space centre is reached at the point of complete refocusing of the signal, i.e., at TE (Section 2.4). The extent of this trajectory defines the required image resolution, whereas the field of view (FOV) determines the necessary filling density. In 2D encoding, the classical single-shot Cartesian sampling in which multiple lines are acquired bidirectionally after each RF excitation is called EPI [Stehling et al., 1991] (Figure 2.3, *left column*). Despite its widespread adaptation owing to ease of the calibration resulting from the repetitiveness of the gradient shapes within the readout, as well as computational efficiency through direct application of Fast Fourier Transform (FFT) without any regridding, the EPI readout is not the best use of the gradient system capabilities for the purpose of maximising the speed. Here, k-space speed is defined as k-space volume covered per unit of time, where a certain point in k-space would be 'covered' when it lies within a sphere of radius 1/FOV around a given sampled k-space point. In EPI, the transition from one line to another, i.e., a sharp turn, requires considerable deceleration. This limitation can be addressed by the employment of trajectories that require fewer of such sharp turns such as spiral sampling [Ahn et al., 1986, Zahneisen et al., 2012] (Figure 2.3, *right column*).

2.4.2.1 Spiral readout

In spiral readout, the independent phase- and frequency-encoding functions used in, e.g., Cartesian EPI, are replaced with 2D readout functions defined in the polar coordinates (r, θ), which relate to

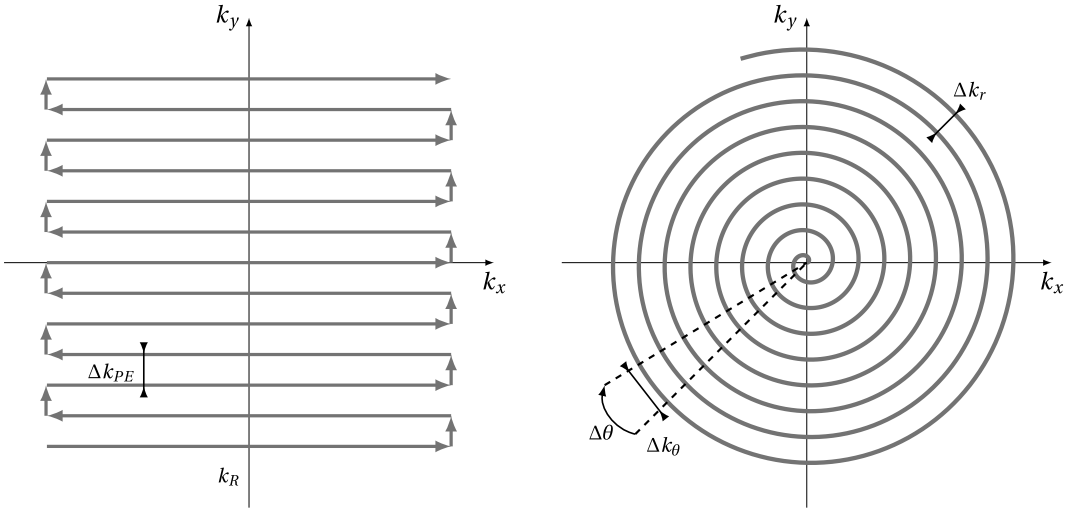

Figure 2.3: EPI and spiral readouts with parametrisation. For EPI: Δk_{PE} - encoding step in phase direction, k_R - frequency (read) direction; for spiral: Δk_r - radial sampling interval, Δk_θ - azimuthal sampling interval, $\Delta\theta$ - encoding step in azimuthal coordinate.

Cartesian coordinates (k_x, k_y) through

$$k_x = r\cos\theta\,, \tag{2.14}$$

$$k_y = r\sin\theta\,, \tag{2.15}$$

where r is the radius defined from the the centre of the k-space, and θ is the azimuthal angle.

Usually, Archimedean spirals are used, which describe the azimuthal trajectory sweep as a function of time t as follows

$$k(t) = \lambda\theta(t). \tag{2.16}$$

Here, λ is a constant determined by the Nyquist sampling requirement. For alias-free sampling that satisfies the Nyquist criterion, $\Delta k = 1/L$, where $L = L_x = L_y$ is the FOV and Δk is the spacing between k-space samples. For a single shot spiral this condition requires that

$$\lambda = \frac{N_{\text{shot}}}{2\pi L} = \frac{1}{2\pi L} \tag{2.17}$$

and is a result of *radial* Nyquist (k_r) sampling theorem.

The gradient waveforms to produce the coverage of k-space are calculated by differentiation of the k-space trajectory:

$$G_x = \frac{2\pi}{\gamma}\frac{\mathrm{d}k_x}{\mathrm{d}t} = \frac{2\pi\lambda}{\gamma}\frac{\mathrm{d}\theta}{\mathrm{d}t}\left(\cos\theta - \theta\sin\theta\right), \tag{2.18}$$

$$G_y = \frac{2\pi}{\gamma}\frac{\mathrm{d}k_y}{\mathrm{d}t} = \frac{2\pi\lambda}{\gamma}\frac{\mathrm{d}\theta}{\mathrm{d}t}\left(\sin\theta + \theta\cos\theta\right). \tag{2.19}$$

The velocity of k-space transversal in any given direction is proportional to the gradient amplitude

in that direction. The maximum gradient strength together with receiver bandwidth defines the *azimuthal* Nyquist (k_θ) sampling requirement. This requirement prevents aliasing from azimuthal undersampling (i.e., along a spiral interleaf). In practice, this requirement is always met as sampling density along the frequency encoding direction is virtually at no cost. In practice, the limitation comes from the receiver bandwidth of the scanner and for commonly used FOV and gradient amplitudes, there is no risk of data undersampling in frequency encoding direction. Importantly, aliasing due to radial and azimuthal undersampling are independent and can be separately controlled.

Lastly, the maximum k-space radius reached, $k_{\max}$, is defined by

$$k_{\max} = \frac{N}{2L} \tag{2.20}$$

where N is the effective matrix size. The final azimuthal angle of k-space trajectory for a single shot spiral is given by:

$$\theta_{\max} = \frac{k_{\max}}{\lambda} = \frac{\pi N}{N_{\text{shot}}} = \pi N. \tag{2.21}$$

The presented theorem for sampling was replaced with constant time sampling, which is employed in this work, and which means that the angular velocity is not constant. Here, the choice of the sampling time is such that Nyquist requirement is fulfilled in the periphery of k-space and the gradients operated at the maximum speed.

Spirals are always restricted in terms of their speed which is defined by $G_{\max}$. However, due to hardware slew rate limitation for the innermost revolutions on the trajectory, their speed is lower than maximal reachable. Therefore, the points around the k-space centre are sampled on a higher rate than required by the Nyquist theorem. Nevertheless, spirals make better use of both gradient axes than EPI [Glover, 2012]. Moreover, spiral(-out) sensitivity to motion is reduced as the k-space centre is acquired in the beginning of the readout and those data points are gradient moment-nulled along both axes owing to the gradient moments periodic oscillations around zero. Besides, spirals allow for achieving shorter TEs, leading to an effective SNR gain. The pitfall, in turn, is that spirals are more sensitive to spatial depending image blurring as the phase encoding direction changes with each point on the trajectory which interacts with, e.g., off-resonance effects. The blurring is observed in all directions with its total amount depending on the accumulated off-resonant phase at the end of the readout, and thus, can be very perceptually disturbing. Similarly to acquisitions with other readout, if the FOV of spiral is not chosen adequately, aliasing artefacts could be introduced to images and would be observed as streaks and swirls.

2.5 Gradient encoding for diffusion contrast

Magnetic field gradients can be used to sensitise the measured signal to spin diffusion. For a brief description of the physics of diffusion, please refer to Section 2.3.

Let us consider an ensemble of spins subject to an applied linear gradient $\mathbf{G}(t)$. A given spin following the trajectory $\mathbf{r}(t)$ between times $t = 0$ and $t = \tau$ (at which the diffusion signal is

measured) will accrue the phase

$$\phi(\tau) = \gamma \int_0^\tau \mathbf{G}(t) \cdot \mathbf{r}(t)\, \mathrm{d}t\,. \tag{2.22}$$

Introducing the spin-dephasing vector,

$$\mathbf{q}(t) = \gamma \int_0^t \mathbf{G}(t')\, \mathrm{d}t'\,, \tag{2.23}$$

and with the knowledge that diffusion gradients satisfy the echo condition ($\mathbf{q}(\tau) = \mathbf{0}$, see Equation 2.30) the above accrued phase can also be rewritten as

$$\phi(\tau) = -\int_0^\tau \mathbf{q}(t) \cdot \mathbf{v}(t)\, \mathrm{d}t\,, \tag{2.24}$$

where the velocity $\mathbf{v}(t)$ is the time-derivative of the particle's displacement $\mathbf{r}(t)$. The signal arising from the entire spin ensemble writes as

$$S = S_0 \int P(\phi) \exp(i\phi)\, \mathrm{d}\phi\,, \tag{2.25}$$

where $P(\phi)$ is the distribution of accrued phases in the spin system.

If one were to discretise Equation 2.22 in time, the accrued phase would appear as a large sum of random terms all drawn from the same probability distribution function, i.e., that describing the diffusion process. Consequently, the central limit theorem ensures that this phase is Gaussian distributed. In the absence of coherent spin flow, spins are as likely to diffuse in a given direction as to diffuse in the opposite direction, which implies that the average accrued phase $\langle\phi\rangle$ must be zero according to Equation 2.22. Using the fact that $P(\phi)$ is a Gaussian distribution with zero mean, Equation 2.25 can be rewritten as

$$S = S_0 \exp\left(-\frac{\langle\phi^2\rangle}{2}\right). \tag{2.26}$$

Assuming that the gradient orientation (and therefore that of the spin-dephasing vector) remains constant through time, $\langle\phi^2\rangle$ can be expressed more explicitly using Equation 2.24 and the fact that the diffusion coefficient D of the medium is straightforwardly related to the velocity auto-correlation function $\langle v(t)v(0)\rangle$ along the diffusion direction in the case of Gaussian diffusion ($\langle v(t)v(0)\rangle = 2D\,\delta(t)$, with the Dirac distribution $\delta(t)$) [Lundell and Lasič, 2020]. One obtains

$$\langle\phi^2\rangle = 2D \int_0^\tau q^2(t)\, \mathrm{d}t\,. \tag{2.27}$$

The definition of b-value, which summarises the overall strength of the diffusion weighting applied to the signal, is

$$b = \int_0^\tau q^2(t)\, \mathrm{d}t. \tag{2.28}$$

The b-value is expressed in units of (time)/(length)^2. Finally, one retrieves the well-known dMRI signal attenuation:

$$S = S_0 \exp(-bD)\,. \tag{2.29}$$

2.5.1 Stejskal-Tanner encoding

The most commonly used dMRI sequence is the pulsed-gradient spin-echo (PGSE), based on the SE sequence [Hahn, 1950] with additional diffusion encoding gradients [Stejskal and Tanner, 1965]. In the most basic form of this sequence, a couple of identical gradients of amplitude G and duration δ, are introduced and placed before and after the 180° refocusing RF pulse. As effect of the refocusing, the second diffusion gradient - separated by the time Δ from the onset of the first gradients - induces opposite dephasing, giving the spin echo condition

$$\mathbf{q}(\tau = \mathrm{TE}) = \gamma \int_0^{\mathrm{TE}} \mathbf{G}(t)\,\mathrm{d}t = \mathbf{0}. \tag{2.30}$$

For the spin dephasing vector of the Stejskal-Tanner sequence, i.e., the case of the trapezoidal gradients, one can define a b-value associated with the sequence as

$$b = \gamma^2 G^2 \delta^2 \left[\Delta - \frac{\delta}{3}\right], \tag{2.31}$$

with the term between squared brackets called the 'effective diffusion time'.

Denoting by $\mathbf{n}$ the constant orientation of the diffusion gradients, the diffusion signal can be expressed similarly to Equation 2.25:

$$S = S_0 \int P(\mathbf{D}) \exp(-b\,\mathbf{n}^{\mathrm{T}} \cdot \mathbf{D} \cdot \mathbf{n})\,\mathrm{d}\mathbf{D}\,, \tag{2.32}$$

where $P(\mathbf{D})$ is the distribution of diffusion tensors characterising the diffusion medium and the integral spans the space of symmetric positive-(semi)definite tensors. Although simplistic in terms of implementation and experiment design, the conventional Stejskal–Tanner diffusion encoding does not enable the disentanglement of certain microstructural features within a voxel. Therefore, sampling schemes beyond trapezoidal gradients have been proposed [Eriksson et al., 2013, Lasič et al., 2014, Topgaard, 2017].

2.5.2 B-tensor encoding

Whereas a conventional Stejskal–Tanner sequence probes diffusion through the b-value, b, and constant orientation, $\mathbf{n}$, b-tensor encoding (or tensor-valued diffusion encoding) introduces more general gradient waveforms wherein the gradient orientation typically varies in time. This implies that the orientation of the spin-dephasing vector $\mathbf{q}(t)$ defined in Equation 2.23 also varies in time. In this

context, Equation 2.32 rewrites as

$$S = S_0 \int P(\mathbf{D}) \exp\left(- \int_0^\tau \mathbf{q}^{\mathrm{T}}(t) \cdot \mathbf{D} \cdot \mathbf{q}(t) \, \mathrm{d}t \right) \mathrm{d}\mathbf{D} \, . \tag{2.33}$$

Introducing the diffusion-encoding tensor (or b-tensor),

$$\mathbf{b} = \int_0^\tau \mathbf{q}(t) \cdot \mathbf{q}^{\mathrm{T}}(t) \, \mathrm{d}t \, , \tag{2.34}$$

Equation 2.33 reduces to

$$S = S_0 \int P(\mathbf{D}) \exp(-\mathbf{b} : \mathbf{D}) \, \mathrm{d}\mathbf{D} \, , \tag{2.35}$$

with the Frobenius inner product ":". Note that the trace of the b-tensor corresponds to the aforementioned b-value.

While the diffusion tensor is only probed along one spatial direction during a Stejskal-Tanner sequence (as shown in Equation 2.32), a tensor-valued diffusion-encoded sequence can probe the diffusion tensor along multiple directions during a single acquisition (as shown in Equation 2.33). The novelty of this new encoding scheme is contained in the shape, i.e., anisotropy, of the b-tensor, which can be tuned when designing a diffusion gradient waveform. For instance, any sequence designed to yield a linear (stick-like) b-tensor generates the same diffusion encoding as that of a PGSE sequence. Alternatively, a sequence associated with a spherical (isotropic) b-tensor only encodes for the isotropic diffusivities of the underlying microscopic diffusion tensors.

In other words, these specifically designed gradient waveforms allow for the signal acquisition in a multidimensional space of b-tensors with arbitrary shapes which, in turn, allow for isolation or removal of specific descriptors of the underlying tissue properties. In particular, if the imaged object contains microscopic compartments that vary in more than one attribute (e.g., diffusivity, anisotropy, orientation), b-tensor encoding allows for the disentanglement of intricate microstructural features such as the variance of isotropic diffusivities or microscopic anisotropy [Szczepankiewicz et al., 2016].

2.6 Examples of the mathematical descriptions of diffusion-weighted signal

2.6.1 Diffusion Tensor Imaging and Diffusion Kurtosis Imaging

Diffusion Tensor Imaging (DTI) and Diffusion Kurtosis Imaging (DKI) are used in the context of conventional Stejskal-Tanner sequences (constant gradient and spin-dephasing vector orientation). The natural logarithm of the dMRI signal can be expanded in powers of the wave number associated with the spin-dephasing vector around zero (corresponding to $b = 0$) [Kiselev, 2010]. In the absence of coherent spin flow, this so-called *cumulant expansion* writes [Basser et al., 1994, Lu et al., 2006]

$$\ln S = \ln S_0 - b \left[(\mathbf{n} \otimes \mathbf{n}) : \overline{\mathbf{D}} \right] + \frac{b^2}{2} \left[\frac{\mathrm{MD}^2}{3} \, (\mathbf{n} \otimes \mathbf{n} \otimes \mathbf{n} \otimes \mathbf{n}) : \mathbf{W} \right] \, , \tag{2.36}$$

where $\overline{\mathbf{D}}$ is the apparent diffusion tensor, $\mathrm{MD} = \mathrm{Tr}(\overline{\mathbf{D}})/3$ is the mean diffusivity, $\mathbf{W}$ is the apparent kurtosis tensor, and the expression $\mathbf{n} \otimes \mathbf{n}$ directly relates to the b-matrix [Mattiello et al., 1997]. While DTI corresponds to keeping the terms of the expansion up to b, DKI also includes the b^2 term.

DTI allows for the estimation of the mean diffusivity (MD) and the dimensionless fractional anisotropy (FA)

$$\mathrm{FA} = \sqrt{\frac{3}{2}} \left(1 + \frac{\mathrm{MD}^2}{V_\lambda(\overline{\mathbf{D}})} \right)^{-1/2} , \tag{2.37}$$

where $V_\lambda(\overline{\mathbf{D}})$ is the variance of $\overline{\mathbf{D}}$'s eigenvalues. The FA informs on the degree of macroscopic anisotropy, i.e., the voxel average of the diffusion anisotropy of all sub-voxel compartments. DKI allows for the estimation of MD, FA and the dimensionless mean kurtosis (MK)

$$\mathrm{MK} = \mathrm{Tr}(\mathbf{W}) , \tag{2.38}$$

which informs on the degree of sub-voxel diffusion heterogeneity, i.e., the presence of distinct diffusion compartments (in terms of diffusivity, anisotropy and/or orientation) within the voxel.

2.6.2 Gamma distribution approximation

Signals acquired with b-tensor encoding (Section 2.5.2) can be powder-averaged, i.e., averaged over acquisition directions, [Arvidson, 1977, Callaghan et al., 1979] to remove the explicit effect of these directions. After such powder averaging, the diffusion signal Equation 2.35 reduces to [Frisken, 2001, Koppel, 1972]

$$\overline{S}(b, b_\Delta) = S_0 \int_0^{+\infty} \overline{P}_{b_\Delta}(D) \exp(-bD) \, \mathrm{d}D , \tag{2.39}$$

where the distribution $\overline{P}_{b_\Delta}$ of effective diffusivities D depends on the normalised b-tensor anisotropy b_Δ, with $b_\Delta = 1$ for linear (PGSE-like) encoding and $b_\Delta = 0$ for spherical (isotropic) encoding, and on the subvoxel microstructure. Equation 2.39 can be more straightforwardly expressed upon finding a plausible approximation for the distribution $\overline{P}_{b_\Delta}$. The 1D gamma distribution [Röding et al., 2012] of mean $\overline{D}$ and variance μ_2 has been shown to provide a good approximation [Lasič et al., 2014], yielding the signal

$$\frac{\overline{S}(b, b_\Delta)}{S_0} = \left(1 + b \, \frac{\mu_2(b_\Delta)}{\overline{D}} \right)^{-\overline{D}^2/\mu_2(b_\Delta)} , \tag{2.40}$$

where $\mu_2(b_\Delta) = \mu_{2,\mathrm{iso}} + \mu_{2,\mathrm{aniso}} b_\Delta^2$ carries information about isotropic and anisotropic sources of kurtosis effects.

The fit of Equation 2.40 provides $\overline{D}$, $\mu_{2,\mathrm{iso}}$ and $\mu_{2,\mathrm{aniso}}$, which allow to recover microstructural features through the following formulas:

$$\mathrm{MD} = \overline{D} , \tag{2.41}$$

$$\mathrm{MK_i} = \frac{3\mu_{2,\mathrm{iso}}}{\overline{D}^2} , \tag{2.42}$$

$$\mathrm{MK_a} = \frac{3\mu_{2,\mathrm{aniso}}}{\overline{D}^2}\,, \tag{2.43}$$

$$\mu\mathrm{FA} = \sqrt{\frac{3}{2}}\left(1 + \frac{\overline{D}^2 + \mu_{2,\mathrm{iso}}}{\frac{5}{2}\,\mu_{2,\mathrm{aniso}}}\right)^{-1/2}\,, \tag{2.44}$$

where MD is the mean diffusivity, $\mathrm{MK_i}$ is the isotropic mean kurtosis, $\mathrm{MK_a}$ is the anisotropic mean kurtosis and μFA is the microscopic fractional anisotropy. In other words, the gamma distribution fit enables the disentanglement of the main contributions to DKI's mean kurtosis $\mathrm{MK} = \mathrm{MK_i} + \mathrm{MK_a}$ in Equation 2.38. Whereas $\mathrm{MK_i}$ informs on the variance of isotropic diffusivities across sub-voxel diffusion compartments, $\mathrm{MK_a}$ reports on both the degree of macroscopic anisotropy (like FA) and the degree of microscopic anisotropy (diffusion anisotropy of sub-voxel compartments without the effect of orientational coherence) within the voxel.

2.7 MR hardware improvements for advanced diffusion MRI

Routinely used clinical systems can reach maximum gradient amplitudes in the range of 40-80 mT/m. Thus, in recent years, various high-performance head-only [Foo et al., 2018, 2020, Versteeg et al., 2020, 2021, Webb, 2016, Weiger et al., 2018] and whole-body [Kimmlingen, 2017, Setsompop et al., 2013] strong gradient systems, e.g. with 300 mT/m capability, have been developed and conferred performance benefits for microstructural imaging [Jones et al., 2018, Kangarlu et al., 2004, McNab et al., 2013] in research and clinical studies [Genc et al., 2020, Huang et al., 2019, Kleban et al., 2020, Nilsson et al., 2017, Tax et al., 2020].

The use of high performance gradient systems provides several advantages, e.g., significantly reduced TE for a given b-value (faster diffusion encoding), which in turns boosts data SNR [Jones et al., 2018, Setsompop et al., 2013]. Moreover, shorter diffusion times are achievable in vivo, enabling a wider range of b-values to be maintained across a range of diffusion times, hence enabling a more precise characterisation of the water probability distribution function [Jones et al., 2018, Setsompop et al., 2013]. Therefore, the resolution limit, i.e., the lower bound of restriction lengths the diffusion-weighted MR signal is sensitive to, is lower, and thus microstructure of smaller dimensions can be characterised. Besides, the intrinsic low spatial resolution of dMRI images could be improved as the higher SNR obtained with stronger gradients could be traded-off at the cost of higher resolution. Achieving higher spatial resolution diffusion experiments could benefit the quantification of several microstructural properties because of reduced partial volume effects. Ultimately, systems equipped with ultra-strong gradients allow for the development of a truly translational pipeline, by making it feasible to perform measurements on humans that so far could only be achieved in animal studies on preclinical systems. As more powerful MR machines are becoming commercially available (e.g., Siemens Cima.X system), markers uniquely enabled by strong-gradient technology could play

a fundamental role in everyday clinical diagnosis. However, technical advancements also introduce additional challenges or concerns, such as additional artefacts in the data or exposition of patients to safety risks, which will be elaborated upon in Section 2.8.1 and 2.10.

Up to this point, most of the research with strong gradients was performed in the brain [Fan et al., 2022]. For example, it was shown that strong gradients enable different attenuation of the signal (so-called signal filtering) coming from intra-axonal and extra-axonal compartments, while maintaining reasonable TEs and thus sufficient SNR [Kleban et al., 2020]. The disentanglement of the contributions of (micro-)compartmental signals is essential for achieving a better understanding of healthy and pathological tissues. In the absence of strong diffusion weightings, parameters of the microstructural model are commonly fixed to a priori values to improve the precision of the to be estimated remaining model's parameters. If the fixed values have little or no biological plausibility, it may lead to biased estimates of the remaining parameters, decreasing their biological specificity [Jelescu et al., 2016]. In contrast, leveraging strong gradients unlocks a much larger portion of the multidimensional experimental parameter space, i.e., wider range of echo times accessible for a given diffusion weighting to be studied. This enables the estimation of more parameters, without having to fix them a priori [Jones et al., 2018, Novikov et al., 2019].

Strong gradients can have significant benefits in abdominal imaging, e.g., in the prostate. An overview of the clinical and research MRI frameworks for microstructural characterisation of the prostate, their limitations, and promises of ultra-strong gradients are described in Chapter 3, Section 3.4.

2.8 Magnetic field perturbations and their monitoring

2.8.1 MR field perturbations

The actual magnetic field patterns deviate from the nominal magnetic fields (Section 2.4) and lead to artefacts in the reconstructed images. Field deviations have different sources and can be categorised as perturbations originating from either physiological effects (e.g., subject or organ motion and tissue-susceptibility induced inhomogeneities) or MR system-related (e.g., eddy currents [Boesch et al., 1991], anisotropic gradient delays [Aldefeld and Börnert, 1998], mutual coupling of gradient channels, gradient cross-terms [Vannesjo et al., 2013], mechanical resonances [Wu et al., 2000], thermal effects, concomitant fields [Bernstein et al., 1998], and magnet drifts). If those field imperfections are not accounted for, it is plausible that the generated MR image contains inaccurate information and therefore should be interpreted with caution. The next sections provide a short overview of selected magnetic field perturbations and more detailed description can be found in textbooks [Bernstein et al., 2004, Webb, 2016].

2.8.1.1 Magnetic field inhomogeneities

Inhomogeneities in the static magnetic field B_0 [Morgan et al., 2004, Salomir et al., 2003] lead to local resonance frequency deviations (called 'off-resonance') and cause severe distortions in both

geometry and intensity - signal pile-ups along the phase-encode direction - of the MR images acquired using EPI readout. Those 'off-resonance' effects originate from magnetic susceptibility differences of the imaged object itself as well as from manufacturing tolerances of the main magnet [Webb, 2016].

To compensate for those at the acquisition stage, two approaches are usually taken, namely passive and active shimming. In passive shimming small pieces of sheet metal or ferromagnetic pellets are fixed at various locations within the scanner bore to improve homogeneity; this is usually performed at the installation of the MR machine by the vendor, thus independent of the scanner user. The active shimming method relies on small currents directed through specialised coils to generate supplemental magnetic fields that has the same spatial distribution, but reversed signs compared to the unwanted component. The optimal supplemental field is superimposed on the B_0 [Gruetter and Boesch, 1992, Turner, 1986] to cancel the remaining deviations from homogeneity; those steps are done prior to any imaging. For the experiments in this work on the Connectom MR system, up to second order spherical harmonic shim fields were deployed.

Furthermore, in abdominal imaging, e.g., of the prostate, the accurate compensation of susceptibility effects is particularly challenging as significant differences are observed over smaller spatial distances near different interfaces, such as the rectum (containing gas), bones and other soft tissues such as glands, muscles and fat. Therefore, for some imaging techniques with long readout trains that accumulate severe phase inconsistencies, an additional acquisition of a field map of the shimmed volume of interest must be recorded. The field map can be incorporated into the image reconstruction (please see Section 2.9.1) or can be leveraged at the data pre-processing stage to further improve data quality [Jezzard and Balaban, 1995]. A well established alternative distortion correction strategy, the so-called reversed-phase encoding correction [Andersson et al., 2003] can be also employed. Importantly, these approaches disregard the dependence of the susceptibility fields if the image object position is not fixed, however they include registration steps to the corrected data, and hence address subject motion to some extent.

2.8.1.2 Eddy currents

Eddy currents (EC) in conducting structures within the magnet and gradient/RF coils are induced by time-varying magnetic fields which are evoked by gradients used in MRI pulse sequences. EC induced fields add or subtract from the spatial encoding gradients, and as a result, affect the expected resonance frequency and lead to deterioration of image quality. The introduced effects will be mostly observed as image distortions, e.g., in EPI, as scaling, shearing and translation in phase-encoding direction [Haselgrove and Moore, 1996]. In general, the extent of these distortions will be unique to each diffusion sampling scheme and diffusion gradient shape used in any dMRI experiment as, e.g., one of the characteristics of EC is that they scale linearly with gradient amplitude of the diffusion gradients. Therefore, it is crucial to characterise the spatial and temporal dependence of the EC. If not accounted for they may result in inaccurate dMRI parameter estimates and imprecise delineation of imaged tissue [Pierpaoli, 2010, Zhang et al., 2017b].

There are many approaches to reduce EC effects. The MR system vendors employ an approach

called gradient waveform 'preemphasis' [Jehenson et al., 1990, Van Vaals and Bergman, 1990] which relies on purposely introduced distortions to the gradient driving currents, so that after EC act, the desired gradient waveform shape will be produced. In addition, EC effects can be addressed through modifications of the classical Stejskal-Tanner experiment [Alexander et al., 1997, Reese et al., 2003], dedicated optimisation of the diffusion gradients [Aliotta et al., 2018, Yang and McNab, 2019], modelling in post-processing [Andersson and Sotiropoulos, 2016, Nilsson et al., 2015], or accounting for at the reconstruction stage if the exact spatiotemporal information about EC information is available [Wilm et al., 2015] or including model-based reconstruction [Valsamis et al., 2022]. While EC effects cannot be completely eliminated at the hardware level, they can be minimised through dedicated gradient system design [Foo et al., 2020].

2.8.1.3 Concomitant magnetic fields

The linear G_x, G_y and G_z gradients employed in MRI create spatial variations along the B_z. However, once a linear gradient is applied to create a variation of B_z, other gradients are concurrently and unavoidably produced as a result of Maxwell's equations. The produced magnetic field components perpendicular to B_z cause the net magnetic field vector to deviate from the direction of the applied B_0 field and may also lead to the presence of higher-order spatial dependence of the amplitude of the magnetic field. The magnetic field corresponding to the higher-order terms is known as concomitant field, and the higher-order spatial terms are referred to as Maxwell's terms [Bernstein et al., 1998].

The strength of the concomitant field is proportional to the intentionally applied gradient and inversely proportional to the field strength. Therefore, for the Connectom gradients capable of a maximum of 300 mT/m, observed concomitant fields may be non-negligible (please see Section 2.8.2). Importantly, as the concomitant field is a result of the active gradient, it vanishes once the gradient is switched off. Nevertheless, short-term presence of the concomitant field leads to extra phase accumulation by the transverse magnetisation of a spin system that is spatially and temporally dependent. This may manifest itself as image shift, intensity loss, blurring [Baron et al., 2012] and therefore affect any dMRI data analysis [Irfanoglu et al., 2012].

The effects of concomitant fields can be removed through alterations of the gradient waveforms, e.g. symmetrisation, phase subtraction, or dedicated optimisation for asymmetric encoding [Szczepankiewicz et al., 2019] or during data reconstruction [Wilm et al., 2015].

2.8.1.4 Gradient non-linearities

MRI is based on the assumption that the z component of the total magnetic field created by the gradient coils varies linearly along three (x, y, z) perpendicular axes over imaging FOV. However, linearity can only be expected at the scanner isocentre, within a sphere of about a few centimetres in diameter. Deviations from linearity are expected further away from the centre. Therefore, the readout and diffusion encoding gradients can deviate substantially from the prescribed trajectories.

The degree of gradient non-linearity has its origin in the trade-off between gradient coil performance and its acceptable linearity decided at its design stage. Substantially higher gradient

amplitude and slew rate can be achieved if the spatial extent of the gradient linearity can be sacrificed, i.e., linearity over smaller FOV is satisfactory [Harvey, 1999]. Such a trade-off is attractive for application with imaging of a smaller FOV [Foo et al., 2020, Huang et al., 2021, Weiger et al., 2018]. However, improved system performance, i.e., achievable higher gradient amplitudes, with whole body capabilities have been also achieved [Kimmlingen, 2017, Setsompop et al., 2013].

Depending on the coil design, gradient non-linearity may require correction as it causes observable geometric image deformations and discrepancies between the expected and effective diffusion encoding gradients. Geometric distortions and associated signal intensity deviations occur because typical image reconstruction methods assume the data was spatially encoded using linear gradients. Moreover, b-matrix discrepancies resulting from gradient deviations are spatially varying, i.e., each voxel has a unique b-matrix for all combinations of b-values and gradient directions. The mismatch between how the signal was expected to be and how it was actually encoded, if not accounted for, may lead to significant biases in quantitative analysis. Therefore, it is crucial to correct the data during post-processing [Bammer et al., 2003] or account for these effects during reconstruction [Tao et al., 2015].

2.8.1.5 Mechanical oscillations

Another main cause of MR field perturbations are mechanical oscillations, or vibrations, of gradient tubes, [Hedeen and Edelstein, 1997, Hennel et al., 1999, Kessels, 1996, Mansfield et al., 1998] arising from fast gradient switching. Those oscillations, via reverse coupling from mechanics to electromagnetics, affect observed MR field stability, e.g., leading to magnetic field oscillation [Clayton et al., 2001], which also alters coil impedance [Winkler et al., 2018]. Those effects are especially noticeable at mechanical resonance frequencies [Foerster et al., 2005, Li et al., 2004, Winkler et al., 2018].

The mechanical behaviour of gradient coils has been extensively studied and accounted for in gradient design [Edelstein et al., 2002, Hedeen and Edelstein, 1997, Mechefske et al., 2004]. As part of these efforts, gradients have been modelled as general linear time-invariant (LTI) systems [Addy et al., 2012, Vannesjo et al., 2013] to capture direct electromagnetic as well as mechanical pathways of field perturbation. LTI models have been proven useful as a basis for, e.g., image reconstruction [Addy et al., 2012, Vannesjo et al., 2016] and for studying field perturbation by devices placed within the gradient range [Rahmer et al., 2019] (Section 2.8.2). However, despite covering diverse range of gradient behaviour, the time invariance assumption cannot be expected to hold strictly for more than a few years [Vannesjo et al., 2016] as gradient coils undergo physical change due to heating (Section 2.8.1.6).

2.8.1.6 Thermal effects

Gradient coils undergo physical changes in the short term as they heat up during operation, and thus their temporal stability is altered, especially during prolonged periods of high gradient duty cycle. Gradient heating is predominantly due to ohmic losses in the coils, and leads to increase

of the coil resistivity with time which affects its electromagnetic behaviour [Chu and Rutt, 1995, Freschi et al., 2016]. Even though the net current flowing through the coil may be hardly affected by change in resistivity [Doty, 1998, Sabaté et al., 2015], it does alter eddy currents within coil conductors and in other system parts subject to heating. The mechanical properties of gradient tubes also change with temperature [Webb, 2016]. Therefore, e.g., overall thermal shift of mechanical resonances over months exceeding the tolerances can be observed and is as suggested cause of time-dependent artefact in EPI time series [Kasper et al., 2015]. Currently, thermal heating is another key consideration in gradient system design [Chu and Rutt, 1995, Freschi et al., 2016, While et al., 2010, 2013].

2.8.2 Monitoring of MR field perturbations

There are approaches to efficiently address the MR system field perturbations through characterisation of the MR system properties assuming a certain model or directly measure them.

To serve this purpose, approaches such as Gradient Impulse Response Function (GIRF) modelling have been proposed to encode field errors [Addy et al., 2012, Vannesjo et al., 2013]. The GIRF is a linear time invariant system model for the gradient chain, capturing gradient delays and field oscillations. For a GIRF measurement, the MR system is perturbed with a set of input gradients, and field responses are recorded with either phantom-based methods or a dynamic field camera [Dietrich et al., 2016] (please see section below). The phantom-based methods typically measure only self-term GIRFs [Duyn et al., 1998], and B_0 cross-terms [Brodsky et al., 2013]. The advantage of the GIRF approach is that it does not require to be repeated for every change in the sequence protocol. Even though the GIRF framework was proven to be effective in, e.g., correction of B_0 EC [Robison et al., 2019], it suffers from low frequency resolution for diffusion gradients [van Gorkum et al., 2022].

An alternative approach for the characterisation of spatio-temporal MR field perturbations is based on the direct measurement of the field with magnetic field sensors. The direct recording of field dynamics is more comprehensive as NMR sensors record information with high sensitivity and temporal resolution [Barmet et al., 2008, De Zanche et al., 2008]. The magnetic field sensor consists of droplets of an NMR active substance suspended in a capillary around which a miniature RF coil is wound. Based on the phase of the FID signals from the NMR field measurement, the information about magnetic field magnitude at the probe positions is extracted. To encode the global field patterns, many NMR sensors are embedded into the receive coils to closely surround the volume of interest or assembled on a spherical frame as a standalone field camera device (please see Figure 2.5). The encoded information is expanded using, e.g., spherical harmonics of low order assuming that sufficient accuracy is thereby obtained. The temporal field evolution per se is retrieved by temporal differentiation of the probe phase expansion. Field-camera measurements provide both self-responses and cross-responses in a single measurement, thereby allowing the full characterisation of a multiple-input, multiple-output linear time invariant system [Vannesjo et al., 2016, 2013]. It is crucial to clarify that both approaches attempt to approximate the MR field perturbations either via modelling the fields with (a few) spherical harmonics as basis functions (NMR sensors) or modelling

them by the characterisation of the MR system itself (GIRF). However, the direct measurement with a field camera is more accurate than GIRF-based field characterisation, but has to be repeated for any change in the protocol. Nevertheless, incorporation of the directly measured field perturbation information into the MR image reconstruction demonstrated excellent image quality for several applications, including diffusion weighted imaging [Wilm et al., 2015].

An example of field perturbations over spiral readout event for the Connectom system for non-diffusion weighted and diffusion weighted acquisition with high gradient amplitude is shown in Figure 2.4.

2.9 Image reconstruction

As outlined in Section 2.4, the MR signal is acquired in k-space using a receive array and the inverse Fourier transform is applied to these raw data to decode (reconstruct) its position in image space [Fourier, 1822]. Ideally, the encoding matrix of the signal would account for, e.g., MR field perturbations, such as B_0 inhomogeneity (Section 2.8.1), to ensure the correctness of the decoding. Commonly, to accelerate data collection, undersampling and coil encoding techniques are employed. For that, so-called parallel MRI, multiple receive channels with per-channel spatially varying sensitivities are used, and those also have to be accounted for in the signal description.

Generally speaking, any image reconstruction from the sampled raw data constitutes the solution of a linear inverse problem. In the case of parallel MRI, a few reconstruction algorithms have been proposed to solve this problem, with two most outstanding and widely adapted by MR

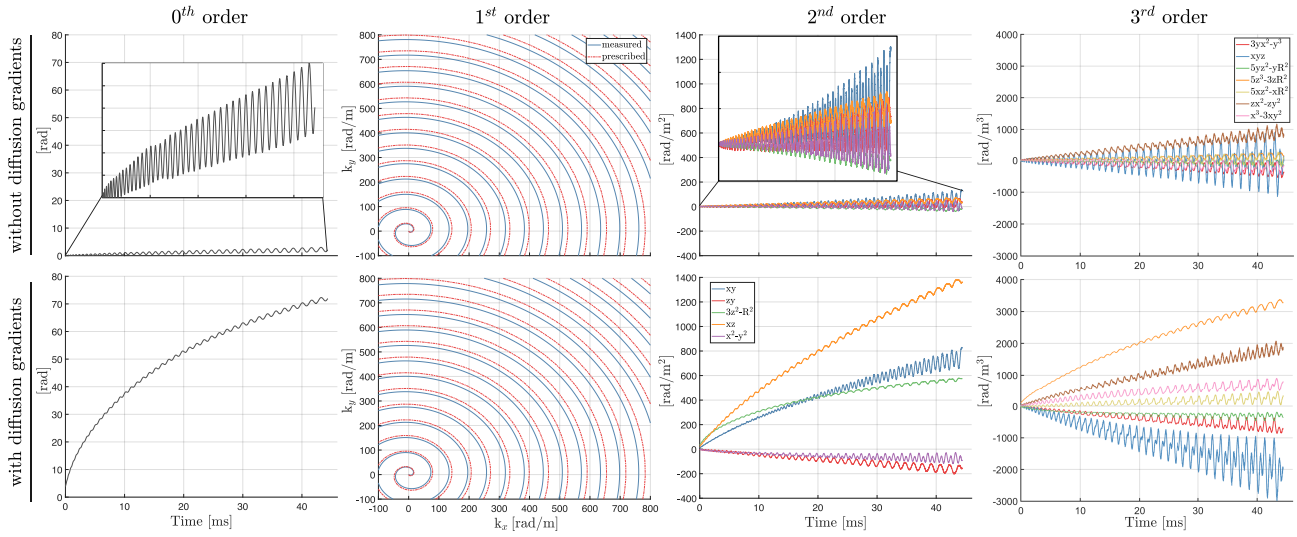

Figure 2.4: The maximum phase excursion within a sphere of 20 cm diameter relating to each (higher order) k-coefficient / basis function during a single-shot spiral readout without and with diffusion gradients is shown. Real-Valued Solid Harmonics up to 3rd order (not normalised) were used for the description. The plots are scaled within each column for direct comparison of the maximum phase changes that occurs within the same imaging slice without and with diffusion encoding. Insets show zoomed-in evolution of phase coefficients for 0th and 2nd order coefficients without diffusion gradients.

system vendors, namely SENSitivity Encoding (SENSE) [Pruessmann et al., 1999] and GeneRalized Autocalibrating Partially Parallel Acquisition (GRAPPA) [Griswold et al., 2002].

With GRAPPA, missing phase-encoding lines are estimated in the k–space domain. Importantly, additional lines in the centre of the k-space, called autocalibration signal (ACS), are acquired to provide calibration parameters. In short, a given missing k-space data point is recreated by combining the information contained in the local neighbourhood (kernel) near the estimated point as well as the 'parallel' neighbourhoods of the other coils with appropriate weights. While the kernels are shift-invariant over the entire k-space, they are specific to the target coils. Therefore, across channels, different weights are required to reconstruct a missing point. These weights are obtained from fully sampled ACS lines and describe the shift-invariant geometric relationships in the k-space coil data [Deshmane et al., 2012, Griswold et al., 2002]. Restored full k–space data for each coil channel is transformed to the image space and finally, e.g., simple operation of sum of squares is applied to combine channel data and create a single image.

Alternatively, the SENSE algorithm operates in the image domain. The undersampled data is transformed to the image domain with a resulting reduced FOV image in the phase encoding direction arising from aliased points in every channel. The number of aliased points ('folded' pixels) is defined by the undersampling factor, i.e., the parameter defining how many k-space points are missing. Thus, a single pixel in the reduced FOV image is a sum of equidistantly distributed pixels in the total FOV weighted by the intensity values of the fully sampled sensitivity profile at the spatial location of 'unfolding' pixels. The 'unfolding' process can be performed as long as the inversion of the encoding matrix is possible [Pruessmann et al., 1999]. Therefore, the undersampling factor cannot exceed the number of channels of the receiver coil.

The noise amplification from the acceleration of the data sampling can be quantified with a g-factor map, which is the ratio of the SNR for an optimal unaccelerated image and the SNR of the accelerated image with an additional acceleration factor which accounts for the SNR loss due to averaging fewer acquired signals. G-factor maps can be estimated independently of the reconstruction algorithm and solely depend on coil geometry, the undersampling factor, and object being imaged. SENSE algorithm performance is evaluated with use of the g-factor, which depends on the geometry of the multi-receiver coil, the object and the undersampling pattern and assesses how easily the inversion of the encoding matrix can be performed.

A significant part of this work (Chapter 6) uses an iterative conjugate gradient SENSE algorithm proposed to be able to cope with non-Cartesian trajectories [Pruessmann et al., 2001] and extended to account for field perturbations up to 3rd order (Section 2.8.2) [Wilm et al., 2011, 2015] and in the following will be referred to as 'expanded encoding model reconstruction' (Section 2.9.1).

2.9.1 Expanded encoding model reconstruction

The expanded encoding model, without the noise component, is defined as follows:

$$\sigma_n(t) = \int \rho(\mathbf{r})\, s_n(\mathbf{r})\, \exp\left(-i\left[\sum_l k_l(t) b_l(\mathbf{r})\right] - i\Delta\omega(\mathbf{r})t\right) \mathrm{d}\mathbf{r}\,, \tag{2.45}$$

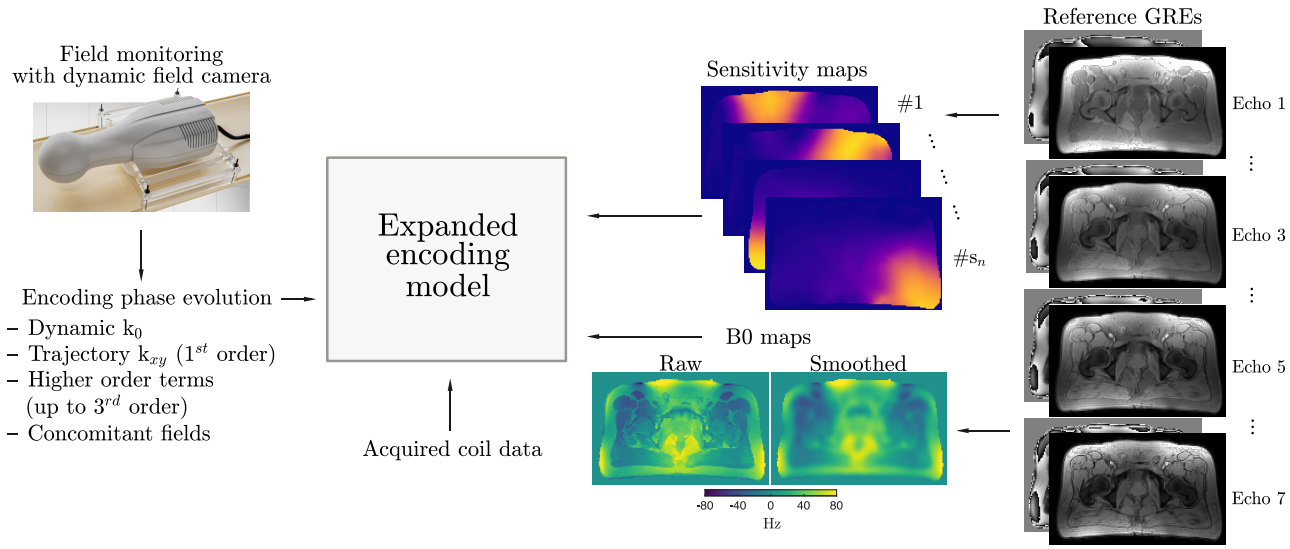

Figure 2.5: Schematic overview of the iterative conjugate gradient SENSE algorithm, so-called expanded encoding model reconstruction, given in Equation 2.46. Image data is formed using the acquired raw data and complemented by concurrently measured field dynamics as well as maps of receiver sensitivity and static B_0.

where $\sigma_n(t)$ is the MR signal acquired by the n-th receive coil at time point t, $\rho(\mathbf{r})$ is the transverse magnetisation as a function of position $\mathbf{r}$, $s_n(\mathbf{r})$ is the receive sensitivity of the n-th receive coil, $\Delta\omega(\mathbf{r})$ is the resonance offset due to static field inhomogeneity ΔB_0 at position $\mathbf{r}$, and the various $k_l(t)$ are the phase coefficients related to a spatial basis function $b_l(\mathbf{r})$ [Barmet et al., 2008, Wilm et al., 2011] describing global frequency fluctuations, conventional (first order) k-space, and higher order terms. The phase coefficients $k_l(t)$ are obtained by field monitoring (Section 2.8.2). Back-to-back calibration of the field sensors and acquisition of ΔB_0 maps ensures automatic accounting for subsequent field drifts.

Equation 2.45 describes signal encoding as a continuous function of the spatial and the temporal domain. Image reconstruction based on the expanded encoding model, i.e., the solution of Equation 2.45 for $\rho(\mathbf{r})$ is performed using a higher order iterative sensitivity encoding (SENSE) reconstruction [Wilm et al., 2011] in which the phase term for the correction of the static field non-uniformity is calculated directly. In brief, using linear algebra, it is straightforward to cast the image reconstruction problem, after combined temporal and spatial discretisation, as

$$\boldsymbol{\sigma} = \mathbf{E} \cdot \boldsymbol{\rho} \tag{2.46}$$

with $\boldsymbol{\sigma}$ denoting a vector comprising the acquired discrete signal samples, $\boldsymbol{\rho}$ listing the values of the initial transverse magnetisation along the chosen grid and $\mathbf{E}$ being the encoding matrix resulting from discretisation of the phase factor. The encoding matrix therefore reads

$$E_{(n,\kappa),\lambda} = s_n(\mathbf{r}_\lambda) \exp(-i\phi(\mathbf{r}_\lambda, t_\kappa)) \tag{2.47}$$

with $\phi(\mathbf{r}_\lambda, t_\kappa) = \sum_l k_l(t_\kappa) b_l(\mathbf{r}_\lambda) + \Delta\omega(\mathbf{r}_\lambda) t_\kappa$; here, κ, λ count the sampling time points and grid points, respectively.

The numerical solution of Equation 2.46 is a large linear inverse problem and gives rise to impractical computation times for typical image matrix sizes. Therefore, the conjugate-gradient method [Shewchuk et al., 1994] is implemented with GPU acceleration.

In our experimental framework, firstly, the spin-warp gradient echo images are reconstructed using nominal trajectories from which receive coil sensitivities, $s_n(\mathbf{r})$, and off-resonance maps, $\Delta\omega(\mathbf{r})$, are calculated. Subsequently, dMRI data is reconstructed using the measured coefficients $k_l(t)$ as well as estimated sensitivity maps and the off-resonance map for static B_0 off-resonance correction.

Figure 2.5 shows a schematic overview of the steps of the reconstruction algorithm.

2.10 MR safety

Even though MRI is a widely applied technique owing to its non-invasive diagnostic capabilities, the potential side effects of the employed non-ionizing electromagnetic fields are a concern for patient safety. The three different magnetic fields, namely static, gradient and radiofrequency may lead to elicitation of different physiological effects.

There have been no significant biological effects of static magnetic field [Schenck, 2000], with no apparent side effects for humans [WHO et al., 2006], apart from some sensory effects such as nausea, vertigo and metallic taste [Weintraub et al., 2007], during transitioning through the field as well as after positioning at isocentre. With regard to the physiological effects induced by RF electromagnetic wave (10 to 400 MHz), which energises the magnetisation vector allowing its detection by the MRI scanner, those are a major concern in ultra-high field MRI as the deposited power scales with the Larmor frequency. RF-induced physiological effects can be classified as non-thermal (arising from direct interactions between magnetic field and tissues), and thermal (due to tissue heating caused by the induced electric currents) effects [Polk, 1995].

Recent technical advances (Section 2.7) in gradient performance have led to tremendous improvements in MR imaging and have caused growing concern about safety aspects of MRI. As gradient magnetic field (100 to 1,000 Hz), which serves for the spatial localisation in the image reconstruction process, is often rapidly switching and thus producing rapidly time-varying, strong, magnetic fields over large spatial extent. Especially, MR systems equipped with gradients stronger than 100 mT/m can produce strong physiological effects, such as peripheral nerve stimulation (PNS) [Setsompop et al., 2013], magnetophosphenes [Brindley, 1955] or, in extreme cases, respiratory [Bourland et al., 1991] or cardiac muscle stimulation, e.g., an ectopic heartbeat [Irwin et al., 1970, Reilly, 1990]. While the latter is a primary concern, as heart muscle stimulation is a life-threatening condition, PNS may cause discomfort and could not be tolerated by the subjects, and thus would even result in a request to stop the MR exam. These phenomena effectively limit the extent to which ultra-strong gradients technologies can be used safely for in vivo imaging.

2.10.1 Peripheral nerve stimulation

While the fact that electric fields interact with nerves and muscles was established by Weiss [Weiss, 1901], the nature of this interaction was thoroughly investigated by Eccles, Hodgkin and Huxley when studying the nerve stimulation induced by extra-nerve-membrane electrodes [Frankenhaeuser and Huxley, 1964, Hodgkin and Huxley, 1952, McNeal, 1976, Rattay, 1986, Reilly et al., 1985]. Nerve stimulation occurs when the application of an extra-axonal electrical field pulse, above a certain threshold and with a non-zero component parallel to the main axis of the axon, generates an action potential. Reilly described the phenomenon of PNS [Reilly, 1989], an involuntary muscle twitch, induced by rapidly time-varying magnetic fields produced by switching gradient coils on and off.

Electrophysiological models, based on the Spatially Extended Nonlinear Node (SENN) model [Reilly et al., 1985], indicate that the applied electrical field must exceed a given threshold to generate an action potential. This threshold depends on the characteristics of the extracellular stimulus, e.g., single pulse or multiple pulses, monophasic or biphasic pulses, and the delay between consecutive pulses [Reilly, 1989]. Efforts have been made to minimise PNS effects by means of optimisation of the gradient pulse shapes, especially for MRI acquisitions such as EPI [Harvey and Mansfield, 1994, Irnich and Hebrank, 2009, Mansfield and Harvey, 1993]. Currently, the problem is addressed by considering more sophisticated human body models and the full map of gradient field produced by commercially available MR coils [Davids et al., 2019] as well as redesigning the wiring of MRI gradient coils with explicit PNS constraints [Davids et al., 2020].

In practice, as defined by the IEC Standard ISO/IEC-60601-2-33 [IEC 60601-2-33, 2015], the PNS limits for a scanner can be established by studying the PNS reported by a cohort of volunteers. During routine scanning, a dedicated model, implemented in system hardware and software, predicts the specific physiological limits for a given measurement [Hebrank et al., 2000].

2.10.2 Magnetophosphenes

Magnetophosphenes are most likely generated by stimulation of the retina. They are generally perceived as a sensation of flashing or a faint flicker spanning much of the field of view but are often reported in peripheral vision. Magnetophosphenes are a biologically reversible effect and thus are considered non-harmful. They are, however, a sensitive probe to the lower thresholds of the human physiological response to time-varying magnetic fields and are therefore considered useful in establishing thresholds of effects that are biologically irreversible [International Commission on Non-Ionizing Radiation Protection et al., 2010].

The production of magnetophosphenes had not previously been a problem with maximal achievable gradient amplitudes (up to 80 mT/m). However, initial work on an ultra-strong gradient system [Setsompop et al., 2013] reported magnetophosphenes when using gradient strengths greater than 130 mT/m, but only when the eyes were located more than 10 cm away from the isocentre. Thus, this physiological effect is particularly relevant for body applications, when the eyes are far away from the isocentre.

2.10.3 Cardiac stimulation

In contrast to model-based predictions of PNS, the cardiac stimulation thresholds in humans are based on animal experiments and electric field-to- $\mathrm{d}B/\mathrm{d}t$ conversion factors computed for a simple, homogeneous body model. Recent paradigm shift in MR safety evaluation, led to the development of a methodology of cardiac stimulation modelling using realistic body models and electrophysiological models of excitable cardiac fibres [Klein et al., 2021].

2.11 Sequence design and protocol optimisation considerations

The rationale behind informed sequence design and protocol preparation is three-fold.

Firstly, the minimisation of the risk to the participants and equipment, including receiver coils, of novel sequence development. For this, the programmers should be informed about MR system-specific properties, including hardware and software limitations, to perform safe experiments. For the safe operation of any system, gradient duty cycle, specific absorption rate (SAR), PNS, hardware (gradient) resonances, and cardiac stimulation should be investigated for any sequence programme. The hardware resonance 'forbidden' bands could be entered if, e.g., the applied gradient readout contains frequencies within that range and could potentially induce a system quench. Moreover, in the case of a system equipped with strong gradients, special consideration has to be taken with respect to PNS, low-frequency vibrations and even power-building supplies. For example, the strong gradient Connectom system is susceptible to gradient-table vibrations over a range of frequencies, but particularly at frequencies below 20 Hz. If a sequence contains significant frequency contributions below 20 Hz, programmers should be aware that some adjustments may be required to minimise vibration artefacts.

Secondly, sequence parameters should be optimised to maximise data quality, e.g., TE, repetition time (TR), BW, resolution (affecting readout length and, for EPI, TE), fat suppression (highly relevant in below the neck applications), among others. If a mistake is made in the trade-off of the set up parameters, e.g., low SNR, and artefacts in the data can substantially affect accuracy and precision of the validation of underlying tissue properties.

Thirdly, the maximisation of the usefulness of the information acquired from object per unit time. For this, the recent approaches of (any- or multi-)contrast protocol optimisation for any model [Alexander, 2008, Cercignani and Alexander, 2006, Lampinen et al., 2020, Panagiotaki et al., 2015, Slator et al., 2019] or scalar measures derived, e.g., from Diffusion Tensor Distribution (DTD) [Morez et al., 2022] could be leveraged.

Chapter 3

Clinical background: Prostate and Pathology of Prostate Cancer

Contents

3.1 Anatomy of the prostate gland

The prostate gland is located in the male pelvis, below the urinary bladder. Macroscopically, the prostate gland consists of lobes and is also described microscopically by zones. The prostate's muscle-driven mechanism allows the gland to switch between micturition and ejaculation.

The current prostate gland model is an output of the ground work from McNeal [McNeal, 1984], which states that the prostate is a highly heterogenous gland, composed of three glandular zones - peripheral (PZ), central (CZ) and transitional (TZ) - and a fourth non-glandular region - the anterior fibromuscular stroma. These different zones are tightly fused together within a common sheath of fibromuscular tissue - the capsule (Figure 3.1). The urethra passes through the prostate gland, and the prostatic urethra consists of two segments, proximal and distal [McNeal, 1975, 1972], where the distal segment joins with the two ejaculatory ducts.

The PZ is the major glandular component of the prostate (around 65%), with ducts extending posterolaterally and anteriorly from the urethra to the prostatic apex [McNeal, 1968]. The second major component of the normal glandular prostate, the CZ (around 30%), surrounds the ejaculatory ducts and branches from mid-prostate to the prostatic base [McNeal, 1968]. The TZ encompasses approximately 5% of the gland volume, and extends bilaterally from the middle to the base of the gland along the proximal urethra [McNeal, 1978].

At the cellular point level, the prostate consists of glandular and connective tissue. The glandular structure of the prostate consists of ductal lumen surrounded by secretary epithelial cells. The highly variable epithelial cells are differentiated into two groups, namely, the luminal (layer), which is composed of columnar epithelial cells, and the basal (layer), which is composed of cuboidal epithelial cells. The connective tissue of the prostate is made up of fibrous tissue and randomly

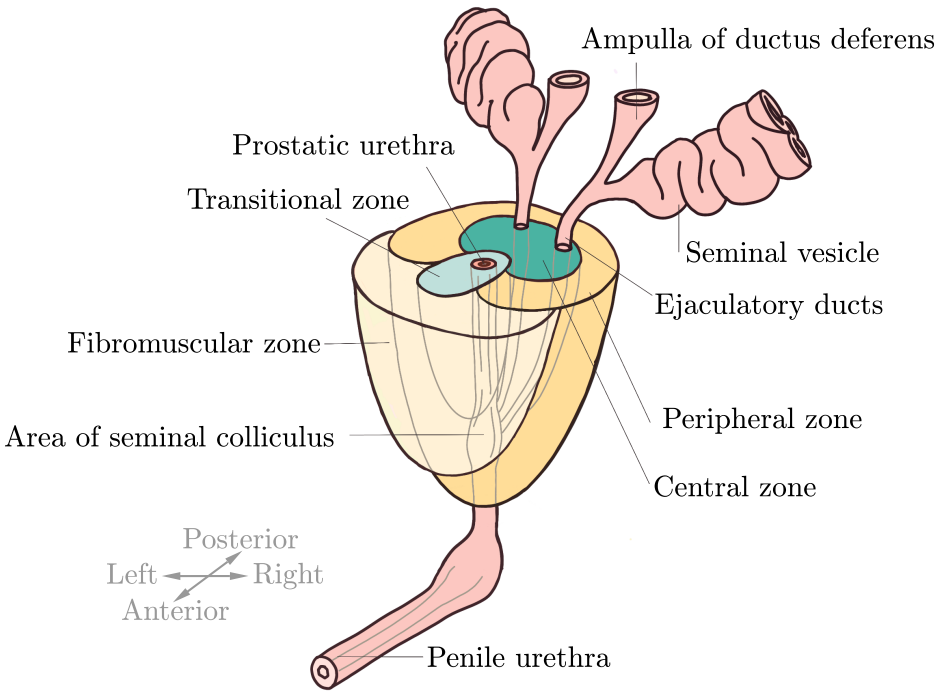

Figure 3.1: Diagram showing the zonal anatomy of the prostate. Drawing by AR.

orientated smooth-muscle bundles. It either separates the gland into lobules (fibrous tissue) or, if mixed with glandular structures (muscle bundles), supports the gland structure.

3.2 Clinical diagnostic pathway and relevance of MRI in the detection of prostate cancer

After the prostate-specific antigen (PSA) level assessment from the blood sample, and digital rectal examination, men with suspected prostate cancer should undergo further investigation.

The traditional diagnostic pathway used transrectal ultrasound (TRUS) guided prostate biopsy to acquire systematic information on 12 core regions (from the apical, mid, and basal) of the prostate with needle biopsies. Although the accuracy of this approach has improved over time, its sensitivity remains only 48% for the diagnosis of one definition of 'clinically significant' cancer (defined as Gleason grade 4+3 or more (see Section 3.3), or a maximum cancer core length of 6 mm or more) [Ahmed et al., 2017]. However, this random process of tissue sampling does not allow for a trackable location of the positive lesions on repeat biopsies. Furthermore, studies have demonstrated that conventional TRUS biopsy is relatively poor in terms of tumour localisation and estimation of tumour grade (under detection of high grade csPCa and over detection of low grade non-csPCa [Abraham et al., 2015, Caverly et al., 2016]), whilst the risk of serious adverse events such as sepsis or bleeding is around 6% [Ahmed et al., 2017, Bennett et al., 2016, Mowatt et al., 2013].

Considering these limitations, the new-standard diagnostic pathway, which has become standard of care, involves mpMRI comprising of T2-weighted, diffusion weighted and dynamic contrast enhanced sequences prior to biopsy. A number of studies have demonstrated increased sensitivity and specificity when a standardised reporting system (the Prostate Imaging Reporting and Data System; PI-RADS [Weinreb et al., 2016]) is utilised [Zhang et al., 2017a]. The latest PI-RADS v2.1 defines primary and secondary MR sequences for peripheral zone and transition zone prostate imaging and enumerates findings to categorise the nature, i.e., benign or malignant, of prostate tissue changes.

Recently published studies comparing mpMRI and TRUS biopsy against transperineal template prostate mapping biopsy as the reference standard (PROMIS trial) demonstrated superiority of mpMRI in terms of sensitivity but lower specificity for diagnosis of csPCa [Ahmed et al., 2017]. The results suggested that mpMRI could be used as triage test, and thus, it would allow 27% of patients to avoid biopsy, and would yield a 5% decreased diagnosis of non-csPCa. More recent studies, established that application of mpMRI prior to biopsy would avoid unnecessary interventions in 49% of the patients who had non-concerning lesions on the MRI, and that TRUS biopsy over-detected non-csPCa in 20% of the patients (4M - Met Prostaat MRI Meer Mans - study) [van der Leest et al., 2019]. Other advantages of mpMRI over TRUS biopsy is that when combined with Gleason grade (Section 3.3) of the cancer and serum PSA level, it provides powerful prognostic information, thereby facilitating risk stratification, and aiding treatment decision making [Boorjian et al., 2008], and assessment of the pelvis for lymph node metastases.

3.3 Microstructural changes of the prostate tissue

In 1966, a new system capturing the complex architectural heterogeneity of prostate cancers was proposed by Gleason [Gleason, 1966], and since then, it has been widely applied in clinical settings. The current version of the five-tier grading system (Figure 3.2) consists of detailed descriptions of the individual architectural patterns [Epstein et al., 2016, Magi-Galluzzi et al., 2016]. It is designed to help grade microstructural changes over time, and therefore directly impacts the patient's prognosis. For an extensive overview of the various sub-patterns constituting the individual Gleason grades please refer to [Kweldam et al., 2019].

Healthy prostate tissue with three main compartments, i.e., ducts, epithelial cells, and stromal cells is depicted in Figure 3.3 (*left column*). Based on the histological validation, general characteristics of prostate cancer are increased cellularity, increased epithelial volume fraction and decreased lumen area (Figure 3.3, *middle and right column*). Overall, about 70% of prostatic cancers originate from the PZ of the gland, while the CZ and TZ account for less than 5% and roughly 25-30% of prostate cancers, respectively [McNeal et al., 1988]. The aforementioned tissue changes lead to a decrease in the diffusivity of water, which is reflected by lower ADC values and shorter values of relaxation rates, T_2 and T_2^*, especially in more aggressive cancers [Desouza et al., 2008, Wu et al., 2016]. Studies have shown that ADC values correlate inversely with tumour grade [Desouza et al., 2008, Vargas et al., 2011]. Conversely, low grade tumours and histologically sparse tumours have intermixed normal tissue and thus ADC and T_2 values in these tumours are similar to normal prostate tissue [Langer et al., 2008]. Despite the proven utility of mpMRI (Section 3.2), the complexity of

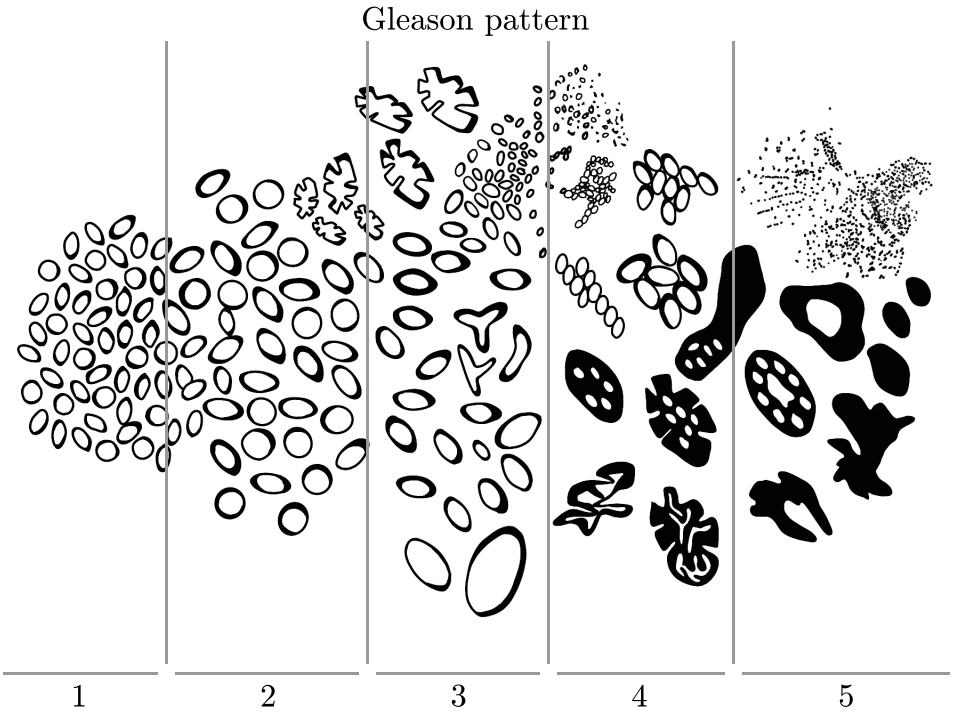

Figure 3.2: Illustration of the current state of Gleason grading based on 2014 ISUP consensus [Epstein et al., 2016]. Drawing by AR based on the original version published in [Epstein et al., 2016].

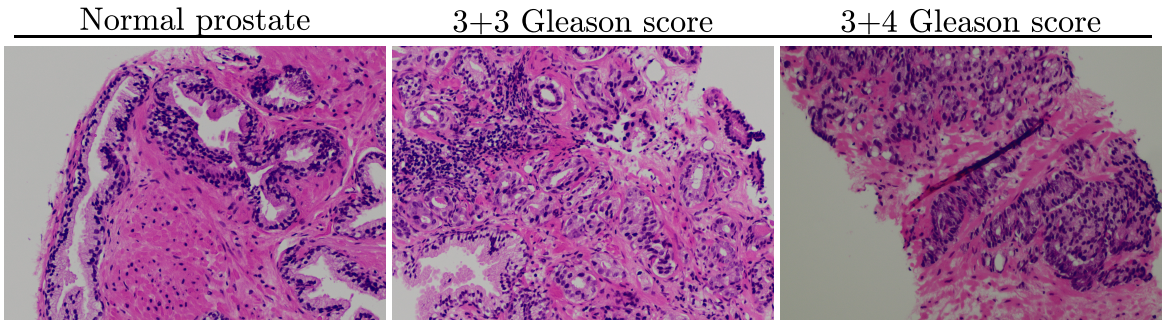

Figure 3.3: Depiction of prostate microstructure in normal and cancerous tissue - 3+3 and 3+4 Gleason score (GS) subpatterns. Image courtesy of Dr Hywel Thomas from Department of Cellular Pathology at University Hospital of Wales.

the cancerous lesions [Kweldam et al., 2019] is not comprehensively captured with clinical scans, and therefore there is a need to improve the specificity and accuracy of non-invasive MRI, especially for diagnosis of low grade tumours.

It should be noted that prostate cancer is not the only pathology affecting microstructure of the prostate gland, and thus there is high likelihood that benign pathologies, such as focal prostatitis in the PZ, can mimic PCa, thus additionally increasing false positive reads of mpMRI scans. Other benign conditions, e.g., post-biopsy hemorrhage, inflammation, focal prostate atrophy, benign prostatic hyperplasia nodules (in the PZ and TZ), and prostatic calcifications can also affect diagnostic accuracy [Chatterjee et al., 2020].

3.4 (In)visible histological changes in clinical prostate MRI: Research studies on prostate cancer

Although proven extremely valuable to identify whether a patient has clinically significant prostate cancer (sensitivity between 93-96% at patient-level) [Ahmed et al., 2012, Thompson et al., 2016], current mpMRI as advised in PI-RADS v2.1, suffers from low sensitivity on the per-lesion basis. Around half of the individual tumour foci are undetected on mpMRI [Johnson et al., 2019, Lee et al., 2018] and the size of large lesions tends to be underestimated [Borofsky et al., 2018, Bratan et al., 2015, Priester et al., 2017]. mpMRI has limited specificity for significant cancer (Gleason score $\geq$ 3+4) [Ahmed et al., 2017] and approximately 50% of lesions biopsied are not found to contain significant cancer. The current diagnostic goal is to detect all lesions that contain significant cancer whilst avoiding the detection of clinically non-significant (Gleason score $\leq$ 3+3) disease, as detecting non-significant disease is not associated with increased mortality and can lead to increased anxiety and overtreatment. Results from a recent study [van Houdt et al., 2020] conclude that the lesions that are undetected on mpMRI have different histopathology features than visible regions. In light of those limitations, which have direct implications on monitoring and focal treatment strategies, a few novel research strategies have attempted to address these limitations and provide an opportunity to address these shortcomings [Singh et al., 2022]. A 'virtual imaging biopsy' biopsy of the prostate

would allow accurate detection of all tumours within the gland, and for low-grade non-significant and small significant cancers to be safely monitored on interval imaging with treatment reserved for those with high-grade or progressive disease.

The extent of different microstructure characteristics, e.g., cellularity or tissue organization, requires optimization of (joint relaxation-)diffusion MRI scans. The diffusion encoding that is classically performed is the Stejskal-Tanner sequence, i.e., linear tensor encoding with trapezoidal gradients (Section 2.5.1). Information obtained in these measurements, depending on the parameters of the actual protocol, can be described using standard DTI and DKI representations (Section 2.6), as well as, more advanced biophysical models, such as Vascular, Extracellular and Restricted Diffusion for Cytometry in Tumours (VERDICT). The VERDICT model [Panagiotaki et al., 2015] consists of three compartments: a restricted spherical intracellular compartment (i.e., non-trivial isotropic compartment, reflecting epithelium), a non-restricted 'zeppelin' extracellular compartment (i.e., single anisotropic compartment, reflecting stroma and lumen), and a non-restricted 'astrostick' compartment (i.e., powder of stick-like tensors, reflecting vasculature). The measured diffusion signal is weighted by the volume fraction of the signal arising from different compartments. Recently, VERDICT analysis of mpMRI data (INNOVATE study) showed that many unnecessary biopsies can be avoided [Singh et al., 2022].

If the measurements are acquired at different TEs, a joint relaxation-diffusion ($T_2 - D$) analysis can be performed via means of a simple three pool model (e.g., hybrid multidimensional MR imaging, HM-MRI) or the extension of VERDICT analysis, called relaxed-VERDICT (rVERDICT). The HM-MRI technique [Chatterjee et al., 2018], has great potential to improve the diagnosis of prostate cancer and determine its aggressiveness, as fractional volumes of prostatic lumen, stroma, and epithelium, estimated non-invasively and by pathologists, are similar to the true tissue composition [Chatterjee et al., 2022a]. Furthermore, biophysical modelling accounting for relaxation effects, implemented using the deep learning framework, rVERDICT, allows for accurate, fast and repeatable estimation of diffusion and relaxation properties of PCa and can discriminate Gleason grade groups [Palombo et al., 2020b]. In another study, diffusion time-dependence effects in $T_2 - D$ space were explored [Lemberskiy et al., 2018], concluding that diffusion and transverse relaxation is comprised of at least two biophysically distinct contributions, lumen (long T_2 and fast diffusion), and stroma (short T_2 and heavily restricted anisotropic diffusion), with both manifesting non-Gaussian behaviour.

Alternatively, if the encoding gradients have more complicated shapes, such as oscillating gradients (OGSE), or beyond being arbitrary, are also applied in three encoding dimensions at the same time (b-tensor encoding, Section 2.5.2), sensitivity to particular tissue properties can be gained. A combination of any arbitrary diffusion encoding waveforms can be leveraged in frameworks such as Imaging Microstructural Parameters Using Limited Spectrally Edited Diffusion, IMPULSED [Jiang et al., 2017, 2016], or using Q-space Trajectory Imaging, QTI [Westin et al., 2016]. In brief, the IMPULSED model combines multiple low-frequency OGSE measurements and a single PGSE acquisition in the long time regime to quantify the characteristic size of restriction and intracelullar fraction. A recent study [Wu et al., 2022], reported that time-dependent diffusion MRI–derived parameters, especially the cellularity index, achieve superior accuracy in discriminating csPCa from

clinically insignificant disease. The feasibility of multidimensional encoding dMRI (MddMRI) in assessing prostate tissue diffusion heterogeneity and anisotropy at different spatial scales was assessed by [Nilsson et al., 2021] and [Langbein et al., 2021], with conclusion that MddMRI provides novel information about isotropic microscopic kurtosis as well as microscopic anisotropy, which differ from measures at the macroscopic level.

In summary, research studies present a tremendous springboard for prostate cancer characterization using frameworks beyond clinically adapted archetypical Stejskal-Tanner encoding and the quantitative ADC map. More advanced acquisition and data analysis approaches, provide a unique opportunity for better understanding of the anatomical regions and pathways involved in prostate cancer using non-invasive, in-vivo techniques, so-called 'virtual pathologic examination'. However, clinical adoption of many advanced MRI techniques with more sophisticated post processing is relatively slow. The low SNR, poor spatial resolution, and exacerbated image distortion at high b-values are among the technical impediments for clinical adoption of these promising techniques.

Part II

Contributions

Chapter 4

Physiological effects of human body imaging with 300 mT/m gradients

Contents

4.1 Introduction

As described in Section 2.7, technical advances in gradient performance (including the availability of higher amplitude gradients) have led to tremendous improvements in MR imaging. However, it was also established, that rapid switching of ultra-strong gradient systems elicits physiological effects in the human body, such as PNS (Section 2.10.1), magnetophospehens (Section 2.10.2), and cardiac stimulation (Section 2.10.3). These phenomena effectively limit the extent to which ultra-strong gradient technologies can be used safely for in vivo imaging.

The Siemens 3T Connectom is a whole-body system with ultra-strong gradients (300 mT/m gradient amplitude and 200 T/m/s slew rate) [Jones et al., 2018, Kimmlingen, 2017, Setsompop et al., 2013]. The system was originally designed for neuroscience research but there is increasing interest in using the system's ultra-strong gradients 'below the neck', e.g., in heart and prostate [Tang and Zhou, 2019].

The rationale for the use of ultra-strong gradients in body applications is the collection of diffusion-weighted data with higher b-values and a range of shorter diffusion times which are available using a Connectom system [Jones et al., 2018]. In prostate MRI, high b-value data can give novel insights into cellular restrictions in the tissue undergoing cancerous changes. In clinical practice, high b-value data is challenging to acquire due to hardware limitations, and is extrapolated from the data acquired with lower b-values assuming a mono-exponential relationship between ADC and b-values [Sahoo et al., 2020] (an assumption that is invalid in the case of restricted diffusion). In heart imaging, although the required b-values are lower than for prostate MRI, using stronger gradients allows for the same b-value in shorter time, resulting in shorter echo time (which is limited by the short T_2 of the heart tissue). Additionally, due to cardiac motion, higher gradient moments encoding for, e.g., coherent flow, have to be compensated, which increases the encoding time needed for the same b-value and therefore leads to longer TEs. This effect can be counteracted using strong gradients.

As the IEC Standard ISO/IEC-60601-2-33 [IEC 60601-2-33, 2015] does not define a regulatory limit for magnetophosphene stimulation, nor a procedure for defining this limit in practice. The aim of this study was to evaluate the probability of eliciting magnetophosphenes to develop a practical guideline for minimising participant discomfort and/or anxiety.

4.2 Methods

4.2.1 Study participants

Ethical approval for the study was obtained from the School of Psychology Research Ethics Committee of Cardiff University. Fifteen participants were recruited for this study (age range: 27-50 years, M = 38.87, SD = 7.17, weight: M = 77.73 kg, SD = 9.59 kg, height: M = 178.6 cm, SD = 6.39 cm; M - mean, SD - standard deviation). All participants were male (to define a prostate landmark) and had no disclosed medical problems that would influence the validity of the results.

Participants had provided informed consent prior to participation and had taken part in previous MRI studies. Participants were informed in advance that the aim of the study was to investigate physiological effects and were briefed on the likely physiological effects that might be experienced to ensure that these effects could be detected.

4.2.2 Experimental setup

The imaging system used in the study was a Connectom MRI scanner, a modified 3T MAGNETOM Skyra system fitted with an AS302 gradient coil capable of 300 mT/m (Siemens Healthcare, Erlangen, Germany). To assist in providing a reference to other works, the vendor supplied maps of the maximum absolute magnetic field of the gradient coil (excluding main magnet B_0) allowing the peak $\mathrm{d}B/\mathrm{d}t$ during the experiment to be estimated (Figure 4.1 A.).

Participants were placed on the scanner table in the supine position prior to data collection from three anatomical regions: head (head first), heart (head first) and prostate (feet first). In each case, the participant's left arm was positioned flat on the table alongside the left hip and their right hand on an optical fibre-interfaced 5 button response box (LxPad, NATA Technologies, Coquitlam, Canada) placed on the abdomen. This device was used to receive feedback from the participants on the experience of the physiological effects. In line with our institute's standard procedures, the participants were also supplied with an alarm call button and a pulse-oximeter (placed on the left hand index finger) to monitor the cardiac cycle. The participants were instructed not to move. The scanner vendor's standard pneumatic headphones and earplugs were used to limit acoustic noise. To increase the sensitivity to any visual effects, the ambient light in the scanner room was reduced to a minimum; the magnet and control room lights were switched off and any remaining light originated from monitor displays. Lastly, absolute distances between the nasal area and the end of the sternum (heart position) and hip bones (prostate position) were measured (Figure 4.1 B.).

4.2.3 Acquisition protocol

We assessed the occurrence of magnetophosphenes in participants when applying a continuous train of 128 trapezoidal bipolar gradient pulses, similar to that used in a conventional EPI read-out. Each gradient pulse train was applied along a single gradient axis with ramp times ranging from 0.88 to 4.20 ms and gradient amplitudes from 60 to 300 mT/m. These ranges were constrained by the MR system's physiological limit monitors. The gradient amplitude/ramp time combinations used in the study were defined by performing a preliminary investigation of magnetophosphenes on three MR-experienced participants.

Data were sampled from the lowest gradient/shortest ramp time to the strongest gradient/longest ramp time (70 combinations, gradient variation first), for each of the three imaging landmarks (head, heart, prostate), for each gradient axis (X, Y, Z), resulting in 630 stimuli for each participant. The sampling of the gradient/ramp time combinations was weighted towards the high-gradient/long-ramp time measurements, as the low-gradient/short-ramp time measurements had been previously performed by the vendor.

The gradient axes are defined as follows: When standing in front of the scanner and looking into the magnet, the X-axis points from left to right (horizontal axis); Y-axis points from bottom to top (vertical axis); Z-axis points from rear to front (depth axis). After each gradient stimulus, the participants were asked to indicate via a button press whether they experienced; (a) no effects, (b) PNS, and/or (c) magnetophosphenes. In the event of any other perceived effects, participants were instructed to use the scanner alarm call button to report this to the experimenters. The participants were not aware of the order of applied gradient amplitude/ramp time stimuli. The only imaging performed was a localiser for landmark identification using the whole-body RF coil to verify participant positioning.

From the observations across the cohort, an estimate of the probability of encountering physiological effects was established; the probability was calculated as a ratio of counts of the reported effect (PNS or magnetophosphenes) to the number of samples collected for each ramp time and gradient amplitude combination.

The main aim of the study was to quantify the reports of PNS and visual effects. To capture any other physiological effects experienced by the participants, a post-scan questionnaire was administered immediately after the experiment. The questionnaire was designed to establish subjects'experiences during the experiment, and to obtain any other effects not reported during the tests and their reflections pertaining to the experimental study.

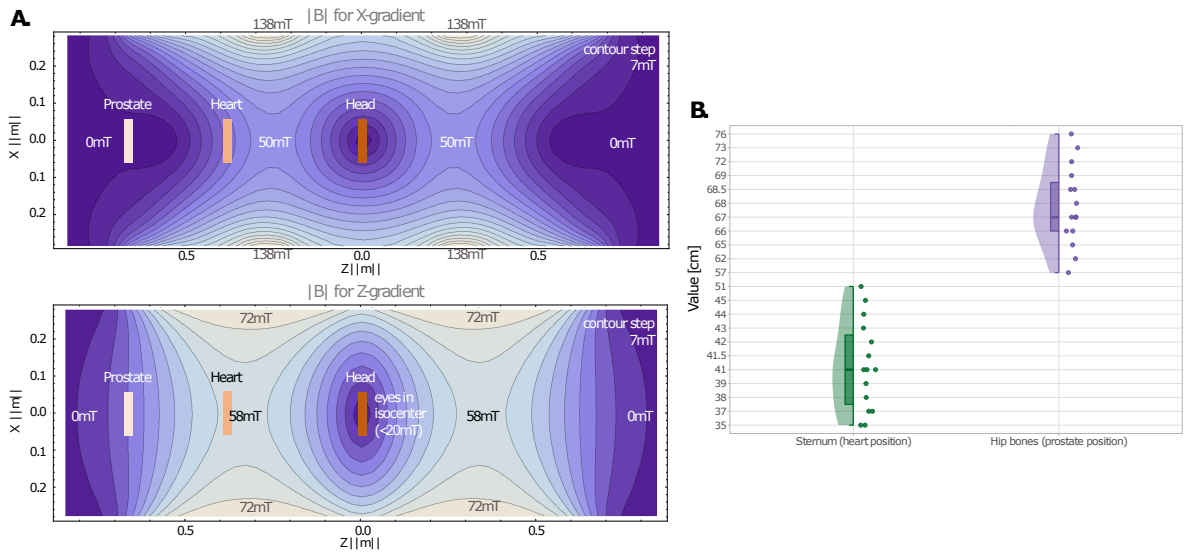

Figure 4.1: **A.** Contour plots of the absolute magnetic field generated by the gradient coil used in this study. X-axis corresponds to left-right, Y-axis to anterior-posterior, and Z-axis to head-foot directions. To aid in the interpretation of the magnetophosphene results, the approximate position of the eyes for the prostate, heart and head positions are shown (rectangular boxes). *Top row:* $|\mathrm{B}|$ for a 300 mT/m X-gradient $(Y = 0)$. Note the plot for the Y-gradient is substantially similar to X-gradient, and thus, only X-gradient is shown for the illustrative purposes of the current figure. *Bottom row:* $|\mathrm{B}|$ for a 300 mT/m Z-gradient $(Y = 0)$. **B.** Descriptive analysis of measured absolute distances between the nasal area and the body landmarks for the study population. Dots represent measured lengths, the half violin plot represents the distribution of measurements in the study sample and the half box plot represent the median and interquartile range: 41 cm, IQR = 5 cm and 67 cm, IQR = 2.75 cm for heart and prostate landmarks, respectively. Please note that Y-axis grid spacing is not uniform.

4.3 Results

All study participants successfully completed the experiment and were able to provide valid responses during the experiment and feedback via the post-scan questionnaire.

4.3.1 Occurrences of magnetophosphenes

Magnetophosphenes were reported by most participants in at least one landmark position, as shown in Figure 4.2. These visual effects were more widely reported when the gradient amplitude was above 150 mT/m, for which the gradient ramp times are longer. For the highest gradient amplitudes, when the corresponding gradient stimulus ramp times were above 3 ms, magnetophosphenes were reported by up to 86.7% of the participants (for the heart landmark); for lower gradient amplitudes, when ramp times were below 3 ms, fewer than 30% of participants reported magnetophosphenes.

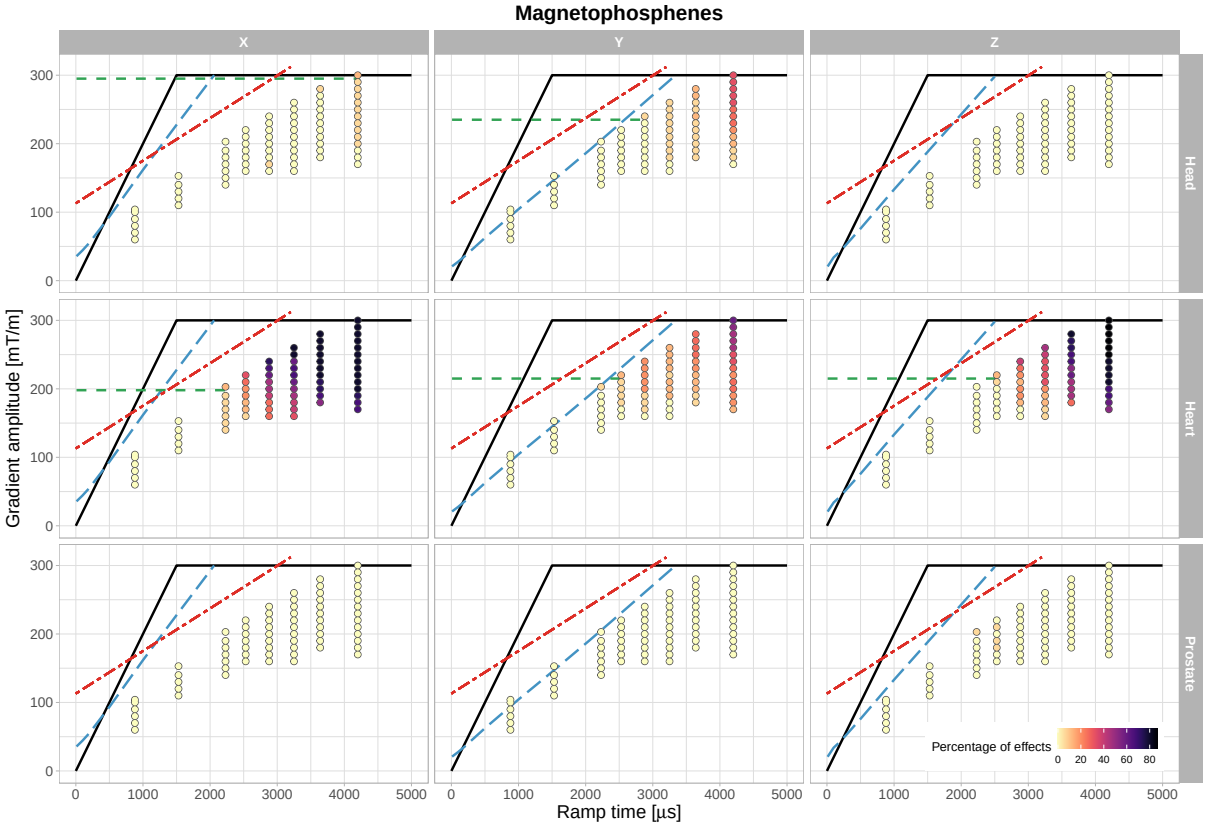

Figure 4.2: Percentage of participants reporting magnetophosphenes for the three imaging landmarks and three gradient axes. The dots are colour-coded according to the percentage of volunteers reporting the effect for each of ramp time/gradient amplitude pair. The hardware limit (maximum slew rate and maximum gradient amplitude) is depicted as a solid black line, the approximate location of the cardiac stimulation limit is shown as a red dot-dashed line and the PNS limit (SAFE model [Hebrank et al., 2000], for X, Y, Z axes separately) is shown as a blue dashed line. As outlined in the discussion, the magnetophosphene guideline value, G_{amp}, is shown as a green dashed line. This represents the maximum gradient amplitude, at the maximum slew rate, for which fewer than 10% of participants reported magnetophosphenes. This is not defined where the guideline value is greater than 300 mT/m.

Participant reports of magnetophosphenes varied greatly between experiments performed in the different landmark positions. For the heart landmark, 80%, 60%, and 86.7% of the study participants reported perceivable changes in vision during the experiment for the X, Y, and Z-axes respectively. In the other landmark positions, there were fewer reports of magnetophosphenes, notably in the prostate position (6.7% of participants). For the head position, 33.3% of participants reported magnetophosphenes when the stimulus was applied along the Y-axis; however, these were rarely reported on the X-axis (13.3%) and not reported at all when pulsing the Z-axis.

4.3.2 Occurrences of PNS

The highest incidence of PNS (Figure 4.3 and Table 4.1) occurred when the gradient was applied along the Y-axis, where 66.7% of the study volunteers reported some degree of PNS (head or heart positions). In contrast to magnetophosphenes, PNS was less common when applying gradients with longer ramp times, with participants reporting PNS in less than 20% of the cases when the ramp time was greater than 3 ms. PNS was less prominent when the stimulus was applied along the X- or Z-axis. There was no dramatic effect of imaging landmark on the PNS probability, as can be seen from Table 4.1.

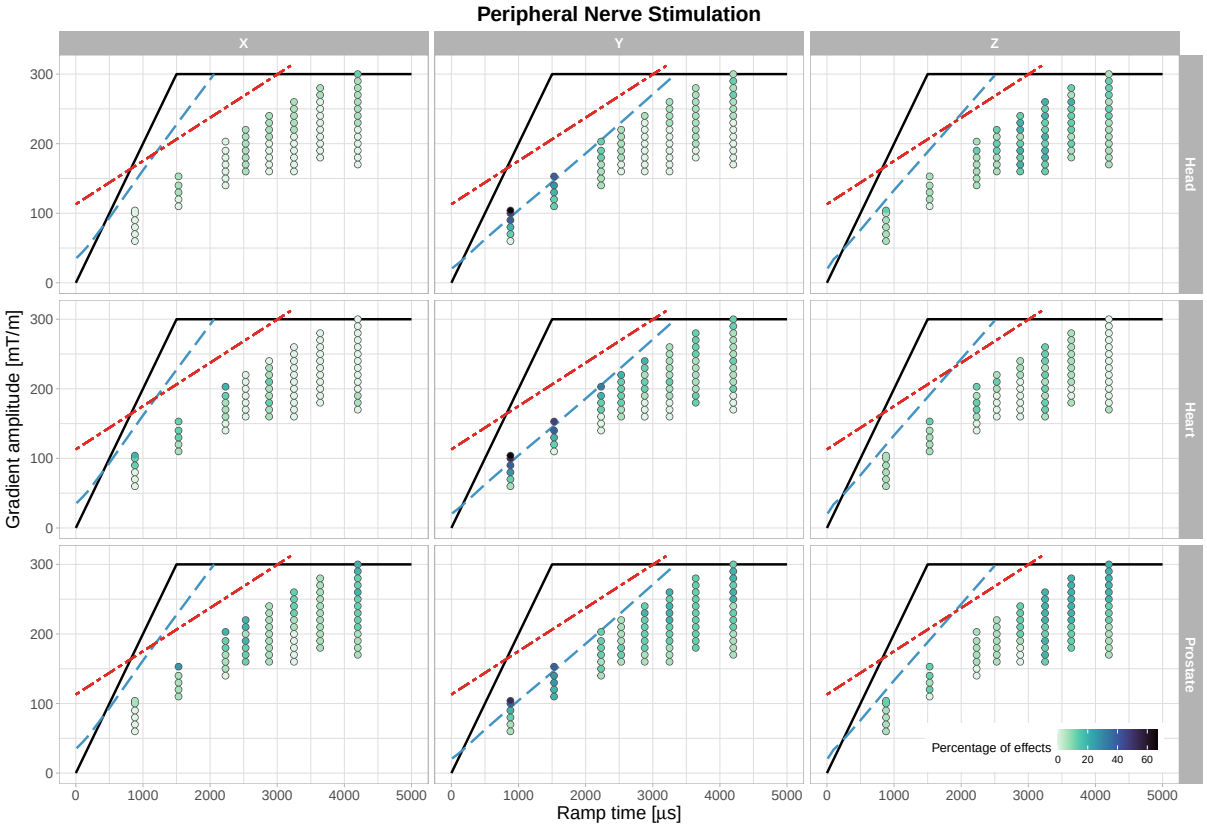

Figure 4.3: Percentage of participants reporting PNS for the three imaging landmarks and three gradient axes. The dots are colour-coded according to the percentage of volunteers reporting the effect for each of ramp time/gradient amplitude pair. The hardware limit (maximum slew rate and maximum gradient amplitude) is depicted as a solid black line, the approximate location of the cardiac stimulation limit is shown as a red dot-dashed line and the PNS limit (SAFE model [Hebrank et al., 2000], for X, Y, Z axes separately) is shown as a blue dashed line.

Table 4.1: Summary of the perceived physiological effects (magnetophosphenes and PNS) in three body imaging landmarks for the X, Y, Z axes. Values represent the highest percentages of participants experiencing effects for each landmark-axis pair among the tested ramp times-gradient amplitude combinations.

	Magnetophosphenes			PNS		
	X	Y	Z	X	Y	Z
Head	13.3%	33.3%	0.0%	13.3%	66.7%	20.0%
Heart	80.0%	60.0%	86.7%	20.0%	66.7%	13.3%
Prostate	0.0%	0.0%	6.7%	26.7%	53.3%	20.0%

The participants reported PNS across a wide range of locations in the body: in the shoulders, lower back, neck, jaw and below the ears, chest, abdomen, arms, fingers, legs and feet. There was no consistent spatial pattern of PNS occurrences. Scarcely, the intensity of the PNS effect was reported to increase with the gradient amplitude of the applied impulse (at a constant ramp time).

4.3.3 Reports of other physiological effects

The post-scan questionnaire responses are reported in Figure 4.4. Overall, 13.3% of the participants reported some level of discomfort during the experiment. This discomfort was associated with muscle twitches (13.3%), claustrophobia (6.7%) or scanner noise (13.3%). In all cases these were classified by participants as either a 'very slight discomfort' or a 'slight discomfort'.

The most commonly reported effects were changes in vision by 73.3% of the participants, and muscle twitches, which were reported by 60% (although primarily classified as an 'awareness of the effect', rather than discomfort). Other effects reported by participants were changes in smell or taste, dizziness, elevated heart rate (participant's subjective sensation, not evidence from pulse-oximeter measurements) and changes in temperature. In each case, these were reported as an 'awareness'

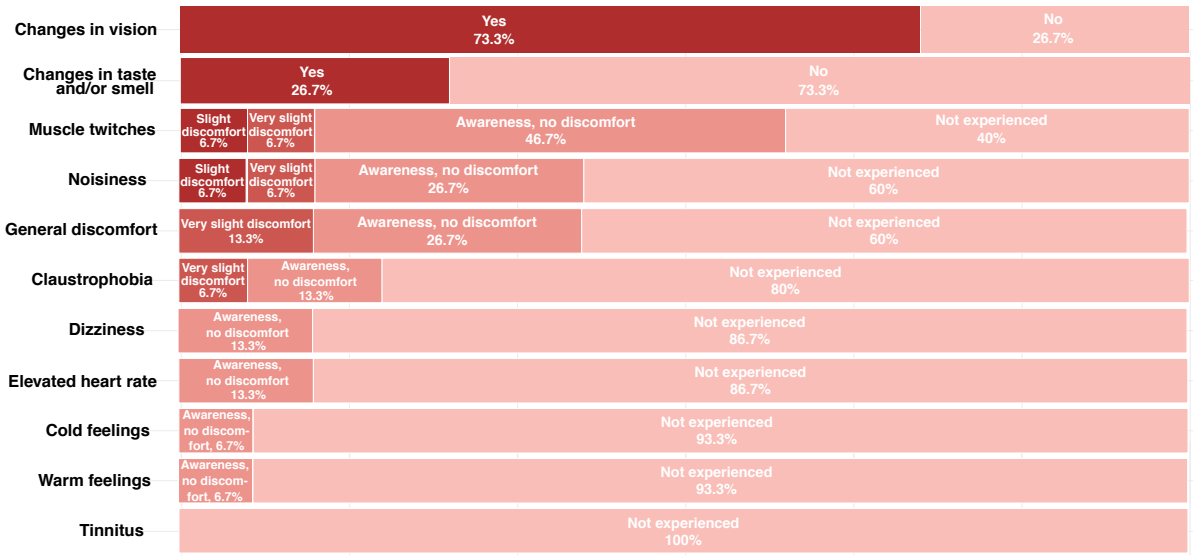

Figure 4.4: The post scan questionnaire results presenting the frequency of other physiological effects experienced during the scan.

rather than 'discomfort'. These effects were already reported in the literature, and are most likely not related to gradient switching [Kangarlu et al., 2004].

4.4 Discussion

We established the magnetophosphene stimulation probability in three anatomical locations, for a trapezoidal train of gradient pulses up to 300 mT/m. The experiment was implemented within limits imposed by regulatory bodies on PNS and cardiac stimulation.

4.4.1 Magnetophosphenes

While there have been several reports of magnetophosphenes associated with MRI, most are associated with the movement of an individual within the main (static) B_0 field [Friebe et al., 2015, Schenck, 1992]. To our knowledge, only two previous studies have reported the observation of phosphenes in participants arising from gradient switching, one in a similar system [Setsompop et al., 2013] and the other from a dedicated head only gradient coil [McCurdy et al., 2020]. There is renewed interest in application-specific gradient coils, for example, for neuroimaging applications [Tan et al., 2020]. These gradient coils offer the performance advantages of higher slew-rates and greater gradient strength, while their reduced gradient fringe-fields offer improvements in PNS performance when compared with whole-body gradient coils.

Electrophysiological studies have demonstrated that the magnetic field threshold for producing magnetophosphenes depends on the magnetic field switching rate, with the minimum threshold occurring at around 30 Hz [Lövsund et al., 1980]. The gradient switching frequencies used in this study are significantly higher, ranging between approximately 60 Hz and 300 Hz. However, the magnetophosphene occurrence reported in this work is consistent with earlier work, showing a reduction in the magnetophosphene threshold with a reduction in the switching frequency (i.e., longer ramp times). This effect was observed for all axes along which magnetophosphenes were observed.

At the location of the eyes, the estimated maximum absolute magnetic field due to the gradient coil alone, at maximum output (300 mT/m, Figure 4.1) is $\sim$ 20 mT, $\sim$ 50 mT and $\sim$ 20 mT for the head, heart and prostate landmarks, respectively. The magnetophosphenes reported by participants during the study (Figure 4.2) are consistent with these data - lower gradient amplitudes produce magnetophosphenes when the heart is at isocentre rather than when the head or prostate is at isocentre. As a comparison with existing literature, Lovsund [Lövsund et al., 1980] reported thresholds of $\sim$ 10 mT for a stimulus of 30 Hz and 14 mT at 45 Hz. In our results, magnetophosphenes were consistently observed for gradient amplitude 150 mT/m and ramp time 4.2 ms in the head position (X-gradient) equivalent to B_{max} of approximately 25 mT at $\sim$ 60 Hz.

No participants suffered discomfort due to the experience of magnetophosphenes, and they are not believed to be associated with any long-term health effects [International Commission on Non-Ionizing Radiation Protection et al., 2010]. Phosphene generation by magnetic, electrical and/or

mechanical stimulation of the retina and cortex are well known and generally reversible (non-harmful) phenomena [Brindley and Lewin, 1968, Grüsser and Hagner, 1990, Schwiedrzik, 2009]. For example, visual phosphenes are commonly experienced in brain stimulation techniques and these phosphenes have been attributed to a combination of cortical and retinal effects [Marg, 1991, Schutter and Hortensius, 2010, Webster and Ro, 2017].

Due to the variability in participants' physiological responses, participant positioning, gradient waveforms and MR hardware, it is challenging to condense these results into general guidance for the treatment of magnetophosphenes in MRI research. However, acknowledging a number of caveats, we evaluated the potential of magnetophosphenes for limiting the peak performance of an experiment by defining a 'magnetophosphene guideline value' which can be used to evaluate the probability of magnetophosphenes in a new experiment. For each condition (gradient axis and landmark), a 'guideline value' was defined, representing the maximum Gradient amplitude (G_{amp}), at the maximum slew rate, for which fewer than 10% of participants reported magnetophosphenes. These guideline values are shown in Figure 4.2, for each gradient axis and landmark, and e.g., for the Y-axis and heart landmark condition, the guideline value is defined by the point at 203 mT/m at a rise time of 2230 ms; resulting in a guideline value of 203 mT/m for studies acquiring data with high gradient strengths on the Y-axis with the participant positioned for cardiac imaging. Most importantly, in some situations, the gradient/rise time combinations which would be required to accurately define the threshold (moderate gradient strength $\sim$ 50-150 mT/m, but very long ramp times $>$ 2 ms) are not practically useful due to their inefficiency from a sequence design perspective. As a result, these points were not included in the study and thus, this guideline excludes any information on low gradient amplitude-long rise time combinations. The proposed guideline holds for the case where the gradient is being ramped near the maximum slew rate.

Studies exceeding the maximum G_{amp} should thus take additional measures before routinely scanning research participants. Such additional measures will depend on the institution's local rules but should include steps such as participant informed consent, Institutional Review Board approval, monitoring and/or limiting the duration of the exposure, pilot studies to evaluate stimulation in novel sequences/protocols/waveforms and additional monitoring of the participant during scanning (e.g., MR safe pulse oximeter or interaction via the intercom). Ideally, pilot studies should include the determination of probability maps, such as the ones determined in this work, to take advantage of the full potential of high-performance gradient systems. If the acquisition protocol includes only a few occurrences of those gradient settings producing magnetophosphenes, safety concerns may be limited. However, when the scans potentially causing magnetophosphenes are prolonged in time, the discomfort for the subject could become non-tolerable, possibly translating into drop-out and even a genuine safety risk (there are indications that longer magnetophosphene stimulus duration results in a longer time to recovery [Barlow et al., 1947]). Therefore the impact of magnetophosphenes on experimental design (e.g., visual fMRI) should not be neglected.

4.4.2 PNS

The reports of PNS presented here are also in line with previous findings [Ham et al., 1997, Schaefer et al., 2000], namely that the PNS probability is higher when pulsing the Y-gradient, most likely due to the larger anatomical cross-sectional area normal to the Y-axis. At ramp times longer than 1.5 ms, fewer reports of PNS were obtained (33.3% of participants across all imaging landmarks and gradient axes). A fraction of these PNS reports may have been sensations of gradient coil vibrations which are substantial at higher gradient amplitudes. When participants were uncertain, these observations were included as a report of PNS. Although the intensity of the PNS was reported to increase with higher amplitudes of the applied impulse, comparison to literature is not feasible; in previous works, protocols were stopped upon reaching the physiological threshold [Davids et al., 2019, Tan et al., 2020].

4.4.3 Other physiological effects

We questioned participants on any aspects of discomfort during the study to investigate any unexpected effects of high gradient field systems [Kangarlu et al., 2004]. The reported effects, such as elevated heart rate, dizziness or a sensation of warming during the scan, were consistent with reports from participants in studies on other systems in our centre. However, in our study, changes in vision (related to gradient switching, not static magnetic field) were more consistently reported, especially for high gradient amplitudes, as expected due to change of body position within the scanner bore.

4.4.4 Study limitations

The sampling of the gradient/ramp time points was limited by the scanner: the PNS limit (as implemented by the SAFE model [Hebrank et al., 2000]) and the IEC cardiac limiter [IEC 60601-2-33, 2015] (as implemented via a hardware limit on gradient output) were both enabled during the study. Additionally the set of gradient/ramp time measurement points was kept consistent for all gradient axes. This results in participants reporting less PNS for the X- and Z-gradients than for the Y-gradient. As a result, it was not possible to define a physiological threshold in all cases, e.g., the phosphene threshold usually exceeds the existing scanner's cardiac limit for ramp times shorter than 3 ms. This is due to a conservative interpretation of the IEC cardiac limit, based on Reilly extrapolations from animal studies [Reilly, 1990], which was set to an estimated probability of 10^{-9} to produce an ectopic beat (ISO/IEC-60601-2-33).

The magnetophosphene guidelines yield indicative values for when further investigation is required when planning a study involving a novel gradient waveform or pulse sequence. Further work will be conducted to investigate physiological effects in applications using alternative diffusion encodings such as multidimensional q-space imaging [Westin et al., 2016], and to evaluate the consistency of the magnetophosphene guidelines on the application of different waveforms. For generalized gradient encoding, as well as for newly-developed gradient systems [McCurdy et al., 2020, Versteeg et al., 2020], further work is required to predict the stimulation patterns precisely [Davids et al., 2019].

Comparisons with other studies using bipolar gradient schemes can be impaired by slight differences in the timing between the studies [Davids et al., 2019, Tan et al., 2020].

As our main interest was in the longer ramp time/stronger gradient domain, a limited data set was acquired in the gradient/ramp time combinations more commonly sampled during PNS studies (less than 100 mT/m and 1 ms). As a consequence, the conclusions that can be drawn relating to PNS are limited.

Finally, the participant group contained only males (due to the interest in the prostate). Thus the magnetophosphene and PNS probabilities may be different for females, adolescents or younger groups, as differences in anatomical distances will lead to participants experiencing different parts of the gradient field (Figure 4.1).

4.5 Conclusions

Evaluation of the physiological limits is critical for human safety on high-performance gradient MR systems. This study investigated the elicitation of magnetophosphenes by a high-gradient field system when different anatomical locations were placed at isocentre. Based on the framework provided by this work, the likelihood of magnetophosphenes can be estimated in future studies of different anatomical regions when using ultra-strong gradient whole-body MR systems.

Chapter 5

Feasibility of 300 mT/m gradients for probing tissue microstructure in prostate cancer

Contents

5.1 Introduction

Over several decades, dMRI has gained recognition in cancer detection and diagnosis [Guo et al., 2002, Yamasaki et al., 2005, Yoshikawa et al., 2008, Zelhof et al., 2009], and its role is extending into areas of staging, grading and treatment design.

The ADC (here apparent diffusion coefficient) [Le Bihan et al., 1986] - derived from data with low-to-moderate diffusion weightings - has been used in multiparametric mp-MRI as a sensitive surrogate for microstructural changes in cancer. However, several studies reported a lack of specificity and limited sensitivity of ADC, e.g., in tumour grading [Shaish et al., 2017]. Moreover, cancerous lesions with microscopic changes are not always visible on mp-MRI [Johnson et al., 2019, Lee et al., 2018, van Houdt et al., 2020] due to intra-tumour heterogeneity [Kweldam et al., 2019].

More comprehensive characterisation of tumours by applying stronger diffusion weightings (commonly quantified by the b-value) at multiple diffusion times and coupling the dMRI signal to a mathematical model or representation of tumour tissue include, e.g., VERDICT [Johnston et al., 2019, Panagiotaki et al., 2015]. In prostate cancer, a proxy for intracellular signal contributions derived from VERDICT has shown to result in improved classification of clinically significant PCa than the ADC [Singh et al., 2022]. For more comprehensive overview of methodological advances in prostate cancer please refer to Chapter 3, Section 3.4. However, strong diffusion weightings and exotic encodings on clinical scanners can significantly lengthen the TE thus decreasing the SNR per unit time. Moreover, short diffusion times and short echo times at higher diffusion weightings are off-limits on clinical systems due to the limited gradient power.

To ameliorate these issues, various ultra-strong whole-body [Kimmlingen, 2017, Setsompop et al., 2013] and head-only [Foo et al., 2020, Versteeg et al., 2021, Webb, 2016, Weiger et al., 2018] gradient systems have been designed. In short, strong gradients provide a shorter TE for a given b-value, and hence a higher SNR - i.e., reduced signal loss due to transversal relaxation - per unit b-value (please see Figure 5.1 and also Chapter 2, Section 2.7). These technological advancements have greatly facilitated the characterisation of human tissue microstructure, albeit currently only in the brain [Jones et al., 2018, McNab et al., 2013, Nilsson et al., 2017, Palombo et al., 2020a, Tax et al., 2020]. Nevertheless, the advantages of strong gradients outlined above represent new opportunities for dMRI with enhanced diffusion resolution for clinical use-cases, and among many applications, they hold promise for advancing the early detection of cancerous lesions, e.g., in the brain and the prostate.

This work assesses the feasibility of prostate dMRI with ultra-strong gradients in healthy population and patients with PCa and compares the image quality to more commonly-available gradient strengths. Using advanced gradients, the signal decays can be examined over a much larger range of b-values at shorter diffusion times and TEs off-limits on clinical scanners. Therefore, the hypothesis of this work is that strong gradients enhance the contrast of tumour lesions compared to healthy tissue at high b-value data. In addition, achievable shorter TEs unlock possibility of evaluation of the SNR gains for fitting a representation using higher b-values such as DKI.

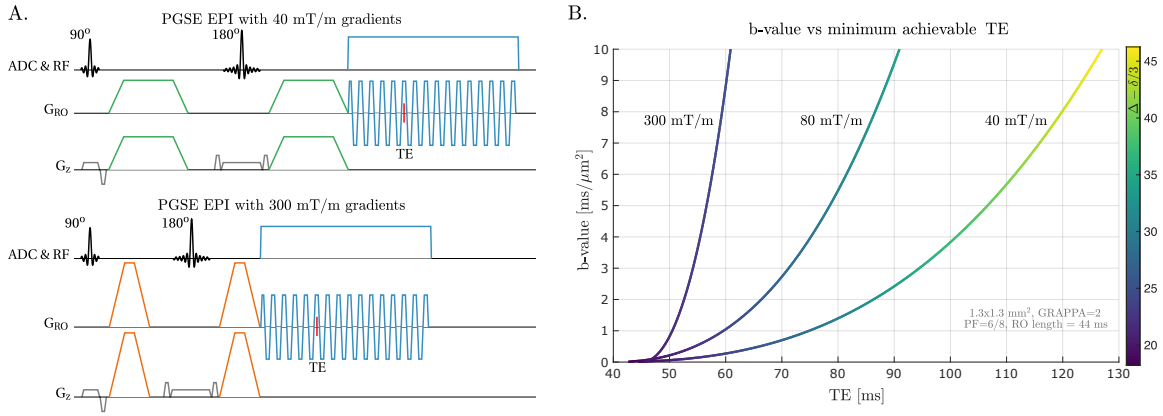

Figure 5.1: **A.** Diffusion sequence diagrams of single-shot EPI readout with Stejskal-Tanner diffusion encoding and gradient capabilities of clinical (*top*) and ultra-strong gradients (*bottom*) MRI systems. ADC (here analog to digital converter) & RF: Spectral fat saturation, excitation and refocusing pulses (*in black*), and ADC (*in blue*). G: Slice selective and refocusing gradients with spoilers (*in light grey*), diffusion gradients (*in green and orange*), EPI RO (*in blue*). **B.** Simulation of b-value vs minimum achievable TE for EPI readout and different maximum gradient amplitudes of 300 mT/m, 80 mT/m and 40 mT/m, using a PGSE sequence with readout parameters provided in the plot. For each point, the colour coding gives the achieved diffusion time ($\Delta - \delta/3$ [ms]). The chosen b-value range for simulation is beyond the upper limit of interest for application in prostate cancer MRI; however, high b-values between 2-5 ms/μm^2 can be advantageous to characterise restrictions [Johnston et al., 2019, Panagiotaki et al., 2015, Tang and Zhou, 2019].

5.2 Methods

5.2.1 Study participants

Ethical approvals for the study were obtained from the School of Psychology Research Ethics Committee (REC) of Cardiff University and from the REC of the National Health Service (NHS), Wales (Health Research Approval, HRA, and Health and Care Research Wales, HCRW) (CVUHB ref 21/OCT/8264).

Four healthy men (age range: 46-64 years, M = 54.8, SD = 7.9, weight range: 75-104 kg, M = 85.6 kg, SD = 12.7 kg, height range: 1.68-1.81 m, M = 1.76 m, SD = 0.06 m; M - mean, SD - standard deviation) and six patients on Active Surveillance (age range: 67-74 years, M = 70.2, SD = 2.9, weight range: 75.3-100 kg, M = 85.5 kg, SD = 9.2 kg, height range: 1.72-1.81 m, M = 1.76 m, SD = 0.04 m) with the PZ prostate cancer confirmed by MRI and TRUS guided biopsy were included in the study, after providing written consent to participate. Detailed patient cohort information is provided in Table 5.1. We advised our participants to follow a diet for 24 hours prior to imaging to reduce the risks of artefacts in the data.

5.2.2 Data acquisition

Imaging data were acquired on a Connectom research-only MRI scanner, a modified 3T MAGNETOM Skyra system equipped with a 300 mT/m gradient coil (Siemens Healthcare, Erlangen, Germany) using Spine32 and Body18 coils (Siemens Healthcare, Erlangen, Germany).

Structural MRI data were acquired using a 3D T2-weighted turbo spin echo (TSE) sequence with parameters: FOV read = 230×230 mm, matrix size = 230×230, isotropic voxel = 1 mm^3, TR = 1920 ms, TE = 102 ms, varying flip angle (due to different SAR limitations across subjects), phase encoding (PE) direction = right-left. The total acquisition time of structural data was 10 min.

Diffusion-weighted images were acquired using a PGSE EPI sequence [Stejskal and Tanner, 1965], with anterior-posterior PE direction. Six shells of 15 non-collinear directions distributed on a sphere at b = [0, 0.05, 0.5, 1, 2, 3] ms/μm^2 were sampled, where non-diffusion-weighted, i.e. b = 0 ms/μm^2 images were interspersed throughout the sampling scheme. The order of acquisition was randomised to limit the thermal load of the scanner. Three non-diffusion weighted images with posterior-anterior PE direction were acquired for the assessment and correction of susceptibility-induced geometrical distortions.

dMRI datasets were acquired with gradient strengths reflecting high-performance (G_{max} = 300 mT/m, at SR = 110 T/m/s) and clinical systems (G_{max} = 40 or 80 mT/m, at SR = 200 T/m/s). The minimum achievable TE, δ and Δ, were as follows (TE/δ/Δ [ms]): (P1, where P stands for protocol) 54/5/25, (P2) 70/16/32, and (P3) 95/26/48, for a maximum achievable gradient strength of 300, 80, 40 mT/m, respectively. TR was constant across protocols and set to 3.5 s, to harmonise longitudinal relaxation effects [Baur et al., 2020]. The in-plane resolution was 1.3×1.3 mm^2, FOV = 220 mm×220 mm, matrix size = 168×168, slice thickness = 5 mm, slices = 14, GRAPPA = 2, simultaneous multislice = 2, and partial Fourier = 6/8, bandwidth of 1860 Hz/pixel. The total acquisition time of dMRI data was 20 min.

In addition, for two patients we designed a set of three protocols (P4-P6) with increased maximum b-value (additional b-values were b = [3.5, 4, 4.5, 5] ms/μm^2) to further investigate the signal decay from restricted diffusion in lesions. The achievable TE/δ/Δ ([ms]) were as follows: (P4) 56/6/26, (P5) 79/20/35, and (P6) 106/34/50, for maximum achievable gradient strength of 300,

Table 5.1: Clinical cohort data overview. (PT - patient, PNI - perineural invasion, EPE - extraprostatic extension, year of clinical examination - mp-MRI and TRUS biopsy). The clinical information (apart from age) is dated as per year reported in the 3rd column.

ID	Age	Year of clinical exam	PSA [ng/ml]	PIRADS	Tumour location	Tumour size	Histology	Gleason score
PT 1	74	2021	5.2	4+3	right posterolateral PZ at the apex, left anterior PZ at the apex	4 mm, 3 mm	Prostatic adenocarcinoma (no PNI or EPE)	3+3
PT 2	68	2021	6	3	right posteriolateral PZ at the base	7 mm	Prostatic adenocarcinoma	3+3
PT 3	72	2022	12.8	5+3	left posterior and lateral PZ, right posteriorlateral PZ	20 mm, 9 mm	Prostatic adenocarcinoma	3+4
PT 4	67	2019	4.7	4	left PZ at the base and midgland	13 mm	Prostatic adenocarcinoma (no PNI or EPE)	3+4
PT 5	68	2020	4.3	3	left lateral PZ, right lateral PZ at midgland level	4 mm, 5 mm	Prostatic adenocarcinoma (no PNI or EPE)	3+4
PT 6	72	2021	6	no record	left PZ at the base and midgland	no record	Prostatic adenocarcinoma (no PNI or EPE)	3+3

80, 40 mT/m, respectively, with remaining parameters as above. The total acquisition time of these additional dMRI protocols was 28 min.

Images were reconstructed using 'adaptive combine' with optimal phase shift factor = 4 [Setsompop et al., 2012]. Data filtering methods implemented by the vendor, apart from 'prescan normalize', were switched off.

5.2.3 Quality assessment and data preprocessing

The unprocessed dMRI data were checked for signal intensity errors [Sairanen et al., 2018], and the noise standard deviation was estimated on low b-value magnitude data (up to 1.5 ms/μm^2) [Cordero-Grande et al., 2019]. SNR was subsequently computed for protocols P1-P3 as $\frac{\widetilde{S}_{ROI}}{\widetilde{\sigma}_{ROI}}$, where $\widetilde{S}_{ROI}$ is the median signal over all voxels across repetitions for each of the b-value and within a mid-gland slice mask (delineated on the average b = 0 ms/μm^2), and $\widetilde{\sigma}_{ROI}$ is the median of the estimated noise standard deviation of the noise map within the same mask. To avoid overestimation of the SNR, SNR was calculated based on unprocessed data. The effect of protocol choice on SNR was evaluated using a linear mixed effects model, including both subject and b-value as random effects. This test was followed by a second linear mixed effect model, evaluating the effect of protocol within each b-value (correcting for multiple comparisons across b-values using the Bonferroni method). Final pairwise comparisons were performed using the Wilcoxon test for non-parametric paired values, with correction for multiple comparisons using the Bonferroni method.

Data were subsequently denoised [Cordero-Grande et al., 2019], and corrected for Gibbs ringing accounting for partial Fourier acquisition [Lee et al., 2021a], B_0 field inhomogeneity distortions [Andersson et al., 2003], and gradient nonlinearity (GNL) distortions [Jovicich et al., 2006], and spatio-temporal corrections of b-matrices were computed [Bammer et al., 2003, Rudrapatna et al., 2021]. The results of each step were inspected manually and a 'minimal' preprocessing pipeline was adopted; neither eddy currents nor motion correction was applied.

5.2.4 Data analysis

For qualitative analysis, direction-averaged signals were calculated [Callaghan et al., 1979]. For the comparison of quantitative measures, maps of MD, FA, MK, AK and RK were derived from the weighted linear least squares estimation of the DKI representation [Veraart et al., 2013] on each non-averaged dataset (up to b = 2 ms/μm^2) and accounting for b-matrix deviations.

5.2.4.1 Simulations

Signals were simulated for benign and cancerous tissue based on a three pool model [Zhang et al., 2020] composed of stroma, epithelium and lumen with different T_2 and diffusivities. For simulations, we used SNR = 25 and SNR = 30 for healthy and cancerous tissue, respectively. The SNR was calculated at b = 0 ms/μm^2 at TE = 0 ms as $\mathrm{SNR}_{b=0,TE\neq 0} = \mathrm{SNR}_{b=0,TE=0} \cdot \exp(-\frac{TE}{T_2})$ using the SNR estimates from in vivo data and average T_2 values of prostate tissue [Lee, 2019]. We performed 15 Rician noise realisations per b-value to reflect number of different gradient directions

in our protocols. To enable direct comparisons with in vivo data, we multiplied the simulated normalised signals by the estimated S_0 signal at b = 0 ms/μm^2 and TE = 0 ms using experimental S_0 values at b = 0 ms/μm^2 measured at different TEs ('benign case' - healthy control 1, 'cancerous case' - patient 4).

5.2.4.2 Image distortion and contrast evaluation

The images acquired with P1-P3 were evaluated by a radiologist with 5 years of experience in reporting prostate MRI to investigate whether the acquired high b-value images with strong gradients improve the conspicuity and delineation of lesions. Thus, we included only data from clinical cohort in this experiment. The following images were presented simultaneously in agreement with clinical practice: the T2-weighted image and a set of dMRI images acquired with either P1, P2, or P3, including the average b = 0 ms/μm^2 image, the average high b-value image at any of b-values = [0.5, 1.5, 2] ms/μm^2, and the estimated MD map. As a result, for all the patients scanned with P1-P3 we obtained 45 combinations (5 subjects x 3 protocols x 3 high b-value images). The order of combinations was randomised within each subject. Each dMRI set (i.e., combination of b = 0 ms/μm^2 and high b-value at the TE corresponding to the maximum gradient strength) was evaluated establishing the diagnostic quality (being able to rule in or out clinically significant PCa) of the prostate MRI scans (1 - all sequences are below the minimum standard of diagnostic quality, 3 - the scan is of sufficient diagnostic quality, 5 - all images are of optimal diagnostic quality). For the purpose of our study, we tailored the proposed PI-QUAL system [Giganti et al., 2020, 2021] to fit our case study needs. Importantly, the radiologist was not informed on the GS but aware that the included patients were on Active Surveillance.

In addition, each set of images was assessed subjectively using 5-point Likert image quality scale w.r.t. distortions and zonal anatomy. The "distortion" was defined as the presence of artefacts, e.g., signal pile-ups, signal drop-out, warping, ghosting, and blurring. It was assessed on a 5-point scale (1 = severe; 2 = significant; 3 = moderate; 4 = low; and 5 = no influence). The "zonal anatomy" was defined as the ability to distinguish the prostate gland zones (transitional and peripheral) and was assessed on a 5-point scale (1 = poor; 2 = below average; 3 = average; 4 = above average; and 5 = excellent).

Finally, the dMRI data collected with 3 protocols were presented to the radiologist side-by-side with the question to select the preferred dMRI acquisition per patient.

5.2.4.3 ROI analysis

ROIs were manually outlined on the dMRI (either 1.5 or 2 ms/μm^2) after confirmation of lesion location by a radiologist. Two different types of ROIs were defined. The first type covered the tumour lesions with up to three ROIs per lesion. In total, ten ROIs in lesions were delineated using a high b-value image from the preferred by the radiologist protocol (either P1 or P4), all in the PZ. The second type of ROI covered normal-appearing PZ regions, e.g., contralateral side of the PZ (with no tumour at the corresponding location in histology in the clinical group). Up to three ROIs

per subject were defined in healthy regions, total of nine ROIs. From each ROI, values of signals at high b-values (b = 0.5-3 ms/μm^2) were extracted. Two sets of data were defined: normal-appearing prostate tissue and cancerous tissue (patients with GS 3+3 and 3+4 pulled together). Extracted values were averaged over ROI and within-subject normalised difference between mean signal across lesions and healthy tissue was calculated to represent each subject in group analysis. A normalisation factor was defined as the mean of the signal in ROI placed in the bladder extracted from P1 protocol data.

The data were compared statistically following the steps described in Section 5.2.3 to assess whether there is a main effect of protocol across b-values and to test which protocols give statistically significant signal differences within each b-value.

5.3 Results

5.3.1 Quality assessment and preprocessing

The results overall showed feasibility of dMRI with ultra-strong gradients in healthy controls and patients. Slicewise outlier profiles revealed only few signal dropouts (Figure 5.2). Looping through the interleaved b = 0 ms/μm^2 images, subtle image misalignments were observed in protocols with the highest gradient strength (P1 and P4), presumably due to short- and long-term eddy currents and/or frequency drift (Figure 5.3). Additionally, for the volumes acquired with non-zero diffusion weighting and sufficient tissue contrast (e.g. b $<$ 1.5 ms/μm^2), minor misalignment to the first b = 0 ms/μm^2 volume image could be observed due to EC; for higher b-values, visual assessment of artefacts in individual images was challenging to evaluate.

Figure 5.4 shows the results of preprocessing in three datasets from patients, each differently affected by distortions. After correction for distortions resulting from susceptibility differences and

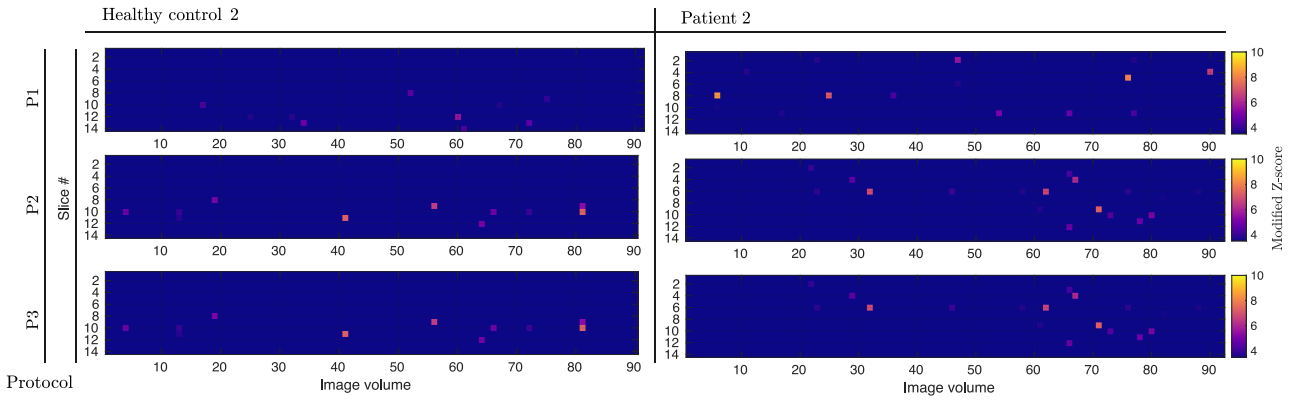

Figure 5.2: Results of outlier rejection performed with SOLID [Sairanen et al., 2018] for two worst case scenarios subjects (one healthy control and one patient). Modified Z-score is a robust version of the Z-score and assesses whether an observation is far away from the median value of the signal across all dMRI measurements with a similar b-value. In our processing analysis, the values below 3.5 have weight 1, the values above 10 have weight 0, and the values between 3.5-10 are linearly transformed to weights on 1-0 range.

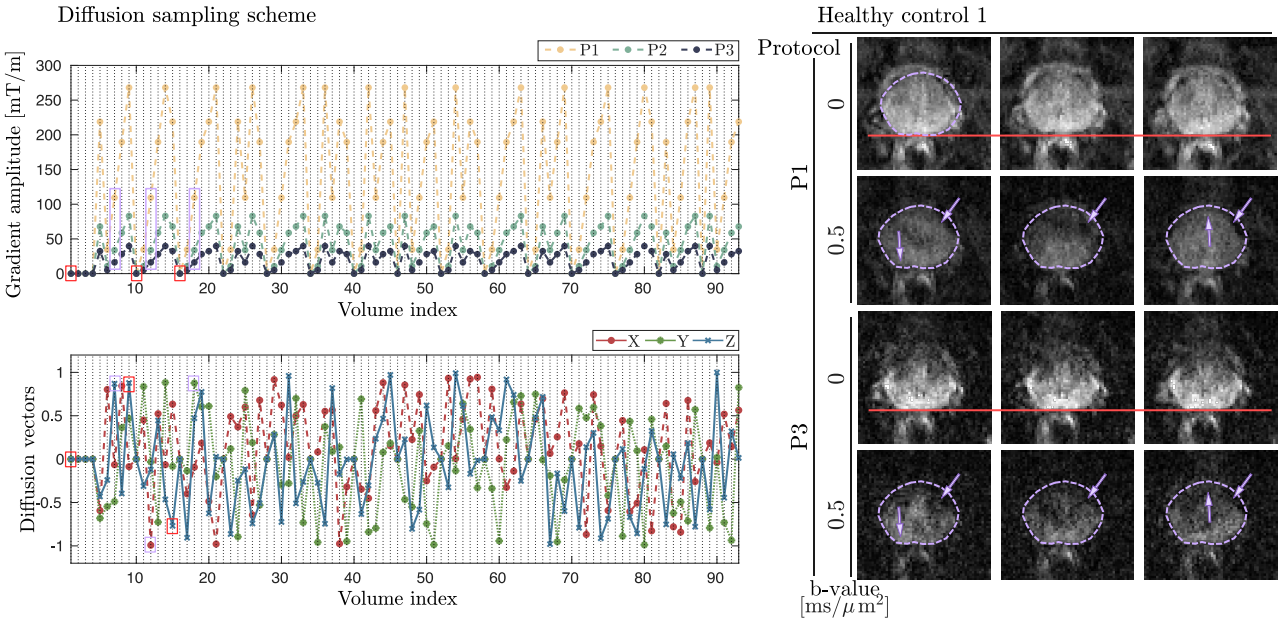

Figure 5.3: Diffusion sampling scheme (*left*): The total gradient amplitude applied (*top panel*) for each volume acquisition in the sampling scheme (P1-P3 protocols). Diffusion vectors (*bottom panel*). Eddy current effects presented used a single healthy control dataset (*right*). The image shift from EC (caused by B_0 or slice direction EC) is shown on b = 0 ms/μm^2 and b = 0.5 ms/μm^2 (1st column). In addition, the read EC and phase EC (causing shearing - 2nd column, and stretching - 3rd column) are shown using b = 0.5 ms/μm^2 single shot images.

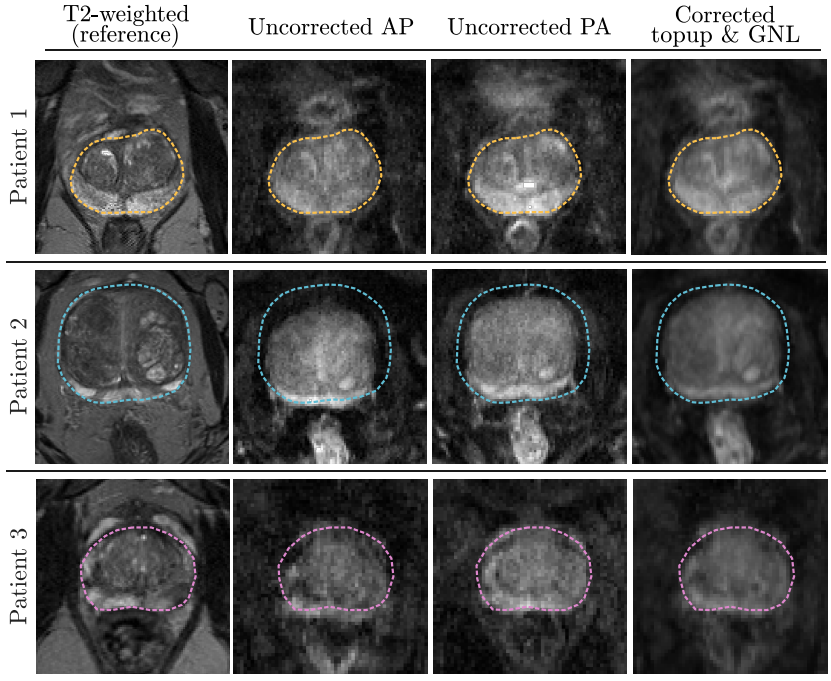

Figure 5.4: Visualisation of the distortion correction processing steps applied to the acquired data: Patient 1 - ideally positioned at isocentre, Patient 2 - positioned offcentre, Patient 3 - positioned at isocentre, with perceptually more severe distortions. The reference T2-weighted images with prostate gland delineation (*dashed lines*) are shown, alongside with AP and PA phase encoded b = 0 ms/μm^2 image from dMRI EPI scans. The result of the applied corrections is shown in the last column.

GNL, the correspondence with the T2-weighted scan was generally improved with most of the signal pileups corrected (Patient 1-3) and therefore signals spatial location recovered. In addition, in Patient 2 with benign prostatic hyperplasia (BPH) which leads to an enlarged gland, GNL associated with ultra-strong gradients systems caused visible geometric distortions at the edges of the image and minor deformations within the prostate gland (Patient 2).

Figure 5.5A. highlights the gain in SNR from shortening the TE by using higher gradient strength, especially within the prostate gland at higher b-values. The estimated median values (with interquartile range, IQR) of SNR based on the data from all subjects from P1-P3 qualitatively show notable SNR increases for the P1 protocol for each b-value. Although our sample size was small, statistical comparisons between the three protocols using a linear mixed effects model, followed by pairwise comparisons of protocols within each b-value, revealed statistically significant differences, crucially for the highest b-value (b = 3 ms/μm^2) used in the acquisitions.

For participants accurately positioned with the prostate gland at the scanner isocentre, the estimated effective b-values inside the prostate deviated from the imposed ones by maximally 5% (mostly 0-3%). Nevertheless, careful positioning is crucial as a significant shift of +/- 80-100 mm along the Z-axis can cause on average 10% and up to 25% deviation (Figure 5.5B, Patient 2 and Healthy control 1).

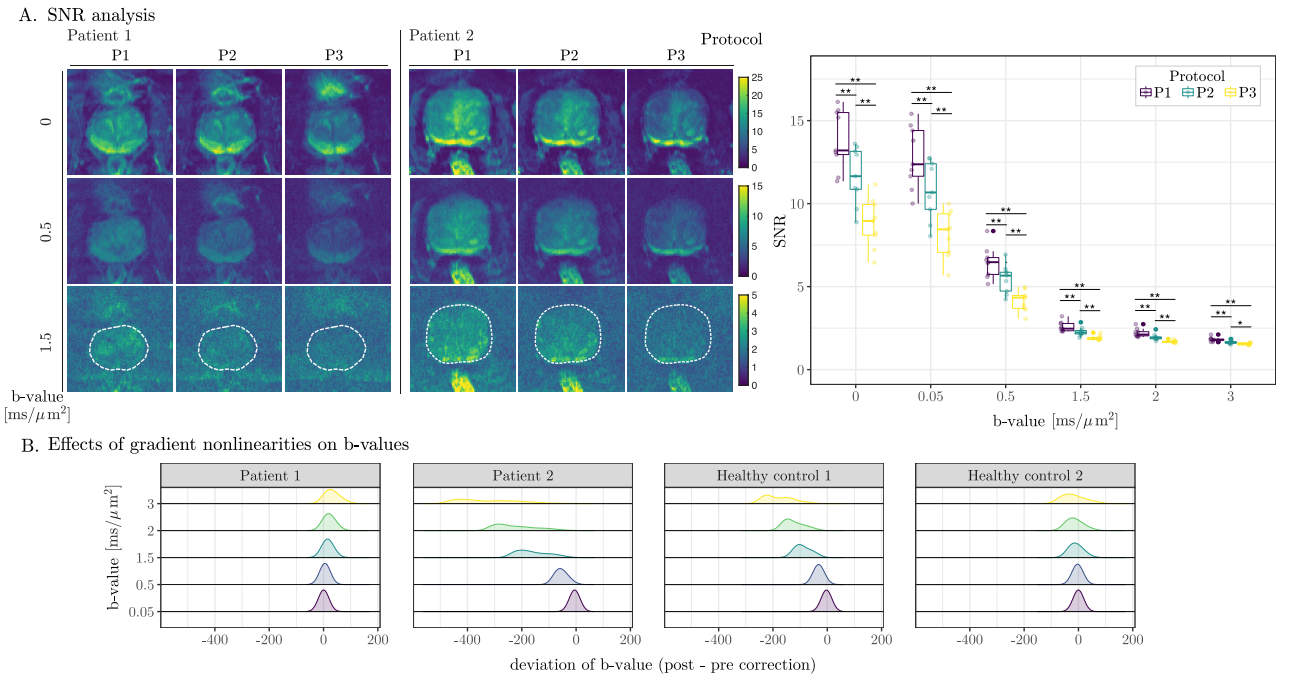

Figure 5.5: A. SNR analysis. (*left*) Spatial distributions of SNR values for two representative patients and three selected diffusion weighted volumes. Note the different color scales. (*right*) The shell-wise SNR across all acquired b-values. Dots represent SNR estimate at subject level, and the box plot represents the median and interquartile range of SNR per given protocol at a group level (* - p $<$ 0.05, ** - p $<$ 0.01). B. Distribution plots of the b-value deviations caused by gradient nonlinearities for all b-values in data from four selected subjects (Patient 1 - positioned at isocentre, Patient 2 - positioned offcentre by approx. 8 cm, Healthy control 1 - positioned offcentre by approx. -10 cm, Healthy control 2 - positioned at isocentre).

5.3.2 Simulations

The benefits of ultra-strong gradients in the context of imaging distinct microstructural compartments of prostate tissue are shown in Figure 5.6. Reducing the TE at a given b-value significantly increases the signal contribution from the supportive stromal compartment (short T_2-pool of approximately 30 ms with intermediate diffusivity of 1-2 ms/μm^2) as well as the epithelium. For changes associated with cancerous tissue in which diffusion becomes more restricted, higher b-values contain significant information above the noise floor. The simulations resemble the signal decays obtained from in vivo data (see the following sections and Figure 5.7 and 5.8).

5.3.3 Healthy controls

Figure 5.7 (*top*) shows the direction-averaged dMRI images as a function of b-value for two healthy controls. The signal intensity in most of the prostate tissue decays substantially at b-value $>$ 1.5 ms/μm^2 acquired at the longest TE (P3), whereas for the protocols at shorter TE (specifically G_{max} @ 300 mT/m, P1), there is significant residual signal present, well above noise floor, at the highest acquired b-value (3 ms/μm^2). This also becomes apparent in the signal decay curves (*bottom*) from the manually delineated ROIs (within the PZ), with an estimate of the noise floor.

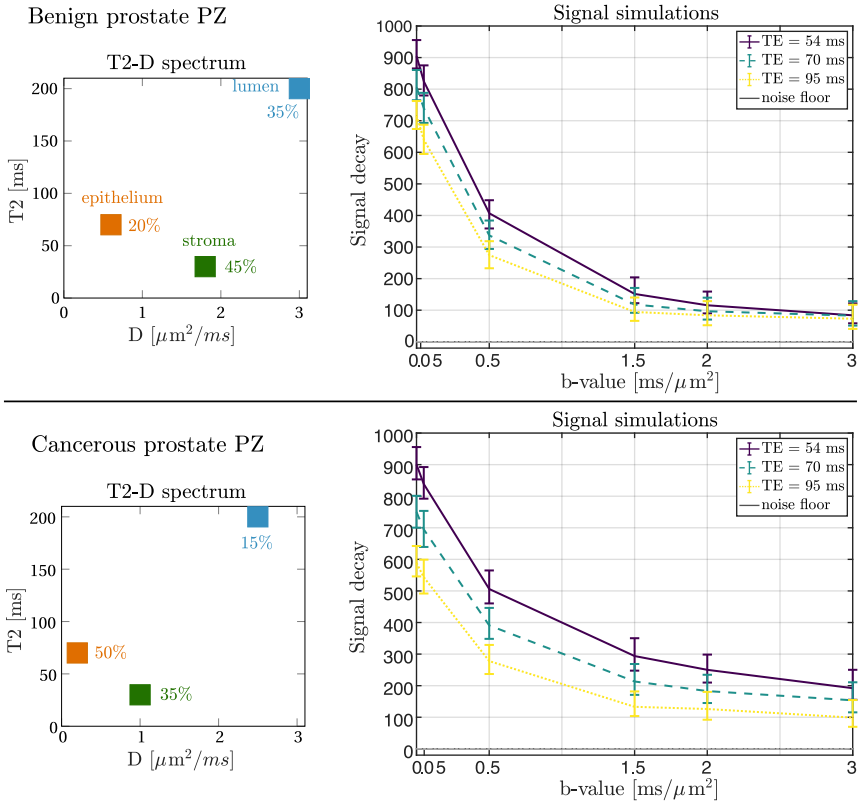

Figure 5.6: (*left*) Diagram of prostate $T_2 - D$ spectrum in benign tissue and malignant adenocarcinoma (GS 3+4). (*right*) Simulation of the three pool model (median with interquartile range) per the values in [Zhang et al., 2020] with diffusivities multiplied by a factor of 2 to reflect in vivo tissue. Ex vivo estimates of T_2 values were used. The expected volume fractions of three microenvironments present in the prostate as given on $T_2 - D$ diagrams. Further simulation details in the main text.

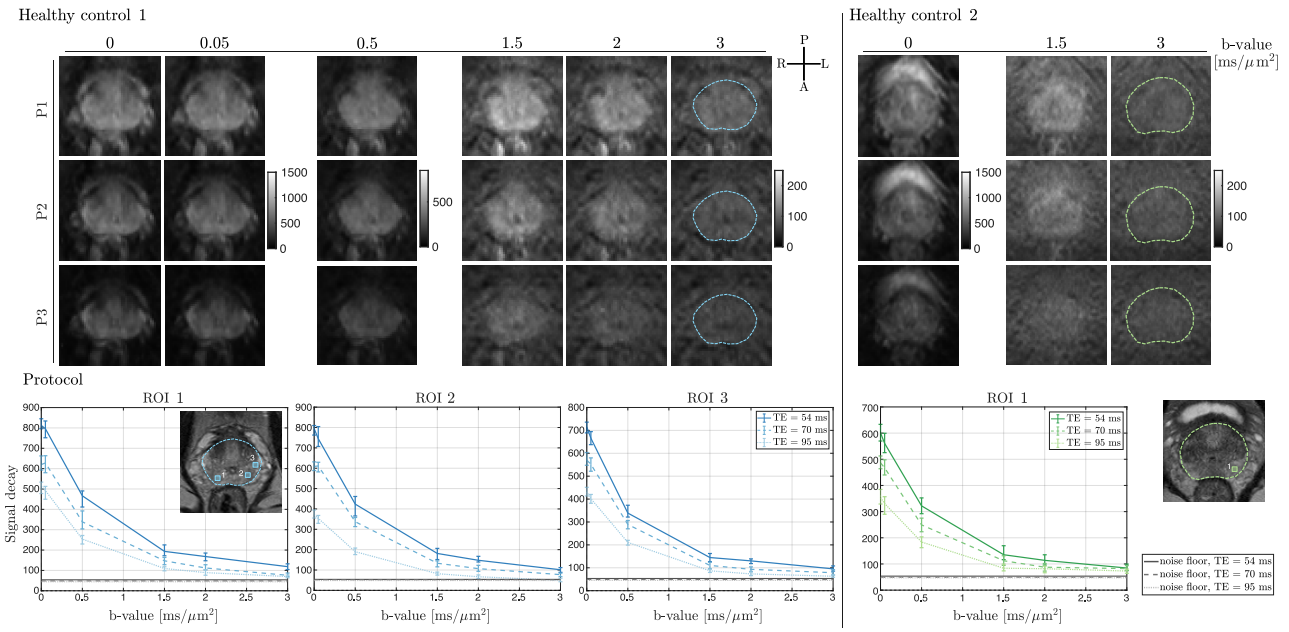

Figure 5.7: Representative example of a healthy control dataset. The direction-averaged diffusion signals of selected b-shell data: 300 mT/m (P1), 80 mT/m (P2) and 40 mT/m (P3) systems (*from top to bottom*) are presented for two healthy controls. Based on the T2-weighted image (an example shown in *bottom left*), a prostate mask was drawn and overlaid on high b-value diffusion dataset. Signal decays (median with interquartile range) of the direction-averaged signals from ROIs drawn in the prostate gland are shown. The gray lines represent the mean of the estimated noise floor in each ROI [Cordero-Grande et al., 2019], and, in most cases, the lines from each ROI visually overlap.

Results from other healthy controls are presented in the Appendices (Figure A.1).

5.3.4 Prostate cancer patients

For the clinical cohort (Figure 5.8 *top*), we observe substantial improvement of lesion-to-healthy tissue contrast for the protocol at high b-values and short TE (P1). One can readily appreciate the increased signal in ROIs at b = 3 ms/μm^2 across patients with different Gleason scores (Figure 5.8). Furthermore, Figure 5.8 (*bottom*) presents the benefit of increasing the b-value up to 5 ms/μm^2 (protocols P4-P6): while the signals from the datasets acquired with clinical gradient strength (80 mT/m - P5, and 40 mT/m - P6) approach the noise floor at intermediate b-values (1-3 ms/μm^2), the decay curve at 300 mT/m shows residual signal at the highest b-values (4.5-5 ms/μm^2). Results from other patients are presented in the Appendices (Figure A.2).

Normalised signal differences from the patient cohort scanned with P1-P3 protocols across high b-values are shown in Figure 5.9. The estimated group-level median values with IQR of signal change show increases within each b-value for the P1 the protocol. The main effect of protocol on signal differences between tissue types (cancerous lesions vs. healthy regions) was evaluated using linear mixed effects modelling, with subject and b-value included as random effects. This test confirmed the presence of a statistically significant effect of protocol, including the evaluation of the effect within each of the b-values. However, pairwise comparisons yielded no statistically significant results,

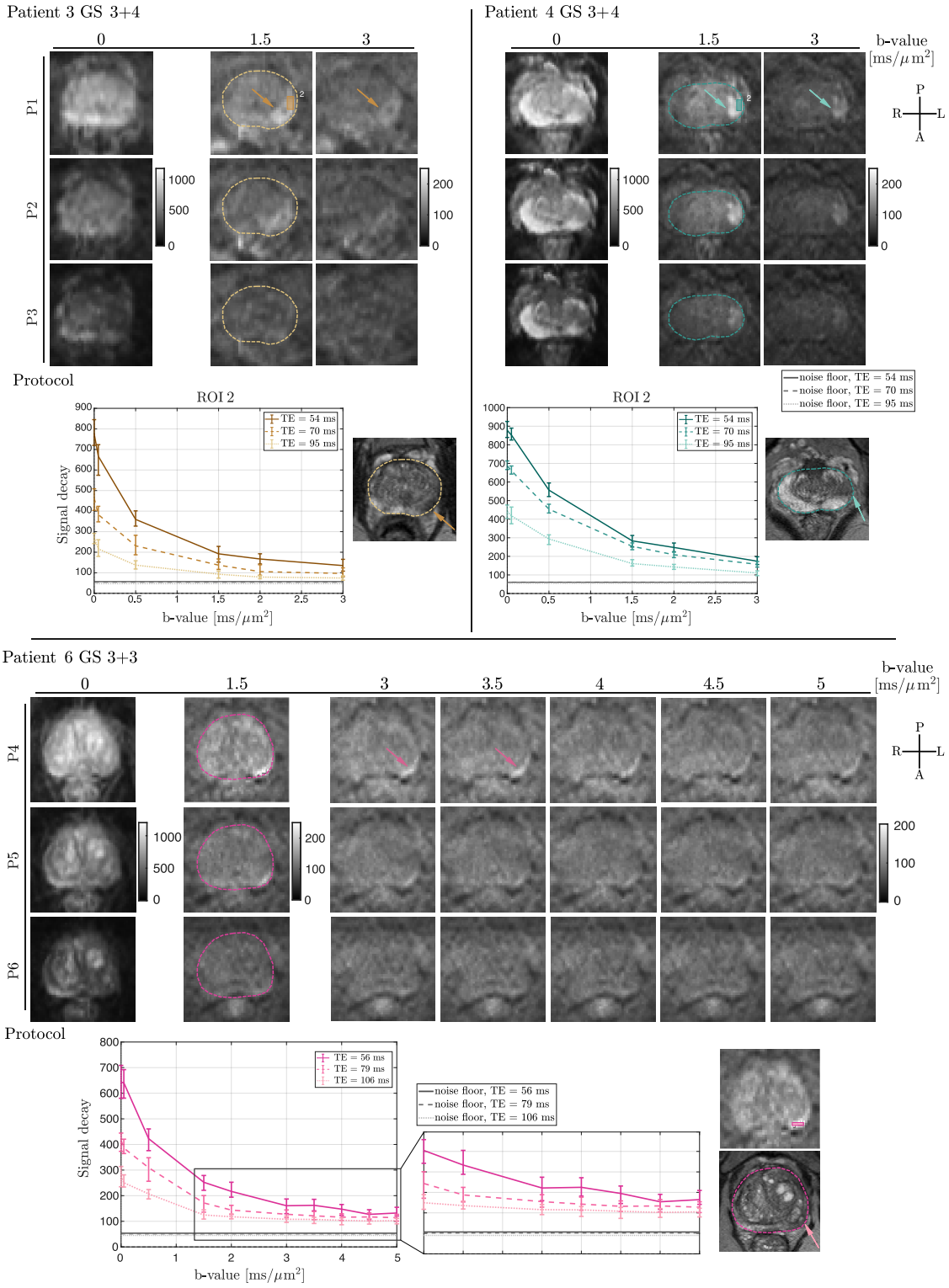

Figure 5.8: Representative example of patient datasets (P1-P3 protocols - *top*, P4-P6 protocols with ultra-high b-value - *bottom*). The direction-averaged diffusion signals of selected b-shell data are presented for three patients. As in the case of healthy controls, a prostate mask was drawn on T2-weighted image and overlaid on high b-value (1.5 ms/μm^2) diffusion dataset (contrast which is obtain in the clinics through signal extrapolation). Signal decays (median with interquartile range) of the direction-averaged signals from ROIs (boxes) drawn in the cancerous lesions (depicted by arrows) are shown. The gray lines represent the mean of the estimated noise floor in each ROI [Cordero-Grande et al., 2019], and, in most cases, the lines from each ROI visually overlap.

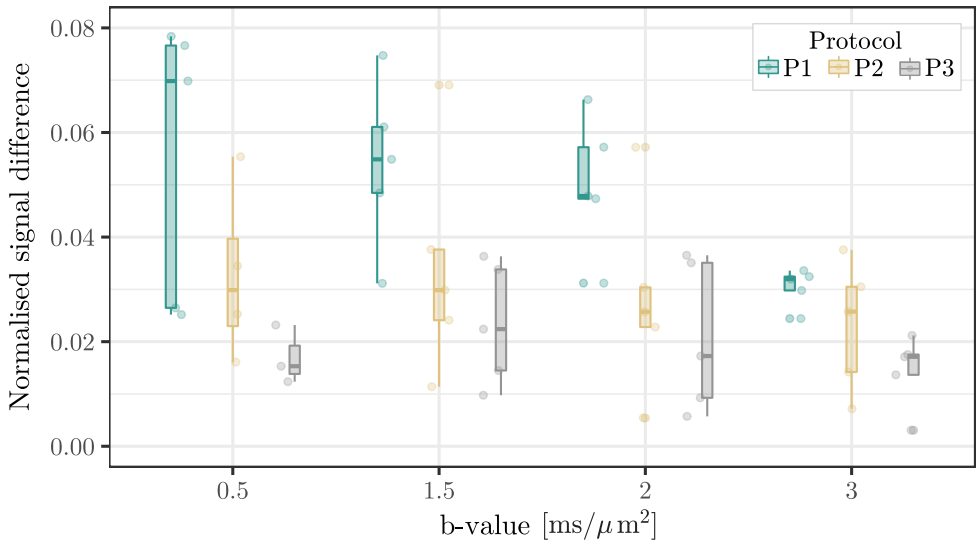

Figure 5.9: Boxplots of signal differences across ROI lesions and healthy tissue across patients scanned with P1-P3 protocols for 4 selected high b-values. The signal difference was normalised by signal at b = 0 ms/μm^2 in a ROI drawn in the bladder. Dots represent normalised signal difference at subject level, and the box plot represents the median and interquartile range per given protocol at a group level.

most likely due to the small number of subjects (low statistical power) included in this pilot study.

5.3.5 Prostate MRI diagnostic quality evaluation

A summary of selected image quality scores for different protocols combinations is given in Figure 5.10. All dMRI data were classified as of diagnostic quality with the highest average scores for dMRI data combinations with b-values of 0 and 0.5 ms/μm^2 included (P1 - 3.6±0.55, P2 - 3.8±0.45, P3 - 3.6±0.89). For the combinations with higher b-values (1.5 and 2 ms/μm^2), P1 and P2 protocols were scored to be equally good or better than P3. The acquired high b-value image in P1 protocol at 0.5 ms/μm^2 was always scored to be of diagnostic quality whereas for P2-P3 these scores were lower. For the remaining combinations with high b-values (1.5 and 2 ms/μm^2) there was no clear preference of the scan from different protocols. The 'zonal anatomy' demarcation of dMRI data, combinations with b-values of 0 and 0.5 ms/μm^2 were scored above average across P1-P3 protocols (3.2±0.45 for all protocols), reaching scores close to below average for remaining combinations. The 'distortions' were the most prominent in combinations with dMRI data from P3 protocol (3.4±0.89, 2.6±0.55, 1.6±0.55, respectively for 0 and 0.5 ms/μm^2, 0 and 1.5 ms/μm^2, 0 and 2 ms/μm^2). Similar extent of distortions was reported for combinations of dMRI data from P1-P2 protocols, with P1 scored higher for combinations including higher b-values (P1 - 2.4±1.14, and 2.2±0.45, versus P2 - 2.2±0.45, and 2±0.71, for 0 and 1.5 ms/μm^2, 0 and 2 ms/μm^2, respectively).

Across 5 patients, for P1-P3 protocols presented side-by-side to the radiologist, dMRI P1 protocol was the preferred one, with two cases where P2 protocol could be used in exchange due to better prostate-background tissue contrast. The selection of the P1 protocol was supported by improved diffusion contrast, i.e., more signal within prostate gland at high b-values, however not always

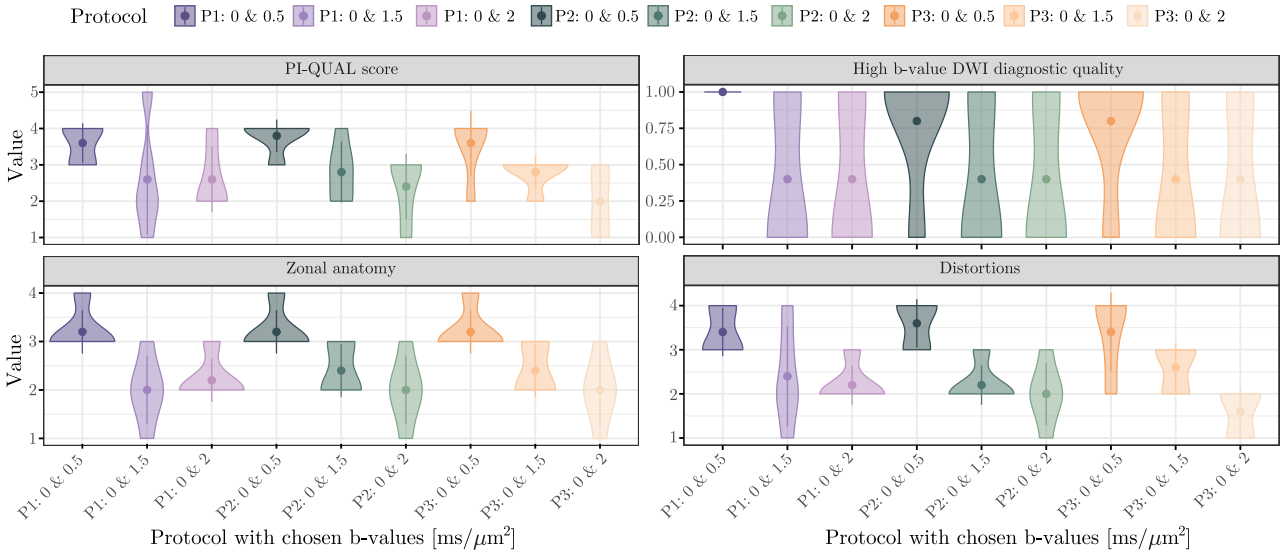

Figure 5.10: Image quality assessment by expert radiologist. Violin plots (trimmed to the range of the data) showing distributions and average scores with standard deviations for overall image quality (with 1: poor to 5: excellent), clinical utility of acquired high b-value image (binary scale: 0-1), zonal anatomy (1: poor to 5: excellent) and distortions (1: severe to 5: no influence) for different combinations of dMRI protocols. The associated standard deviations are also indicated for all scores, apart from quality metric using binary scale.

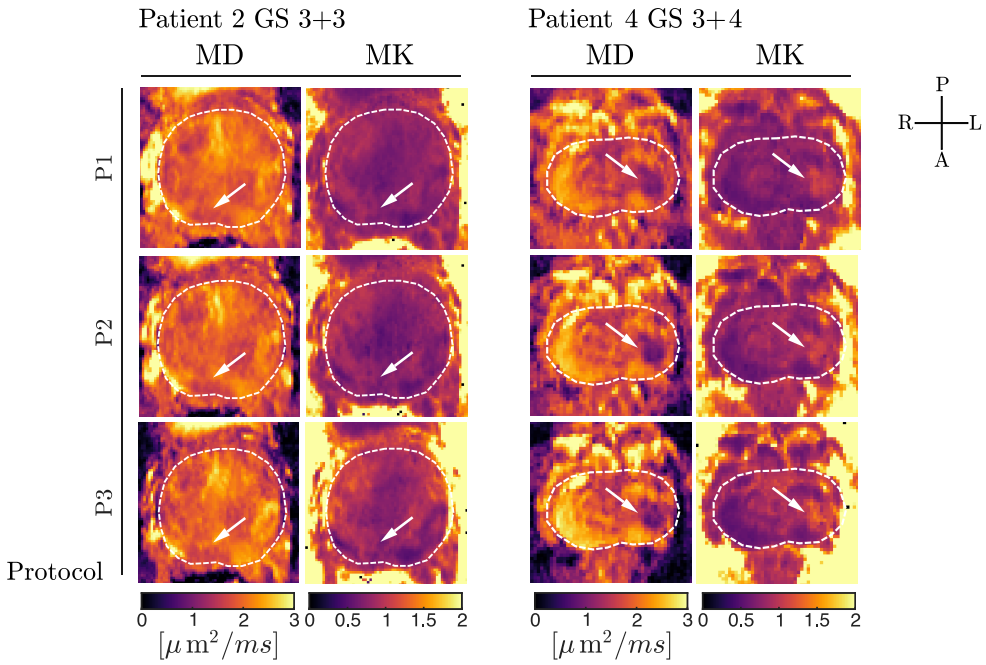

Figure 5.11: Quantitative results. MD and MK maps estimated from data of two patients (P1-P3 protocols). The cancerous lesions are indicated with white arrows.

unequivocal for confident lesions delineation. Importantly, it was commented that even though more signal present in the surrounding tissue could be seen as 'distortions', the gain of the signal within prostate gland was still valuable.

5.3.6 DKI parametric maps

DKI parameters maps (Figure 5.11) show differences in values estimates due to different diffusion time effects and relaxation effects captured with P1-P3 dMRI protocols. For P1 protocol, the maps are more homogeneous in lesion in comparison to P2 and P3 and also show the lowest estimates of MD and MK in prostate gland. The best contrast between cancerous lesion and healthy tissue is observed in the P3 protocol (e.g., Patient 4).

5.4 Discussion

This study showed the feasibility of employing ultra-strong gradient dMRI for prostate imaging in healthy subjects and patients diagnosed with PCa. Particularly in cancerous tissue characterised by increased restriction, higher b-values at sufficient SNR can provide novel information. The results show that employing stronger gradients and thus higher b-values at shorter TE (and diffusion times) enhances the conspicuity of cancerous lesions in patients with suspected clinically relevant prostate cancer.

5.4.1 Data quality and artefacts

dMRI commonly suffers from artefacts such as gradient-induced vibrations, eddy currents, gradient nonlinearities and susceptibility-induced off-resonance fields [Tax et al., 2022]. These effects may be amplified with strong gradients and particularly off-resonance fields caused by magnetic susceptibility differences can be more prominent in abdominal imaging compared to, e.g., brain. This, in turn, can cause a significant deterioration of data quality such as signal pile-ups or stretching, image misalignment, and signal drop-out, potentially resulting in poor depiction of the zonal anatomy and outweighing the expected benefits of strong gradients.

5.4.1.1 Susceptibility artefacts

Upon thorough visual evaluation, the quality of the acquired datasets using different maximum gradient strength was satisfactory as also supported by the radiologist's evaluation. Susceptibility artefacts were modest with no severe susceptibility artefacts due to gas in the rectum in both groups, and could be corrected using blip-up/blip-down Field Map Estimation ('topup' in FSL) [Andersson et al., 2003]. However, the estimation and correction of susceptibility induced distortions may not have been completely accurate in all acquired datasets as the 'topup' approach suffers from the lack of a unique solution between the corresponding locations in the blip-up and blip-down images. However, the reported results (Figure 5.7 and 5.8) are not severely affected by signal pileups, leading to blurring in the post-topup images.

Alternatively, the Direct Field Map approach can be used in which a separate gradient echo sequence is used to estimate the B_0 field map [Jezzard and Balaban, 1995]. It was shown that pixel shifts and distortions in prostate dMRI can be corrected for [Tong et al., 2019]. More recently,

a joint reconstruction framework for prostate dMRI was proposed which accounts for changes or inaccuracies in the B_0 field due to any potential origin such as scanner frequency drift, motion or physiological changes near the prostate-rectal area [Usman et al., 2019, 2020]. The combination of the model based reconstruction with dynamic B_0 field estimation improved dMRI images quality. However, it requires to acquire double the amount of data, i.e., both blip-up and blip-down directions for selected diffusion gradient scheme, and therefore significantly increases the scan time.

5.4.1.2 Eddy current-induced distortions

Regarding eddy-current image distortions, the alignment of the non diffusion-weighted images (which have the highest SNR) and diffusion-weighted volumes varied across participants. Qualitative assessment across protocols (P1-P3) revealed more substantial misalignment between non diffusion-weighted images in the protocol with the highest gradient strength (P1) across all subjects. The suggested cause of this are EC effects as an image shift in PE-direction is caused by slice-direction or B_0 EC in EPI-based acquisitions, and B_0 EC on the Connectom system have longer decay times (data unpublished; provided by system manufacturer) than the reported $\sim$ 260 ms in the literature [Jehenson et al., 1990]. We hypothesise that dMRI data acquired with P1 is the most affected by EC (including shearing and stretching, coming from read-direction and phase-direction EC) as EC effects scale with gradient amplitude. However, the visual assessment of EC-induced misalignments in single shot images unique to each diffusion-encoding (b-value and direction) turned out to be challenging and less trivial than in brain, therefore we only investigated those effects at 0.5 ms/µm^2 (Figure 5.3). Additionally, we suspect that higher or similar degree of residuals of acquired signal and estimated from DKI (results not shown) for 300 and 80 mT/m can be caused by interaction of motion and EC.

A common method to correct for EC in brain dMRI is combined predictive modelling with standard registration techniques (e.g. 'eddy' in FSL [Andersson and Sotiropoulos, 2016]). However, image registration-based method may fail to perform satisfactorily in body applications due to lower SNR [Kale et al., 2009, 2008] and less apparent tissue contrast than in brain. We adopted a minimal processing approach and plan to further evaluate EC correction in future work. Alternative approaches to address EC-based distortions such as EC-compensated diffusion gradients [Aliotta et al., 2018] for single-refocused SE or EC-correction methods [Mueller et al., 2017] in twice-refocused SE [Reese et al., 2003] can null EC induced fields. However, applicability of those are the cost of either requirement to access sequence source code to implement new optimisation schemes or increased TE, compared to the Stejskal-Tanner experiment with symmetric trapezoidal gradients.

5.4.1.3 Gradient non-linearities

Gradient linearity is often sacrificed in high-performance whole-body or head-only ultra-strong gradient systems [Foo et al., 2020, Jones et al., 2018, Setsompop et al., 2013, Weiger et al., 2018]. Discrepancies between effective and expected gradients emerge as geometric image deformations, with associated signal intensity deviations, and discrepancies from the intended diffusion encoding.

On the Connectom system used in this study, dMRI data is not corrected for gradient non-linearities during online image reconstruction with currently available programmes.

Even though the prostate is a small gland, correction for the GNL effects is crucial before any further quantitative dMRI analysis, as all b-values are affected [Guo et al., 2021], and if uncorrected, it can lead do biased results. Nevertheless, our results show that also lower b-values are affected. Therefore, spatially-varying b-matrix discrepancies, i.e., each voxel having a unique b-matrix, resulting from GNL have to be accounted for to limit biases of the estimated diffusion coefficient [Bammer et al., 2003], diffusion tensor directions and DTI/DKI scalar measures [Mesri et al., 2020], and measures derived from b-tensor encoding [Paquette et al., 2020]. Although it was investigated so far in brain, those errors can be problematic in big clinical trials, e.g., INNOVATE [Singh et al., 2022], once extended to different centres.

5.4.1.4 Motion

Subject motion can be an important confounding effect, which can cause misalignment between images and signal drop-out (result of phase dispersion) when occurring during diffusion-encoding. In our study, we did not use any hypotonic agents to control peristalsis, or perform breath-hold acquisitions. Since patient preparation is not specified in PI-RADS v2 [Turkbey et al., 2019, Weinreb et al., 2016], we solely advised participants to follow a light diet for 24 hours and fast on the day of the scan to minimize image artefacts. Even though this step is not necessary, [Engels et al., 2020]), it may help to limit bowel activity and therefore decrease distortions close to the PZ-rectal wall.

5.4.1.5 Rician bias

dMRI was reconstructed using 'adaptive combine' [Setsompop et al., 2012], and therefore the magnitude data are Rician distributed. For low SNR magnitude data, e.g., long TEs and/or ultra high b-values, one observes a spurious SNR-dependent signal increase – the noise floor. This signal bias propagates in all diffusion measures if not corrected for before fitting [Koay et al., 2009, Veraart et al., 2013] or not accounted for during model fitting [Jones, 2004, Veraart et al., 2013]. For example, the impact of such noise bias has been observed in DKI (overestimated kurtosis) [Veraart et al., 2011]. For our acquisitions, for a given b-value, shortening the TE by means of stronger gradients, and thus increasing data SNR, should help reducing the impact of the Rician bias. Preferably more recent strategies relying on complex-data [Cordero-Grande et al., 2019, Eichner et al., 2015] could be applied to remove the bias early in data pre-procsessing.

5.4.2 Study limitations

There are several limitations to this study. The sample sizes of healthy controls and clinical cohort were small and not per se demographically matched. Moreover, the protocol was designed to obtain the highest b-value per given TE for three different gradient strengths disregarding diffusion time-dependence and transverse relaxation effects. This study focuses on assessing the cancerous-to-healthy tissue contrast enhancement and data quality and future work will study time- and

TE-dependence into more detail. Lastly, the data processing did not include any steps to correct for EC, signal drift or inter-image motion, which may have a residual effect on the presented analyses. To address majority of the challenges in the data processing, one would obtain on-the-fly accurate information about scanner instabilities and gradient system imperfections, e.g., through concurrent field monitoring, so that information about MR field perturbations could be leveraged at the data reconstruction stage [Wilm et al., 2015] (Chapter 6).

5.4.3 Future directions

The tissue-background contrast of dMRI at 2-3 ms/μm^2 with strong gradients are significantly higher in healthy and patient cohorts. Moreover, significantly shorter TEs are achievable owing to shortened time for diffusion encoding, provided significant SNR gains at higher b-values and more residual signal in lesions. These advances can be even more powerful in combination with radiotherapy to deliver more precise tumour delineation in the radiotherapy planning process [Beaton et al., 2019].

Currently, ADC is actively used as a biomarker aiding in identifying suspicious lesions in men with suspected prostate cancer. However, a recent study recognized that changes in epithelium, stroma, and lumen signal fractions estimated from MR data correlate more strongly with Gleason grade than any cellularity metrics from histological data (e.g., nuclear count) [Chatterjee et al., 2022b, 2015]. Our proof of concept adaptation of strong gradients in prostate imaging shown in this work, holds great potential for quantifying microstructure heterogeneity which is an important consideration in Gleason scoring for prostate cancer [Kweldam et al., 2019] as some of the lesions are not MR-invisible [van Houdt et al., 2020]. Moreover, in this study, we observed the effects of average T_2 of the underlying tissue on the contrast in maps from the DKI representation. This dependence hints that indeed choosing a certain TE may maximise this contrast; strong gradients allow for this to be investigated and optimised in experiments. Ultimately, as stronger gradients become more available, they can enable widespread adaptation of comprehensive characterization of the prostate in a multidimensional space [Langbein et al., 2021, Nilsson et al., 2021], at different TEs [Chatterjee et al., 2018, Lemberskiy et al., 2018, Zhang et al., 2020], and range of diffusion times to explore time-dependence effects [Lemberskiy et al., 2017, Palombo et al., 2020b, Reynaud, 2017, Wu et al., 2022]. Our study is a first important step towards showing the feasibility and highlighting the benefits, and demonstrating that they outweigh potential confounds.

5.5 Conclusions

This works addresses the main technical impediment of clinical dMRI in prostate: low SNR at high b-values. The benefits of 300 mT/m gradients compared to more commonly-available gradient strengths outweigh their drawbacks as a significant gain in sensitivity to signal restrictions occurring in low-grade PCa. Strong gradient amplitudes enable novel acquisitions which in turn can improve specificity and/or sensitivity of current MRI methods for prostate cancer characterisation and detection.

Chapter 6

Enhanced Diffusion and Spatial Resolution Prostate dMRI using Spiral Readout and Expanded Encoding Model

Contents

6.1 Introduction

Strong diffusion weighting can provide unique information for the characterisation of tissue microstructure. Among other applications, it holds promise for advancing the early detection of PCa [Johnston et al., 2019, Panagiotaki et al., 2015], by allowing the separation of intra- and extracellular signal contributions and, in turn, reducing the number of performed biopsies. Unfortunately, clinical dMRI suffers from inherently limited diffusion weighting per unit time due to the low gradient amplitudes available on current MR systems. This leads to prolonged TEs and low SNR, all of which limit diagnostic efficacy.

Acquiring higher b-values with weaker clinical gradients, e.g., 40 mT/m, inevitably results in longer TEs (e.g., in VERDICT analysis [Panagiotaki et al., 2015]), which, in turn, increases chances of motion and signal drift. Moreover, data correction by means of image registration is especially challenging at high b-values. As shown in Chapter 5, advancement in gradient hardware enabling higher b-values per unit time, allows for lesion-to-healthy tissue contrast enhancement. However, strong diffusion gradients can inherently lead to more severe eddy current effects, which consequently results in inaccurate localisation, misrepresentation of tissues, and misalignment between images [DeSouza et al., 2018, Koch and Norris, 2000, Kyriazi et al., 2010], having lasting impact on accurate delineation and characterisation of prostate lesions. Accounting for field perturbations through measurement using NMR probes can correct for the detrimental effects of, e.g., eddy currents with a high degree of accuracy [Wilm et al., 2011].

The typical EPI readout used in dMRI leads to prolonged echo times in classical PGSE experiments, as the k-space readout does not start at its centre, and thus, additional dead time has to be included to meet the spin echo condition. This becomes more detrimental in single shot high in-plane resolution acquisitions. Alternative readouts can be employed to increase the efficiency of signal sampling. The non-Cartesian spiral readout allows for maximisation of time for diffusion encoding as the readout trajectory starts at the centre of k-space. This enables shorter TEs and SNR benefits. Moreover, spiral trajectories are efficient in sampling speed and can be straightforwardly adapted to take into account constraints, e.g., PNS, on a point-by-point basis as opposed to EPI for which those have to be considered globally.

This works demonstrates considerable enhancement of dMRI quality and tissue-to-lesion contrast in prostate as a result of combining 300 mT/m gradients for diffusion encoding with spiral readouts for spatial encoding, accounting for field perturbations in the image reconstruction [Wilm et al., 2015]. We present prostate dMRI with high b-values at short echo times for microstructural tissue characterisation. Our objective was three-fold: (i) to reduce geometrical distortions resulting from MR system imperfections, (ii) to boost SNR, and (iii) to improve in-plane resolution. The feasibility of this approach is demonstrated in a healthy subject and a patient diagnosed with prostate cancer.

6.2 Materials and Methods

6.2.1 NIST isotropic diffusion phantom

An isotropic diffusion phantom containing multiple vials in a 3D-printed shell developed at the National Institute of Standards and Technology, (NIST; current official producer CaliberMRI, previously called QualibreMD) [Keenan et al., 2018] was used for sequence testing. This phantom has an array of thirteen 30-mL cylindrical vials filled with variable amounts of the polymer polyvinylpyrrolidone (PVP) with mass fractions of 0% (de-ionized water), 10%, 20%, 30%, 40%, and 50% and resulting diffusivities of 1.127, 0.843, 0.607, 0.403, 0.248, and 0.128 $\mu m^2/ms$ at 0°C, respectively. The phantom was placed in the scanner with the principal axis of the vials pointing along the main magnetic field direction, therefore, the cross-section of vials was imaged in the axial plane.

6.2.2 Study participants

Ethical approvals for the study were obtained from the School of Psychology Research Ethics Committee (REC) of Cardiff University and from the REC of the National Health Service (NHS), Wales (Health Research Approval, HRA, and Health and Care Research Wales, HCRW) (CVUHB ref 21/OCT/8264).

One healthy control (age: 51 years, weight: 75 kg, height: 1.68 m) and one patient (age: 53 years, weight: 69.5 kg, height: 1.61 m) with GS 3+3 PCa were scanned after providing written consent. We advised our participants to follow a diet for 24 hours prior to imaging to reduce the risks of artefacts in the data.

6.2.3 Data acquisition

Images were acquired on a 3T Connectom research-only scanner (Siemens Healthcare, Erlangen, Germany) using two surface coils (Body18 and Spine32). For both phantom and in vivo measurements the sequences used were as described below.

Multi-echo gradient echo (GRE) images were acquired for the estimation of static B_0 maps and receive coil sensitivities. The imaging parameters were: TEs = 2.32/4.64/6.96/9.28 ms, TR = 547 ms, in-plane resolution = 3.07 × 3.07 mm, slice thickness = 5.0 mm, number of slices = 18.

A prototype PGSE sequence with the flexibility of using arbitrary readouts (Figure 6.1 A.) was used to acquire dMRI images along 15 non-collinear directions distributed on a sphere at b = [0, 0.05, 0.5, 1.5, 2, 3] $ms/\mu m^2$ (G_{max}= 247 mT/m, SR = 83.3 T/m/s, δ = 5.7 ms, Δ = 23.3 ms) and TEs of 53 and 35 ms for EPI and spiral, respectively, TR = 3 s, in-plane resolution = 1.3 mm, slice thickness = 5 mm, and 18 slices without gap. Importantly, the resolution of the spiral readout is defined by the k_{max} of the outermost trajectory evolution. EPI and spiral readouts were designed in MATLAB using prototype code and the Time Optimal Gradient Design toolbox [Lustig et al., 2008], respectively, and were matched in length and spatial resolution (i.e., covered k-space area, Figure 6.1 B.); for both: G_{max} = 39.11 mT/m, SR_{max} = 186.24 T/m/s, for EPI: undersampling factor

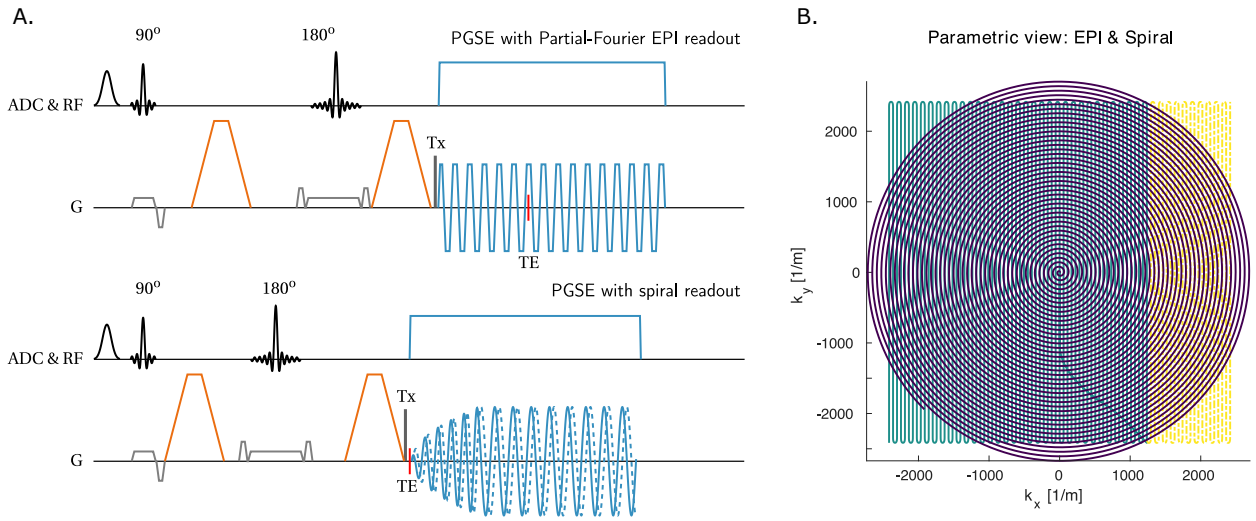

Figure 6.1: A. Sketch of the Stejskal-Tanner diffusion encoding sequence diagrams: Single-shot EPI readout (*top*) and single-shot spiral readout (*bottom*). The EPI product sequence had additional navigators for phase correction [Heid, 1997] (not shown). ADC (here analog to digital converter) & RF: Spectral fat (Gaussian) saturation, excitation and refocusing pulses (*in black*), and ADC event (*in blue*). G: Slice selective and refocusing gradients with crushers/spoilers (*in light grey*), diffusion gradients (*in orange*), readout event (EPI or spiral, *in blue*), and trigger for dynamic field camera (Tx, *in dark grey*). B. Parametric view of matched k-space area coverage: partial Fourier EPI (*blue line*, *yellow dashed line* indicates reconstructed points) and spiral (*purple line*).

(R_{UF}) = 2, partial Fourier factor = 6/8, phase encoding = anterior-posterior, and for spiral: R_{UF} = 2.24). For the sequence comparison, dMRI with the vendor's PGSE EPI sequence was acquired, with the EPI readout train matching the one in the prototype sequence (referred to as the 'Reference EPI', in short 'Ref. EPI').

In addition, a dMRI dataset from a healthy participant using the high resolution spiral was acquired (Section 6.2.3.1). The maximum PNS tolerance was 96% of the maximum allowed according to the SAFE model, with 4% buffer, allowing for remaining PNS from sequence modules other than the readout train to occur. Spiral readout length was 76.43 ms, G_{max} = 45.78 mT/m, SR_{max} = 200 T/m/s, with remaining sequence parameters as described in the previous paragraph. Overall, each of the dMRI protocols took 4 min, 45 s.

Structural MRI scans were acquired using a 2D T2-weighted TSE sequence in the axial plane (voxel size = 0.625 × 0.625 × 3 mm).

The magnetic field dynamics during the readout were monitored in a separate experiment using a dynamic field-camera (Skope Magnetic Resonance Technologies) [Dietrich et al., 2016]. To this end, the prototype sequence was equipped with a trigger event followed by a 500 ms gap free of any gradients right before the start of the readout. As MR raw data and field monitoring data are acquired on two different spectrometers, the relative delay between the data has to be found for the reconstruction to perform optimally. In our framework, a method which uses an artificial time varying RF signal (proposed by Skope Magnetic Resonance Technologies) is deployed. The method estimates the relative delay between the signals fed into the field probes and the receive coils. This value determines the best alignment of both signals.

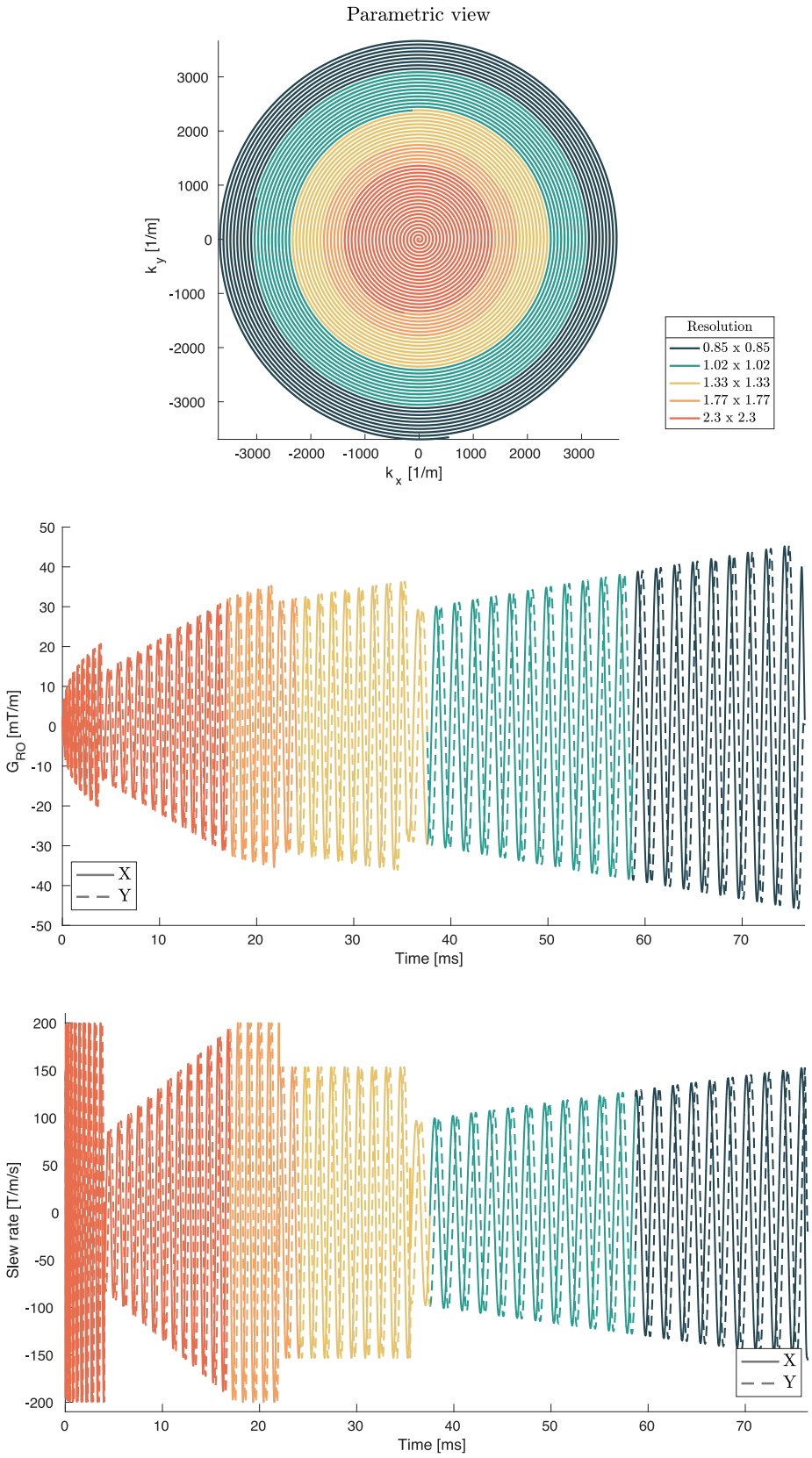

Figure 6.2: Overview of high resolution spiral readout parametrisation. k-space parametric view showing the k-space coverage of the readout for a set of resolutions, where for the finest resolution, k-space points depicted by all colours (resolutions) are included in the reconstruction (*top*). For the same set of resolutions, the readout gradient and slew rate time courses are depicted (*middle* and *bottom panel*, respectively); for the finest resolution, the complete readout trajectory is composed of all 'colored' readout segments.

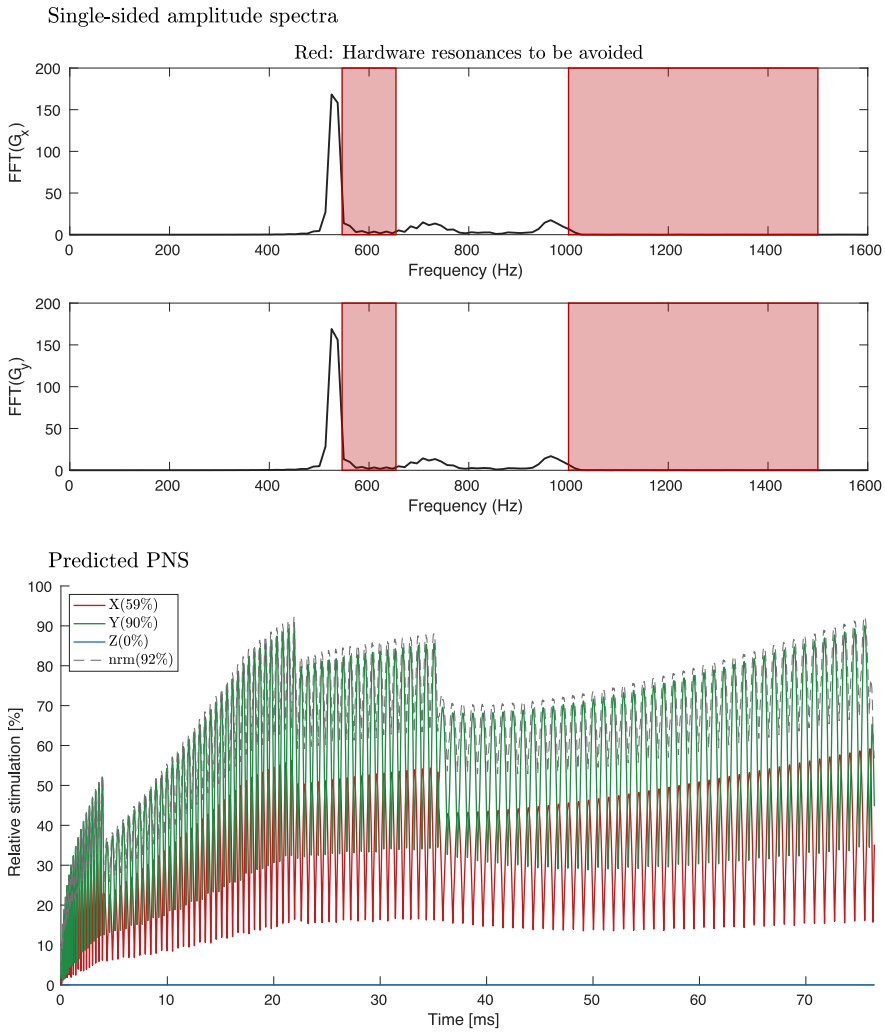

Figure 6.3: Properties of the optimised high resolution spiral readout. (*top panel*) Frequency content of the readout gradients (*black line*), with overlaid hardware resonances (*red boxes*). (*bottom panel*) Predicted PNS using SAFE model.

6.2.3.1 High in-plane resolution spiral readout optimisation

In any gradient design, e.g., diffusion or readout gradients, one should include constraints to avoid any unwanted effects such as PNS (SAFE model, [Hebrank et al., 2000]) and hardware resonances. Including those constraints becomes especially valuable for high resolution readouts, as otherwise one would have to operate using very low slew rates in order not to hit the PNS limit, which then extends the readout excessively. Moreover, for larger radii of the spiral (due to higher resolution) one could enter critical hardware resonance bands (mechanical resonances).

Therefore, we included constraints to account for PNS and hardware resonances in the design of high-resolution spiral readout. By default, the Time Optimal Gradient Design toolbox does not include those in the trajectories optimisation. For a single gradient axis (e.g., x), the k_x Cartesian coordinate of the spiral trajectory (in polar coordinates, $(R, \omega t)$) is defined as:

$$k_x = R\sin(\omega t) \overset{\mathrm{d}t}{\rightarrow} G_x = \frac{\omega R}{\gamma}\cos(\omega t) \overset{\mathrm{d}t}{\rightarrow} S_x = -\frac{\omega^2 R}{\gamma}\sin(\omega t) \tag{6.1}$$

where R is the radius of the circle in k-space, i.e., a certain distance from the k-space origin, and maximum gradient amplitude and slew rate are:

$$G_{max} = \frac{\omega R}{\gamma}, \tag{6.2a}$$

$$S_{max} = \frac{\omega^2 R}{\gamma}. \tag{6.2b}$$

To avoid certain frequency bands, it has to be calculated at which point on the spiral pathway which frequency is hit. Thus, we approximate any given point on the trajectory with a circle to find the radius R_{thr} (threshold radius) from which onward one would be operating at maximum speed. We are interested in maximum speed as we approximate the feasible velocity in k-space with that one of a circle of the same radius R. Therefore, the imposed constraints are:

- amplitude limit:

$$G_{max} = \frac{\omega R}{\gamma} \rightarrow f = \frac{\gamma G_{max}}{2\pi R} \rightarrow R = \frac{\gamma G_{max}}{2\pi f} \tag{6.3a}$$

$$\text{if } R_{LB}(f) > R > R_{UB}(f) \rightarrow G_{max} = \frac{2\pi f_{LB} R}{\gamma} \tag{6.3b}$$

- slew rate limit:

$$\omega = \sqrt{\frac{\gamma S_{max}}{R}} \rightarrow f = \frac{1}{2\pi}\sqrt{\frac{\gamma S_{max}}{R}} \rightarrow R = \frac{\gamma S_{max}}{(2\pi f)^2} \tag{6.4a}$$

$$\text{if } R_{LB}(f) > R > R_{UB}(f) \rightarrow S_{max} = \frac{R}{\gamma}\left(2\pi f_{LB}\right)^2 \tag{6.4b}$$

where R_{LB} and R_{UB} stand for lower and upper radius bound.

The maximum speed is reached when the system is at gradient amplitude limit (i.e., Equation 6.2a holds true) and for this gradient amplitude, the slew rate can be anything smaller or equal to the maximum slew rate given by Equation 6.2b. If we resolve for ω, we obtain:

$$R_{thr} = \gamma \frac{G_{max}^2}{S_{max}}. \tag{6.5}$$

The spiral readout operates in amplitude limit for $R \geqslant R_{thr}$ and in slew rate limit for $R < R_{thr}$ with R_{thr} defined by Equation 6.5. If for both modes we express the radius R as a function of the frequency (Equations 6.3a and 6.4a) and thus find the radius ranges which hit hardware resonances. In the given ranges, if there was a likelihood of hitting hardware resonance or activation of PNS watchdog, the algorithm reduced the maximum slew rate/gradient amplitude such that these frequency bands are avoided (Equations 6.3b and 6.4b). The designed spiral is then broad-banded, i.e., it sweeps through a wide band of frequencies.

The algorithm relies on user dependent choice of maximum PNS tolerance and width of the frequency band (defined by the scanner's vendor during assessment of mechanical vibrations of the system).

6.2.4 Data reconstruction

The dMRI EPI data acquired with the vendor's PGSE sequence were reconstructed using a GRAPPA-based reconstruction [Griswold et al., 2002] provided by the vendor.

The data acquired with the prototype sequence were reconstructed using an expanded encoding model [Wilm et al., 2011, 2015] (SENSE-based approach) [Pruessmann et al., 2001] including static B_0-inhomogeneities, coil sensitivities and the measured field dynamics (up to 3rd-order spherical harmonics and 2nd-order concomitant fields [Bernstein et al., 1998, Vannesjo et al., 2016]). For those reconstructions, the vendor's correction of B_0 eddy currents was undone prior to feeding the coil data into the reconstruction, which was performed using commercially available software (Skope-i, Skope Magnetic Resonance Technologies). In addition, to evaluate the degree of image distortions caused by system imperfections, the patient data were reconstructed with prescribed trajectories (EPI and spiral), i.e., the measured field perturbations were disregarded, without undoing the vendor's B_0 EC correction, but including static B_0-inhomogeneities.

Since the nominal resolution is given by the covered k-space extent, i.e., in case of the spiral-out how long the trajectory is allowed to go on rotating outward, the impact of the nominal resolution on actual resolution and SNR can easily be studied by trimming the number of k-space samples included in the reconstruction. This was done for a range of different resolutions. Therefore, we reconstructed data from the full readout train for the prescribed resolution of 0.85 $\times$ 0.85 mm for spiral (0.96 $\times$ 0.96 mm for quadratic k-space area, such as EPI, based on formula $\mathrm{res}_{\mathrm{spiral}} = \frac{\sqrt{\pi}}{2} \cdot \mathrm{res}_{\mathrm{EPI}}$); the remaining resolutions were: 2.30, 2.04, 1.77, 1.60, 1.33, 1.15, 1.02, 0.87 mm (corresponding to 2.60, 2.30, 2.00, 1.81, 1.50, 1.30, 1.15, 0.98 mm for EPI). The reconstruction matrix size was kept constant across all resolutions leading to different degrees of zero-filling for the trimmed spiral readouts/lower resolution reconstructions. The most coarse resolutions were defined according to the PI-RADSv2 guidelines [Turkbey et al., 2019, Weinreb et al., 2016], i.e., the maximal voxel volume could be $\leqslant$ 25 mm^3 (2.5 $\times$ 2.5 $\times$ 4 mm). In our study, the biggest voxel volume reconstructed with high resolution spiral is higher, $\approx$ 27 mm^3 (2.3 $\times$ 2.3 $\times$ $\times$5 mm) which corresponds to $\approx$ 34 mm^3 in EPI). Figure 6.2 shows the k-space parametric view for a set of resolutions (*top panel*), and time courses of readout gradient (G_{RO}) amplitudes (*middle panel*) and SR for a set of selected resolutions (*bottom panel*). Figure 6.3 shows the spectra of the G_{RO} (*top panel*) and predicted PNS over the time course of the readout (*bottom panel*).

6.2.5 Data processing and analysis

dMRI images were corrected for gradient nonlinearity induced distortions [Bammer et al., 2003, Jovicich et al., 2006], and spatio-temporal b-matrices [Rudrapatna et al., 2021] were computed. For qualitative analysis, direction-averaged signals were calculated for each shell.

6.2.5.1 NIST phantom data

Phantom data were used to assess eddy current-induced distortions and to evaluate the diffusivity estimation for two types of readouts (EPI and spiral).

The degree of eddy current induced image artefacts in the data reconstructed with the vendor's default reconstruction programme and the expanded encoding model, was assessed with a pixel-wise coefficient of variation (CoV) of diffusivities for a given b-shell [DeSouza et al., 2018]. The diffusivities were estimated assuming mono-exponential decay for each diffusion direction for all sampled b-values separately, and the CoV was calculated as $\frac{\sigma}{\mu} \cdot 100\%$, where σ is standard deviation, and μ is mean value of the estimated diffusivity across all directions.

A diffusion tensor model with non-linear weighted least squares fit [Sairanen et al., 2018], which decreases the weighting of outliers, was estimated from the data acquired with the prototype sequence to evaluate the accuracy and precision of the mean diffusivity estimation. The voxel-wise estimates of MD were extracted from within the vials of a single slice (Figure 6.5) and grouped based on the concentration of the PVP. The voxel extraction mask was defined on the b = 0 ms/μm^2 image acquired with spiral readout using an automatic edge detection algorithm with erosion to exclude voxels in proximity of vial edges. Means with standard deviations with parameter distributions (kernel probability density of the data at different values) were obtained. Importantly, since for our measurements the phantom was not cooled down to 0°C, we used scaling coefficients as reported in [Wagner et al., 2017] for PVP K30 used in the phantom [Boss et al., 2014, Pierpaoli et al., 2009], to compare the measured mean diffusivity at 22°C with the reported ground truth values in the phantom manual.

6.2.5.2 In vivo data

In the ROI analysis of the direction-averaged signals, the estimated noise floor in each ROI was calculated using the method from [Gudbjartsson and Patz, 1995, Jones and Basser, 2004].

For quantitative analysis, MD, FA, MK, AK, and RK were computed [Veraart et al., 2013], accounting for b-matrix deviations.

SNR maps were determined using the 'pseudo multiple replica method' [Robson et al., 2008] following the steps as in [Lee et al., 2021b]. First, the covariance matrix of noise in raw data was calculated from noise prescans (without gradient and RF transmission). Gaussian noise of the same covariance was then added to the given raw k-space data, followed by image reconstruction. Noise maps were estimated from 200 image reconstructions, i.e., with 200 different noise instances as the pixel-wise standard deviation of image magnitude. Magnitude SNR maps were calculated by dividing a magnitude image reconstructed without additional noise by the respective noise maps. The SNR analysis was performed using the data from the healthy participant, across all directions and all b-values, but only for a single slice to limit computation time. Voxel-wise percent SNR gain of spiral over EPI images was calculated as SNR_{gain} [%] = 100 · (SNR_{spiral} - SNR_{EPI})/SNR_{EPI}, where SNR_{spiral} and SNR_{EPI} are mean SNR of the spiral and EPI data across all voxels within a manually drawn mask outlining the prostate gland.

The degree of image misalignment caused by long-term EC and susceptibility effects (likely to differ across slices and diffusion directions if the subject had moved) in in vivo data was assessed via calculation of the edge congruency maps using b = 0 ms/μm^2 images interleaved throughout the diffusion sampling scheme. The congruency map is defined as a sum of the binary masks (of each b = 0 ms/μm^2) containing edges of the tissue. The higher the value of the voxel in the congruency map, the more frequently the given voxel was classified as 'edge' during an automatic edge detection.

The high-resolution spiral dMRI dataset was in addition analysed quantitatively using Structural Similarity Index Measure (SSIM) [Wang et al., 2004], for which the set of the low resolution images only at b = 0 ms/μm^2 was compared to the ground truth high-resolution b = 0 ms/μm^2 image at 0.85 × 0.85 mm in-plane resolution.

6.3 Results

6.3.1 Phantom imaging: Eddy current-induced distortions

CoV maps of diffusivites (Figure 6.4) for acquisitions with the vendor's and prototype PGSE sequences show much higher values of the CoV for the Ref. EPI scans (vendor's sequence and reconstruction software) across all selected b-values, and are constantly high for the vials filled with the PVP of the highest concentration. High CoV values at the edges of the vials reflect directionally-dependent eddy current-induced distortions, which were minimised once the data were reconstructed with the expanded encoding model accounting for field inhomogeneities as well as EC. The significant improvement in reduction of distortions was obtained for both EPI and spiral readout with the prototype sequence. For Ref. EPI, the observed spatial distribution of high CoV appear quite clear around the vials and is consistent with the most likely occurrence, i.e., in EPI, in the phase encoding direction.

6.3.2 Phantom imaging: Accuracy and precision of diffusivity estimation

Figure 6.5 shows the estimation of the MD of PVP solutions of different concentrations. The estimated MD shows minor differences in accuracy between EPI and spiral readouts. For the 10% PVP concentration, MD is slightly more overestimated than for the remaining concentrations. Across all PVP solutions, the precision of the MD estimation is improved for the spiral readout as shown by the narrower distributions of parameter values.

6.3.3 In vivo data: dMRI sequence comparison and image alignment evaluation

Figure 6.6 shows single (*top row*) and average (*middle row*) b = 0 ms/μm^2 images acquired with either EPI or spiral readouts, reconstructed using two different approaches. Fine anatomical features are better defined when accounting for field perturbations using the expanded signal model (2nd vs

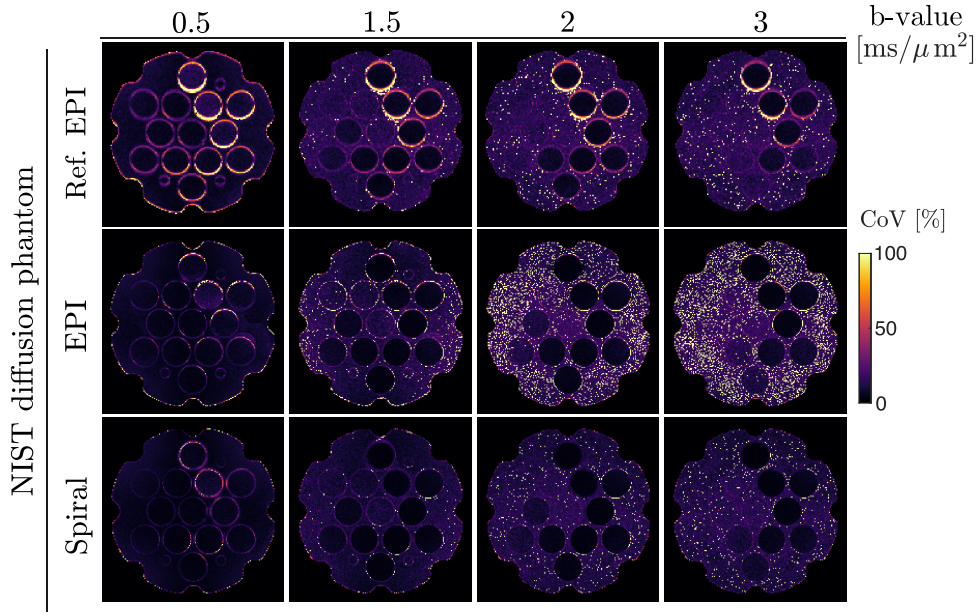

Figure 6.4: Evaluation of eddy current effects in a diffusion phantom. The CoV was measured across ADC maps of fifteen diffusion directions within each sampled b-value for dMRI data acquired with three sequences (vendor's PGSE sequence - Ref. EPI, prototype PGSE sequence with EPI and spiral readout.)

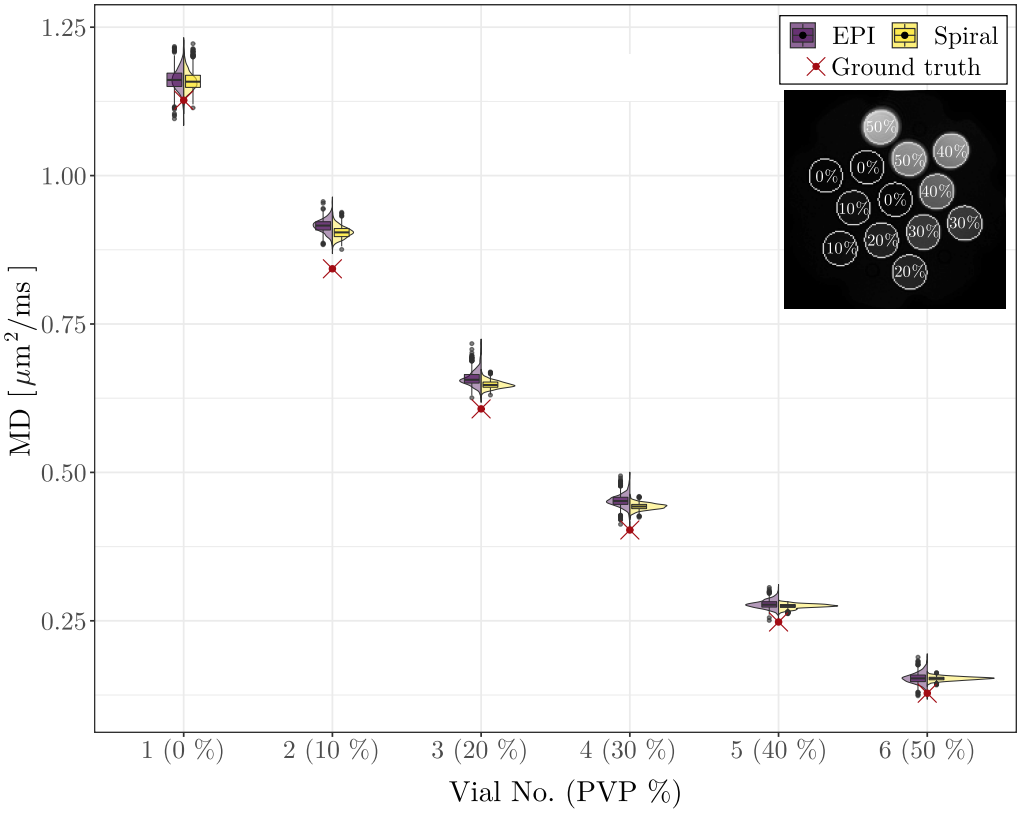

Figure 6.5: MD estimates of PVP solutions in diffusion phantom for EPI and spiral readout. Box plots (mean, standard deviations, and outliers - *black points*) with density plots of estimated values across voxels, with ground truth values are shown. The phantom image shows the corresponding mask (*white circles*) used to extract the voxel-wise values of the estimated parameters.

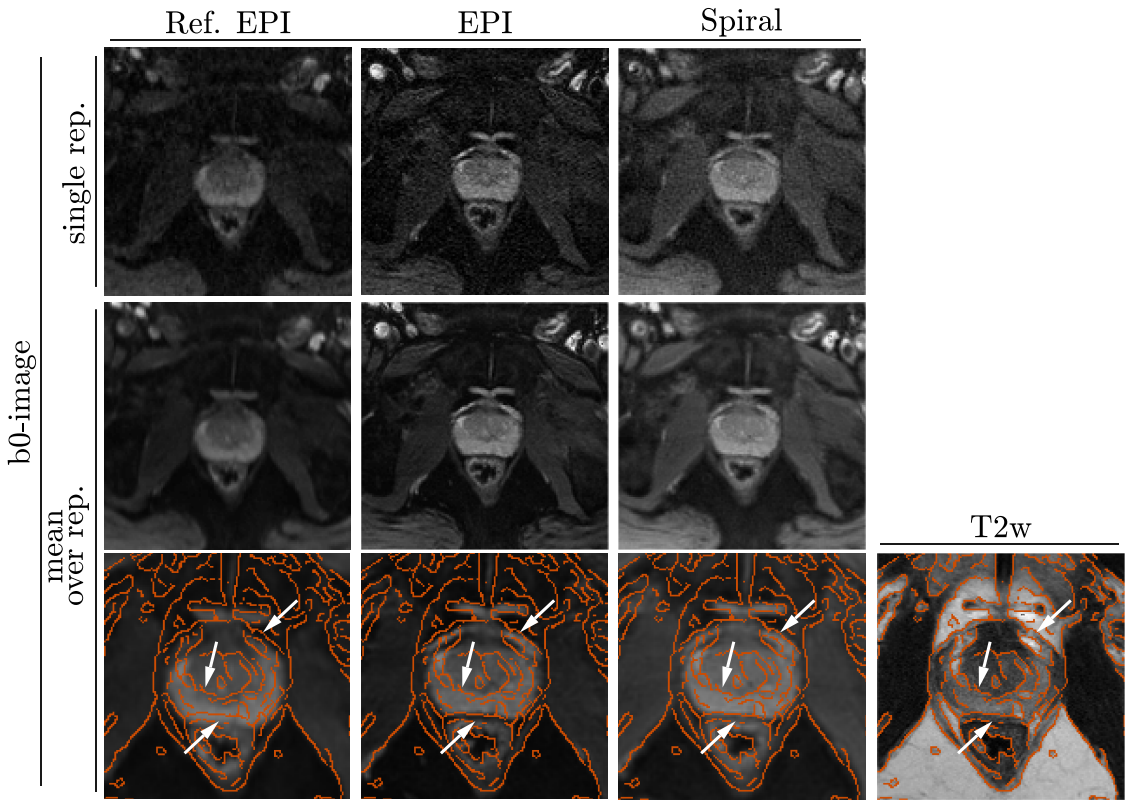

Figure 6.6: Qualitative evaluation of dMRI images acquired and reconstructed using different methods. A single b = 0 ms/μm^2 image (1st in each series of acquisition) from a patient imaged with three PGSE sequences: the vendor's EPI-sequence and prototype sequence with EPI and spiral readout (*top row*). Average b = 0 ms/μm^2 from three protocols (*middle row*), zoomed in and with overlaid edges detected on T2-weighted image (*bottom row*). The improved alignment of fine anatomical features across modalities is highlighted with white arrows.

1st column). The signal intensity in the prostate and surrounding muscles is higher at shorter TE (3rd column). In addition, the spatial correspondence of fine anatomical features clearly visible in the T2-weighted image, is better preserved in dMRI data reconstructed with the expanded encoding model.

The edge congruency maps calculated from b = 0 ms/μm^2 (Figure 6.7) confirm better image alignment across shots in data reconstructed with the expanded encoding model. Importantly, the fine features within the prostate gland and the surrounding tissue are more consistently delineated, e.g., between prostate PZ and rectum. For the Ref. EPI acquisition, the edges are more blurred due to B_0 and long term slice-direction EC that vary across the experiment and, if present, motion between shots, which was not apparent from the images.

6.3.4 In vivo data: SNR analysis

Magnitude SNR maps (Figure 6.8) confirm higher SNR in dMRI data across all b-values if acquired with spiral readout rather than EPI with partial Fourier. The mean of the SNR and gains within a prostate mask are reported alongside each image. The median values of SNR gains (with interquartile range given in the round brackets) of the spiral readout over EPI ranged between 31.34%

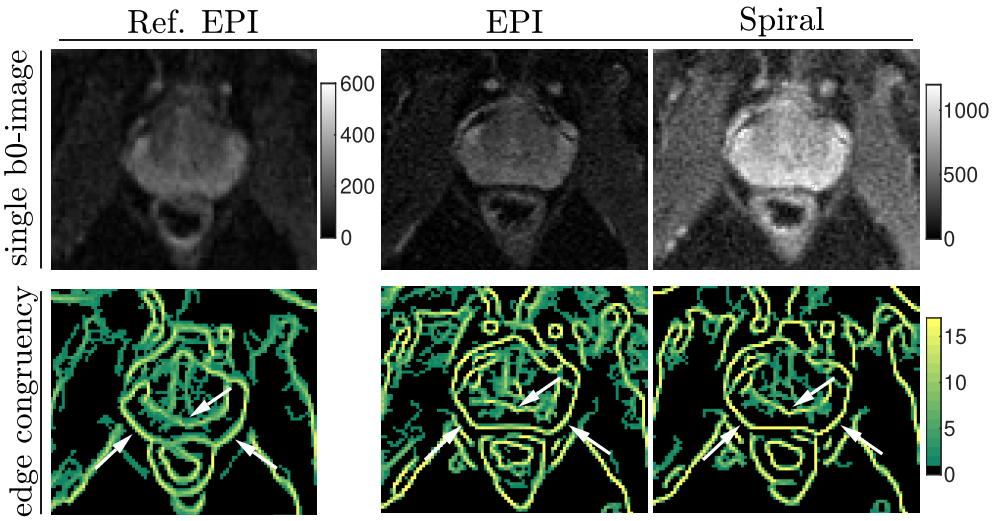

Figure 6.7: Image alignment evaluation in PCa patient. Edge congruency maps for b = 0 ms/µm^2 are shown for three sequences and two different reconstruction algorithms. The scaling of the map was defined by the total number of images at b = 0 ms/µm^2 that were acquired, e.g., bright yellow, 17, means the given voxel was detected as being an 'edge' voxel across all 17 b = 0 ms/µm^2 volumes. An example of areas of (in-)consistent edge detection are highlighted (*white arrows*); for those regions (e.g. the wall between PZ of the prostate and rectum), the best performance was achieved once the data were reconstructed with the expanded encoding model, regardless of the readout technique employed.

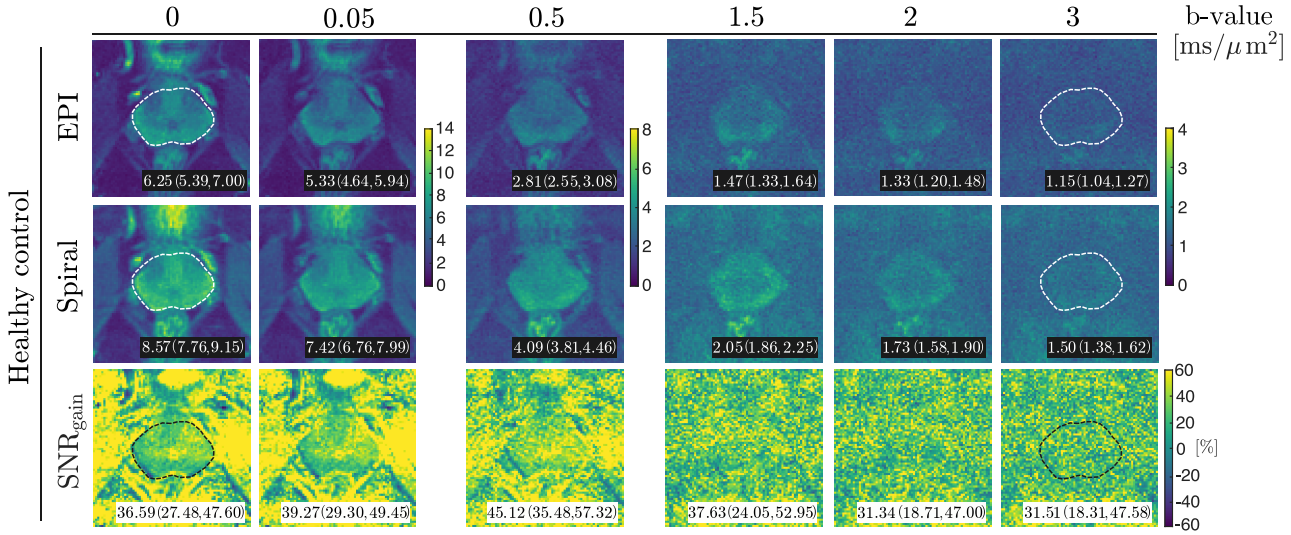

Figure 6.8: Magnitude SNR of b = 0 ms/µm^2 (1st column) and diffusion-weighted images from (2nd to last column) obtained with the sequences shown in Figure 6.1 (PGSE with EPI or spiral readout) reconstructed with the expanded encoding model. Note the different color scales between rows and columns. SNR gain maps are presented for each b-value (*bottom row*). Reported values in the bottom right corners of the images are median with interquartile range of SNR or SNR gain within the prostate mask (*white/black dashed line*), which for legibility of maps was only shown on the images from the lowest and highest b-values.

(18.71, 47.00) and 45.12% (35.48, 57.32), depending on the b-value, with the lowest obtained for b = 2 ms/µm^2, and the highest obtained for b = 0.5 ms/µm^2. Please note that only little signal is expected to be left for high b-values in a healthy prostate, hence, the SNR maps do not reflect the

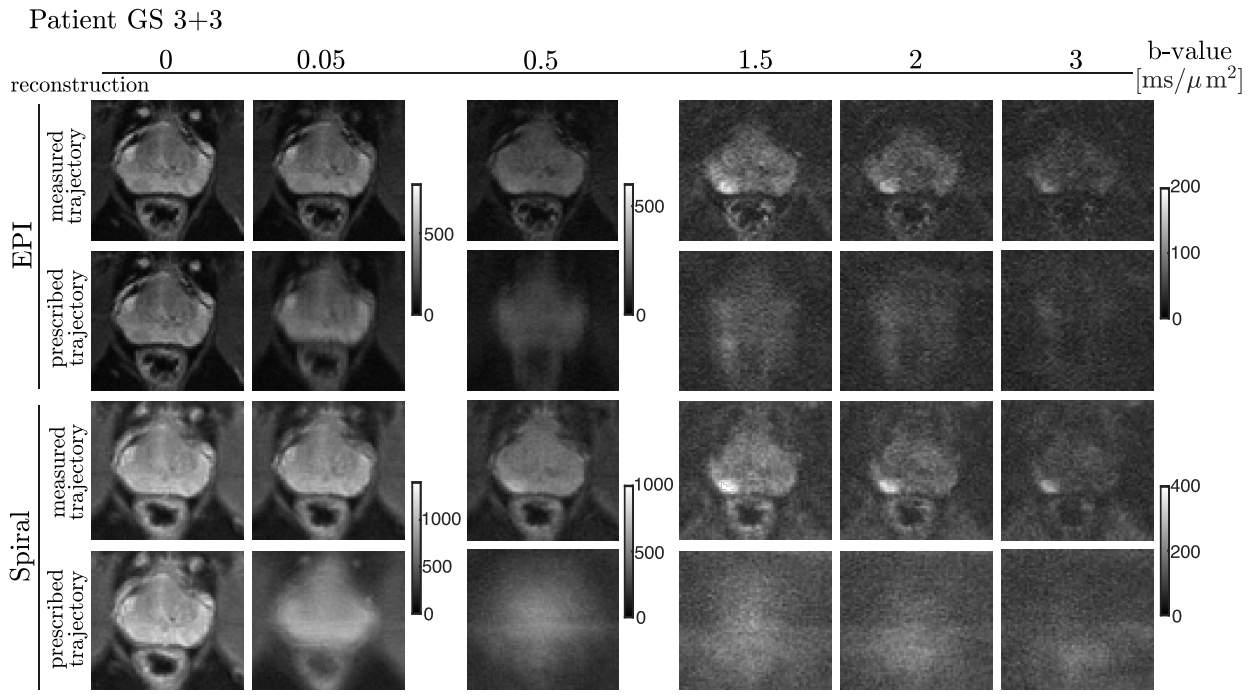

Figure 6.9: The diffusion direction-averaged signals of data from a PCa patient obtained with the expanded encoding reconstruction using measured field perturbations and nominal trajectories of EPI (*top*) and spiral (*bottom*).

full potential of spiral in terms of clinical application. The reported gain might be different in PCa patients.

6.3.5 In vivo data: Reconstruction with prescribed trajectory

Figure 6.9 shows direction-average signals of data from a PCa patient obtained with the expanded encoding reconstruction using measured field perturbations and nominal trajectories of EPI (*top*) and spiral (*bottom*) readouts. As expected, the b = 0 ms/μm^2 appear to have decent quality for both readouts with different reconstruction approaches. From lower to higher b-values, artefacts become increasingly visible; for EPI, the blurring is only in the phase encoding direction while for spiral readout blurring occurs in all directions. Significant improvement is achieved if field monitoring information is included during reconstruction.

6.3.6 dMRI image contrast evaluation in the prostate

The direction-averaged dMRI images for a healthy control (Figure 6.10) show enhanced tissue-to-background contrast across all b-values with spiral compared to EPI. For the latter, the signals from the chosen ROIs decay substantially at b-value $\sim$ 1.5 ms/μm^2, whereas for spiral, the noise floor is only approached at the highest b-value (3 ms/μm^2).

The conspicuity of cancerous lesions in a PCa patient (Figure 6.11) is improved in high b-value images (4$^{\text{th}}$ to 6$^{\text{th}}$ column) and signal values from an ROI drawn around the lesion are well above the noise floor at b = 3 ms/μm^2 only for dMRI with spiral readout.

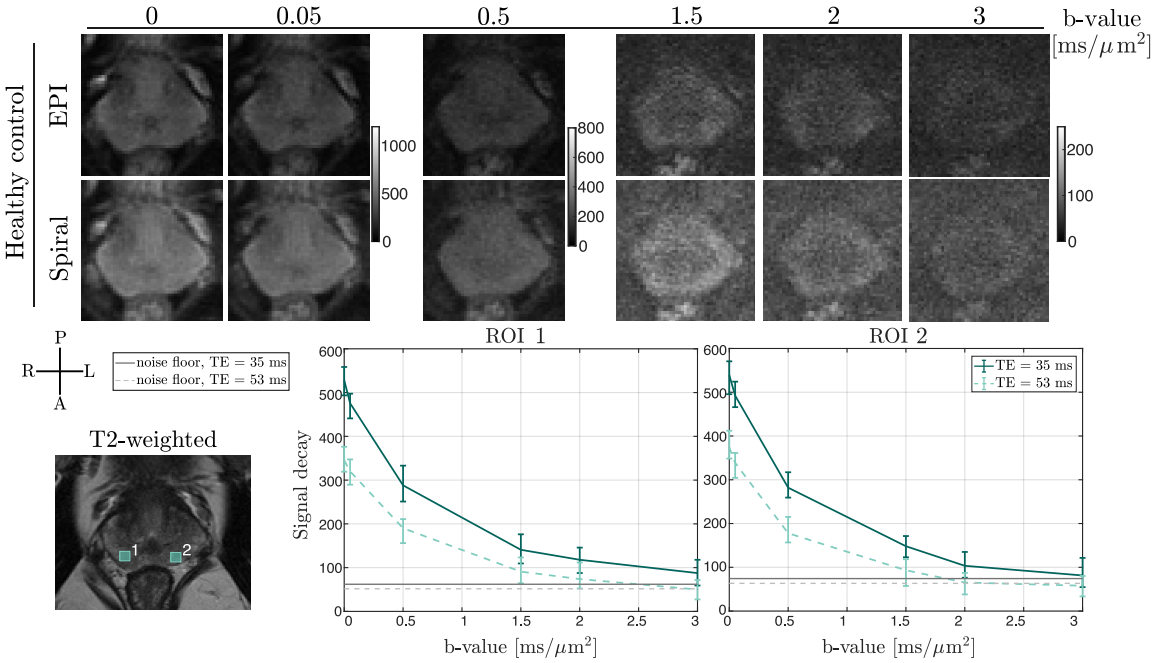

Figure 6.10: Representative example of a healthy control dataset. Diffusion direction-averaged signals for each b-value obtained with the prototype sequence using EPI at TE = 53 ms and spiral at TE = 35 ms (*top row*). Signal decays (median and interquartile range) from 2 ROIs (*bottom right*) drawn on high b-value images and depicted on the T2-weighted image (*bottom left*).

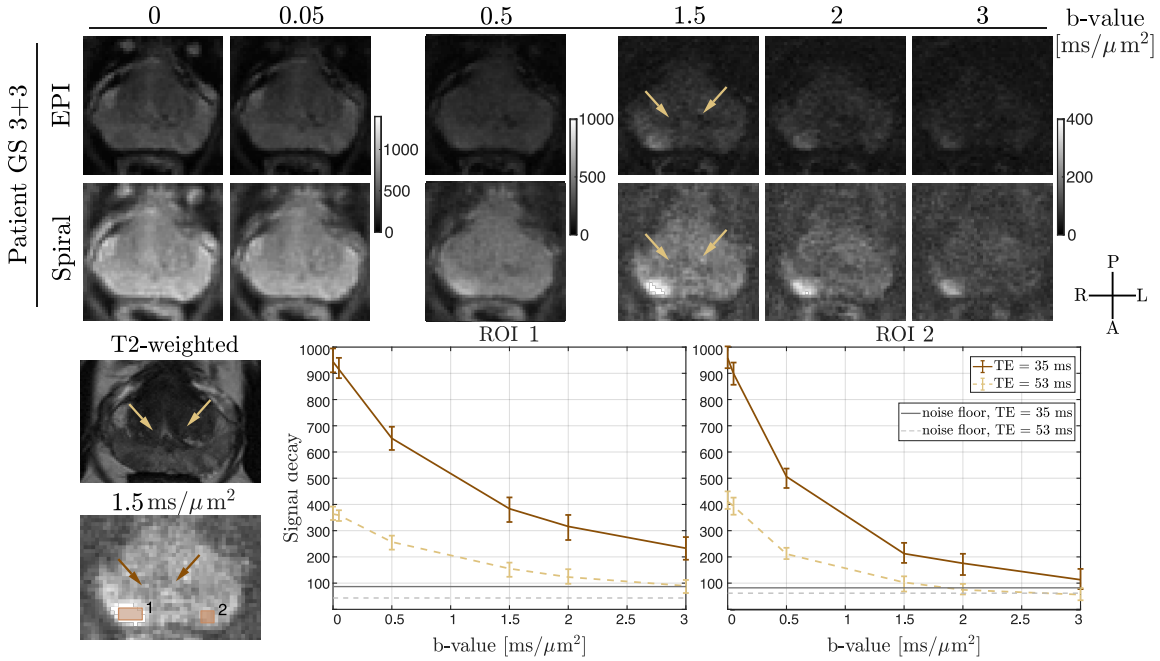

Figure 6.11: Representative example of a prostate cancer patient dataset. Diffusion direction-averaged signals of each b-value obtained with the prototype sequence using EPI at TE = 53 ms and spiral at TE = 35 ms (*top row*). Signal decay (median and interquartile range) from ROIs drawn in the cancer lesion (ROI 1, *bottom left*) and in healthy PZ (ROI 2, *bottom right*) drawn on high b-value images (PGSE spiral, bottom left). The T2-weighted image is shown for reference (*middle left*). The grey lines represent the estimated noise floor in each ROI. The arrows highlight anatomical features corresponding between T2-weighted and dMRI scans.

6.3.7 Quantitative MRI of the prostate

Quantitative maps obtained from DKI (Figure 6.12) show: i) fine anatomical details consistent with those observed in the T2-weighted image, ii) excellent conspicuity of the cancerous lesion (i.e., lower MD, higher MK and AK) in the right PZ regardless of the readout employed, iii) less noisy maps if estimated from the data acquired with spiral readout, and iv) ability to distinguish prostate zones (peripheral and transitional) (e.g., on MD and FA). The maps estimated from the dataset acquired and reconstructed with the vendor's software are more blurry, and therefore, the borders of the lesion and zones are less congruous. Despite being visually less affected by noise than images reconstructed with the expanded encoding model, the map's reliability might be lower due to distortions present in the data, e.g., EC and off-resonance effects, and therefore estimates might be inaccurate.

6.3.8 Prostate dMRI at high in-plane resolution

An overview of dMRI data acquired with high-resolution spiral trimmed to a range of different resolutions is shown in Figure 6.13. As expected, the images with higher resolution have visibly lower SNR across all sampled b-values. The decreased tissue to background contrast at high b-values for resolutions smaller than 1.33 mm is a result of ongoing T_2^* decay which leads to points

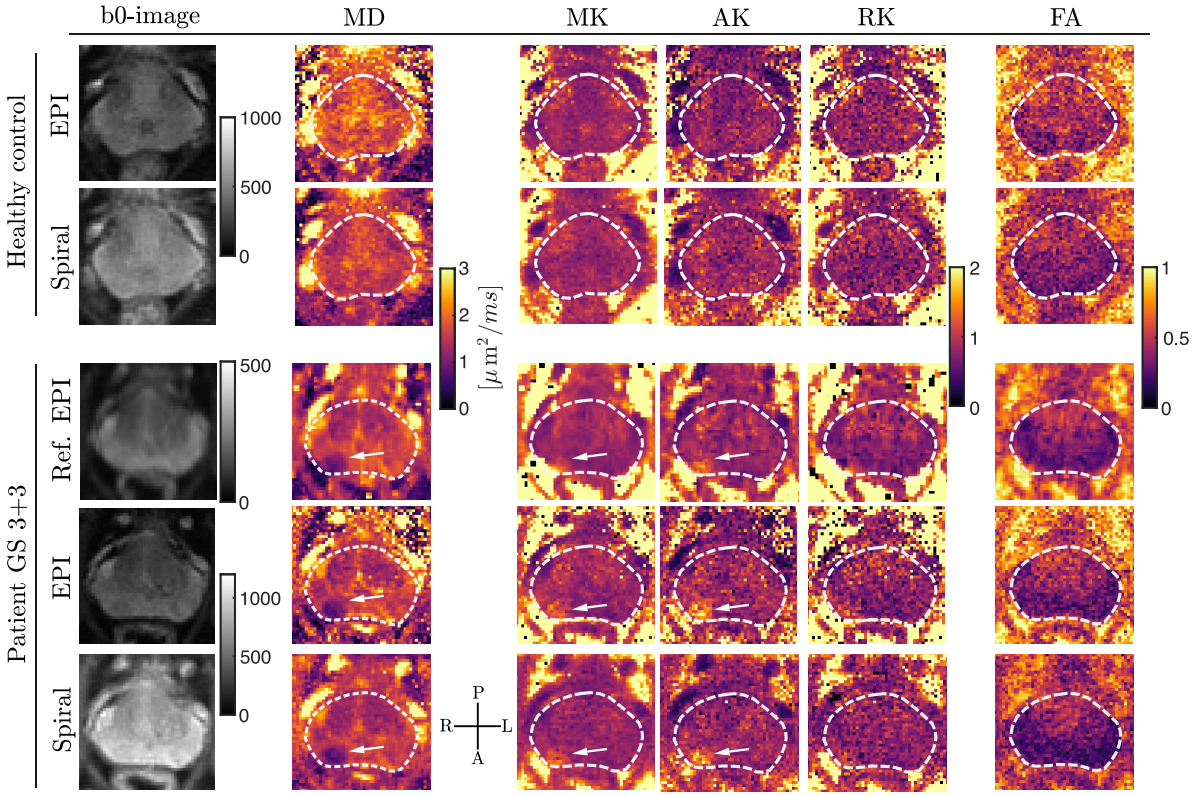

Figure 6.12: Quantitative maps from DKI estimated using data from a healthy control and PCa patient acquired using product PGSE (patient only) and prototype PGSE with EPI or spiral readouts (manually delineated gland edges are depicted with a dashed white line). The cancerous lesion (identified by the white arrows on selected maps where it is most recognisable) shows lower MD, and higher MK and AK.

sampled late within the readout train, i.e., farther out from the centre of k-space for a spiral-out, contributing an increasing amount of noise rather than signal to the image. Nevertheless, at the finest in-plane resolution (0.85 × 0.85 mm), the non-diffusion weighted image shows fine anatomical features preserved and at high b-value, the outline of the prostate gland is still noticeable despite noise amplification. For the comparison of the highest in-plane resolution data with the structural T2-weighted image please refer to Figure 6.10.

Figure 6.14 presents quantitative maps obtained from DKI for datasets shown in Figure 6.13. The MD and MK maps from the data at lower resolutions are blurrier and the zonal anatomy is difficult to outline, whereas maps from high-resolution dMRI data show greatly preserved zonal anatomy. Regarding the estimates, MD maps have similar spatial contrast (distribution of values) across different resolutions and are consistent with the values reported for the healthy prostate tissue in group studies [Sen et al., 2022]. However, in the MK maps one can observe increasing values for increasing resolutions.

The image quality comparison is shown in Figure 6.15. As expected, the SSIM decreases when the resolution decreases. SSIM maps present voxel-wise distributions of SSIM values with the lowest

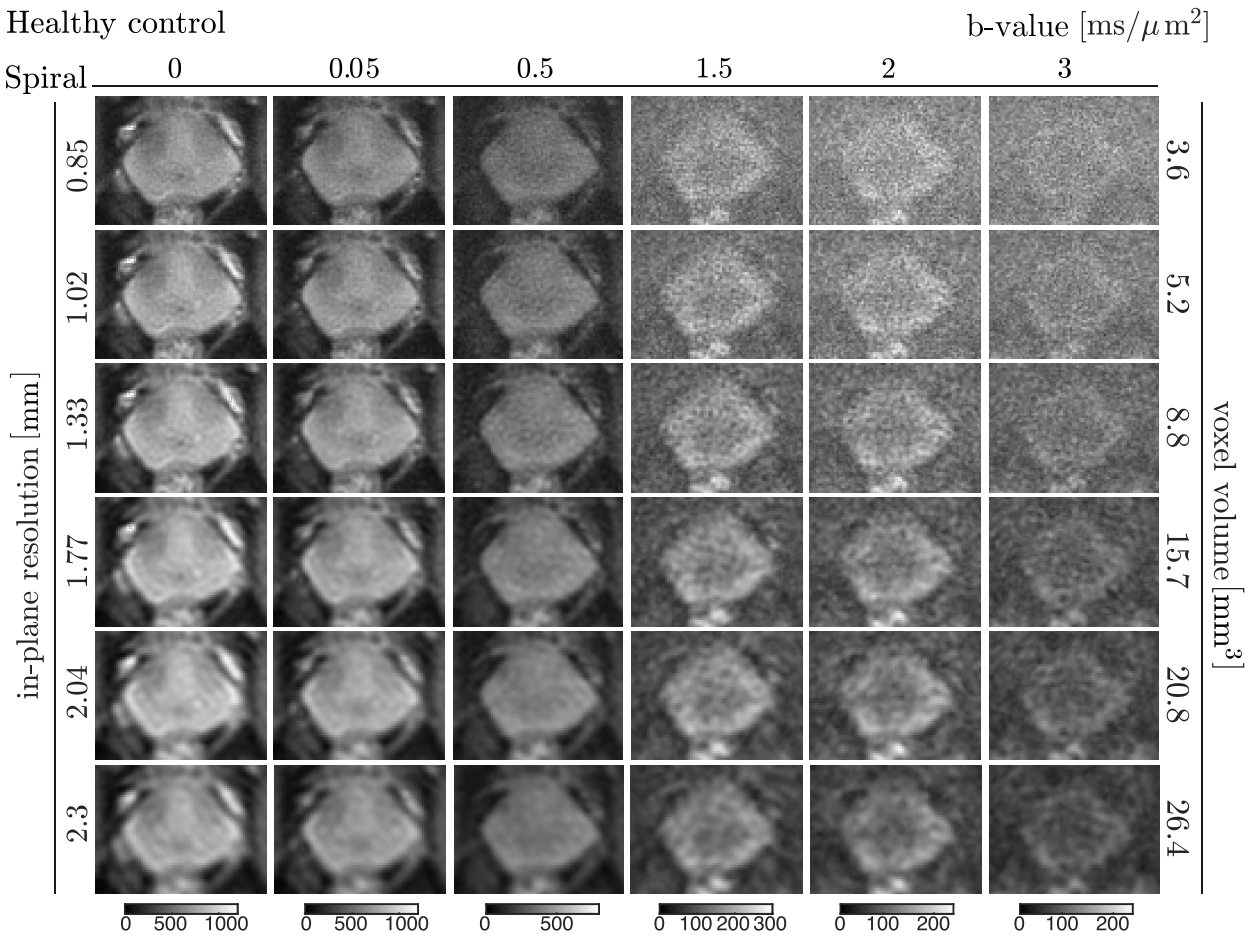

Figure 6.13: Overview of the diffusion direction-averaged signals of all b-values (*different columns*) obtained from a healthy control with the prototype sequence using a spiral readout and different resolutions (with corresponding voxel volumes reported). Please refer to Figure 6.10 for a comparison with the structural T2-weighted scan.

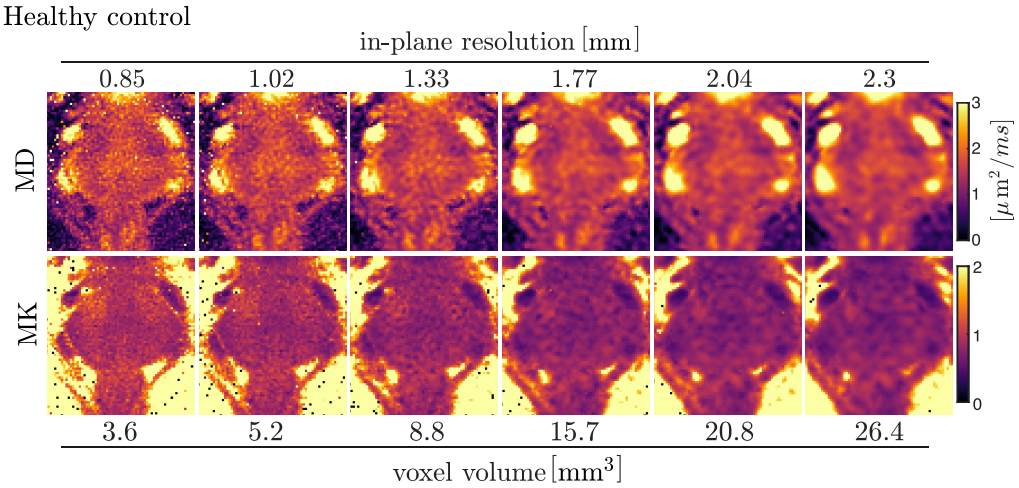

Figure 6.14: Quantitative maps from DKI (MD and MK) estimated using data acquired with high-resolution spiral reconstructed on a range of resolutions. The corresponding voxel volumes are reported.

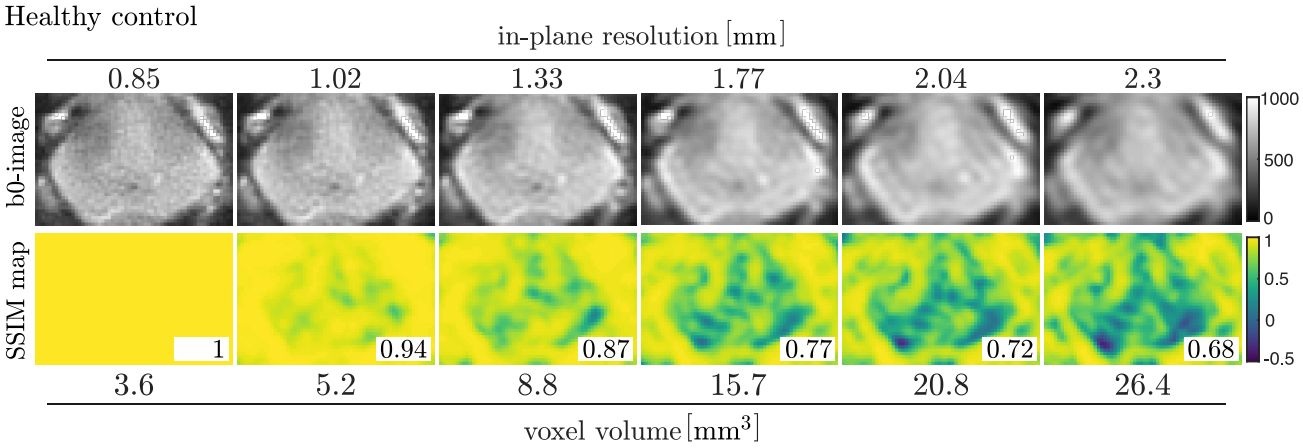

Figure 6.15: Comparison of structural similarities of the prostate across different images resolutions. Average b = 0 ms/μm^2 image (*top row*) and corresponding SSIM map are shown (*bottom row*). In bottom right corner of SSIM map, the global SSIM value for the image is reported with respect to the ground-truth at 0.85 × 0.85 mm in-plane resolution.

ones observed in the peripheral zone of the prostate for the biggest in-plane resolutions (2.04 and 2.33 mm). Moreover, SSIM maps highlight interesting areas in which structural information is being mostly lost, e.g., at the gland edges and the interface of zones.

6.4 Discussion

We successfully devised advanced field sensing and image reconstruction techniques for the prostate. Thereby, we achieved high dMRI quality even at high b-values exhibiting fine anatomical features. We deployed these methods for spiral readout, which provides shorter TEs and thus higher SNR [Lee et al., 2021b, Mueller et al., 2021].

6.4.1 EC correction in prostate dMRI with expanded encoding model

The results from phantom data (Figure 6.4) show that eddy current-induced distortions were evident in the data reconstructed with the vendor's programme, while effectively nulled in reconstructions using the expanded encoding model. The phantom experiment used the same protocol as the in vivo imaging, with the benefit of reduced motion (residual 'motion' could be coming from table vibrations) and smaller susceptibility differences compared to in vivo tissue; therefore, we carefully speculate that the observed high values in CoV maps for Ref. EPI can be mostly attributed to incompletely compensated eddy current effects. The directionally-dependent discrepancies of the vial boundaries were minimised with the expanded encoding model reconstruction, leading to very low CoV at the edges of the vials - even lower than with bipolar or eddy current nulled (ENCODE) gradients (Figure 2 in [Zhang et al., 2020]) - at no cost of complexity of the waveform design, no TE increase nor b-value penalty; however, with increased complexity of the reconstruction in the current set up.

Since EC originate purely from the MR hardware, and are gradient waveform design dependent, we expect to observe the same level of image discrepancies in vivo for the same diffusion sampling schemes. We did not specifically compare the EC induced distortions for in vivo prostate data in the same way as in the phantom experiment as it would be more challenging to interpret the results due to other confounding effects, e.g., surrounding tissue still contributing signal, whereas for the brain the signal decays away in the surrounding tissue. However, the results of improved image alignment presented in Figure 6.7 and the remaining distortions in diffusion-weighted volumes if reconstructed with the prescribed trajectory in Figure 6.9, support qualitative improvement of the data. Based on the analytical description of EC, one would expect to observe more prominent EC artefacts with increasing b-value; while the phantom experiment does clearly show this trend (Figure 6.4), the reconstruction of in vivo dMRI data with prescribed trajectories leads to more pronounced image distortions at higher b-values (Figure 6.9). This would need further investigation as short and long term eddy currents effects may be mixed and information on exact operations on k-space data by the vendor is not always available. If field monitoring with NMR probes is not possible, characterisation of those effects could be done in a repeated experiment as in [Jehenson et al., 1990].

6.4.2 Enhanced SNR of high b-value prostate dMRI

The expected SNR gain by shortening TE with a spiral readout rather than a partial-Fourier EPI would be 30% at $T_2 = 70$ ms as observed in the prostate tissue [Storås et al., 2008] (assuming monoexponential decay). This value is close to but lower than the observed SNR gain in b = 0 ms/μm^2 images seen in this study. For the remaining b-values, the SNR gains reached maximally 45% gain. The reported SNR gains could be attributed to a mixture of effects: significant difference in TE (spiral readout leads to 18 ms shorter TE than EPI) and fundamental properties of spiral readouts (more uniform readout time allocation and more spatially uniform g-factor maps [Lee et al., 2021b, Pruessmann et al., 2001, 1999]). In this study, we do not report g-factor maps since no fully sampled data were acquired and therefore SNR differences can not be reliably explained by differences in noise

penalty for parallel imaging with different readouts. Moreover, the readout duration and k-space coverage were matched across EPI and spiral readouts, and thus the T_2^* decay effects are not the same and therefore should be considered as factors contributing to the observed SNR difference.

The reported mean SNR gains of spiral over EPI are somewhat higher for low b-values (0.05-1.5 ms/μm^2) and lower for high b-values (2-3 ms/μm^2) than at b = 0 ms/μm^2. Regardless of the variability, one could expect approximately 35% SNR gain with spiral readout based on an estimate from b = 0 ms/μm^2 (Figure 6.8), since sequence differences relevant to SNR efficiency (i.e., readout trajectory, and g-factor) are equally at play with and without diffusion weighting. However, in the case of multicompartmental tissues with varying diffusion properties, like the prostate, this is subject to further evaluation. Thus, the reported SNR gains are valuable, especially at high b-value acquisition, since it is a key contrast to explore cellular restrictions occurring in prostate cancer. In our work, the SNR experiment was limited only to the healthy control dataset for the assessment of the SNR gain in healthy tissue. An equivalent experiment in prostate cancer would provide added insight into SNR gains as, in lesions there is more signal present.

6.4.3 Improved image quality and diffusion contrast

Undoubtedly, image quality of dMRI data was improved once reconstructed with the expanded encoding model. Our pilot Stejskal-Tanner PGSE experiment with spiral readout shows that the gain in diffusion contrast improved conspicuity of the GS 3+3 PCa lesion, the extent of which seems visually bigger on a spiral scan compared to EPI at high b-values. Ideally, this observation would require validation with excised tissue to precisely delineate the lesion volume. Improvements in the depiction of prostate tissue - as suggested by the high-resolution dMRI images with spiral readout - could help radiological evaluation of prostate anatomy [Medved et al., 2014, Nguyen et al., 2016].

6.4.4 Blurring in dMRI with spiral readouts

Comparing dMRI data across readouts, minor blurring (e.g., of fine structures anterior to the prostate) can be observed for acquisitions using spiral (Figure 6.11). The reason for this can be two-fold. dMRI with spiral readout is more prone to spatial dependent blurring due to changing phase and frequency encoding directions interacting with off-resonance differences caused by B_0 inhomogeneity, local susceptibility variations and chemical shift offsets. Therefore, we observe distortions (blurring) in all directions rather than distortions in one direction as in imaging with EPI readout which are less disturbing visually.

Secondly, the way B_0 maps are computed is that the raw B_0 maps are being thresholded and then extended, any holes are filled up and smoothed. Therefore, either a considerable amount of information has to be filled in or is lost during smoothing and a trade-off has to be made. So far, the expanded encoding model has been optimised for the brain, for which the B_0 field mapping is more straightforward. In abdominal imaging, there is wider diversity of tissue types, i.e., fat, muscles, bones, voids, that are interwoven over the imaging FOV. Therefore, the susceptibility can vary greatly over short distances in abdominal imaging and can be discernible in intra- and inter-subject

scans. Moreover, subject motion and peristalsis in the bowel will alter the field with respect to the initially acquired map. Ideally, one would do simultaneous estimation of the image and B_0 map, i.e., an update of B_0 for each shot would be exploited to robustify the reconstruction framework [Patzig et al., 2021, Sutton et al., 2004].

6.4.5 dMRI data at sub-millimetre in-plane resolution with high-resolution spiral readout

High-resolution dMRI with single shot EPI readout results in long TE and thus low SNR, which is further affected when high b-values are required. A combination of strong gradients and spiral readout schemes can drastically shorten TE. Our results demonstrate that obtaining sub-millimetre in-plane resolution with high b-value in a single shot acquisition is feasible.

Since spirals start k-space transversal at its centre, the minimum achievable TE is independent of the image resolution whereas it increases proportionally with the resolution for acquisitions with EPI readout. Therefore, the higher the resolution the larger the SNR advantage spirals provide over full-Fourier EPI. This gain is less prominent with partial-Fourier sampling, which - depending on the partial-Fourier factor - can bring down TE. Conversely, the advantage of spirals over EPI decreases once the resolution further increases, i.e., finer voxels; this is the effect of the ratio of time spent on sharp turns relative to the overall readout duration of EPI.

Based on the sequence simulations with the vendor's Ref. EPI, the achievable TE for high in-plane resolution partial-Fourier (= 6/8) single-shot EPI at 0.96 $\times$ 0.96 mm would be 80 ms. In this study, we did not acquire dMRI dataset with EPI at this resolution as the readout train would coincide with forbidden frequency bands based upon closer evaluation. Therefore, the bandwidth would have to be lowered, thus slowing down the timecourse of the trajectory globally, and increasing the readout time and TE further. With spiral readout, these constraints can be addressed on a per-trajectory-point basis, therefore maximising its sampling efficiency. The direct comparison of high-resolution spiral and EPI readouts would require a more complex optimisation as well as careful testing, and thus, was beyond the scope of this work.

6.4.6 Noise enhancement in dMRI data with high-resolution spiral

The same FOV and matrix size were used for reconstructions across different resolutions for high-resolution spiral readout to remove the pixelated appearance and need for dMRI data re-interpolation before numerical and visual comparisons. Thus, the improved quality of lower resolution images is a result of the application of zero filling, which smooths the image and reduces partial volume effects. As a result, higher resolution images may seem to be of inferior quality not only due to the noise amplification, which is a result of sampling points further out from the k-space centre that are mostly noise. Importantly, the investigation of signal decay curves from an ROI in the peripheral zone across resolutions (result not shown), confirmed significant signal increase for the finest resolutions at higher b-values. Therefore, we suspect that signal increase as a result of noise amplification at higher b-values leads to biased estimates of MK for the smallest voxel sizes. In

future work, we will employ recently proposed strategies of complex data denoising to remove noise from the data [Huynh et al., 2021] or account for noise bias in parameter estimation.

6.4.7 Study limitations

This study has several limitations. Firstly, it included data from a single healthy control and a single PCa patient and no statistical analysis of the differences (or improvements) could be performed. Therefore, to explore the full potential of strong gradients and spiral readouts with expanded encoding model reconstruction, the size of the study cohort should be increased. Nevertheless, the presented improved data quality with SNR gain for both standard and higher resolution imaging protocols should help improve PCa diagnosis, including low grade lesions that are challenging to image.

Secondly, our reconstruction framework relies on the measurement of field dynamics using an expensive commercial product in a separate session. As long as the acquisition protocol does not change, the same single measurement of field perturbations can be used across many in vivo scans. However, this approach has the drawback that the state of the MR system and field changes due to the volunteer in the scanner can be different between field camera and in vivo measurements, and therefore minor differences in monitored field perturbations, e.g., due to different thermal effects, may affect reconstruction performance. Concurrent field monitoring would address this problem, provided that a dedicated surface coil for abdominal imaging is constructed to enable such measurement as in the case for brain imaging [Wilm et al., 2015]. However, this would require placement of the probes around the abdomen constituting a larger area than the head, which extends out the bore on both ends. Therefore, the conditioning of the field computation would be challenging.

Thirdly, the B_0 field inhomogeneity can change over prolonged scan times due to subject and organ motion. Ideally, the B_0 field would be monitored dynamically during data acquisition and thus its variations could be incorporated in the reconstruction process. In our study, we assumed that the B_0 field mapped prior to EPI and spiral dMRI protocols (approximately 10-11 min overall) was correct. However, in cases of deviation from optimal field homogeneity over the scan time, e.g., as caused by changes in the susceptibility of the imaging object by varying content of gas in the rectum, it is likely that this assumption would not hold, leading to artefacts in the data.

Finally, in all dMRI protocols we used monopolar Stejskal-Tanner trapezoidal gradients, which are routinely employed in clinics. Since the prostate is a highly heterogenous gland, more advanced diffusion encoding could be employed to assess properties of multiple microscopic tissue compartments [Langbein et al., 2021, Nilsson et al., 2021] with characterisation of transverse relaxation properties at a wider range of echo times enabled by spiral readouts. Our study can form a solid foundation for advanced dMRI of the prostate at higher SNR, higher in-plane resolution and improved image quality.

6.5 Conclusions

The combination of strong gradients and spiral readouts unlocks sampling at short diffusion times and short TEs and can potentially lead to improved differentiation between low GS cancer and healthy tissue [Lemberskiy et al., 2017, Molendowska et al., 2022] and enable the accurate characterisation of short T_2 compartments (e.g., stroma) [Zhang et al., 2020]. Moreover, it addresses the current limitations of clinical diffusion imaging of the prostate. Clinical MRI can only be pushed up to moderate b-values (between 0.8-1.4 ms/μm^2 on more modern scanners) due to time constraints, as a high number of averages is required. The presented work could translate into higher b-value or sub-millimetre resolution without the need for averaging, or with a reduced number of averages.

Part III

Conclusions and Outlook

Chapter 7

Concluding remarks

This thesis showcases the use of an ultra-strong gradient system to image the human body below the neck, thus expanding the potential of ultra-strong gradient dMRI outside the brain. In particular, state-of-the-art hardware and image reconstruction techniques were exploited to tackle the challenge of obtaining increased sensitivity to microstructural difference in the prostate gland.

As a consequence of the limited gradient amplitude available on clinical systems, prostate dMRI typically relies on up to two acquisitions at distinct b-values smaller than 1 ms/μm^2, from which a high b-value image (e.g., at 1.4 ms/μm^2) is extrapolated assuming monoexponential signal decay. Such acquisitions limit the MR parameters available for diagnostic purposes to ADC maps whose poor microstructural specificity increases the likelihood of missing cancerous lesions. Thus, critical improvements to the sensitivity and specificity of dMRI measurements may be yielded upon leveraging the latest MR hardware advancements.

We first showed in **Chapter 4** that the Connectom scanner - capable of delivering 300 mT/m gradient amplitude - can be safely used for imaging landmarks below the neck (including the prostate). Physiological effects such as magnetophosphenes and PNS were assessed and found to be at most similar to those experienced in head imaging.

We then exploited the Connectom hardware in **Chapter 5** to measure dMRI signals over an extended range of b-values at shorter TEs than those found in the clinical setting, thereby enhancing SNR. Qualitative examination by a radiologist confirmed that the newly enabled contrasts are of diagnostic quality. The results from data acquired in a clinical cohort supported the hypothesis of increased diseased-to-healthy tissue contrast. However, the advantages of strong gradients used at high b-values could be diminished by prominent image distortions, e.g., by eddy currents, and thus limit the utility of the image for diagnostic purposes. Even though data-driven corrections in the image domain have been developed to tackle these detrimental effects, they usually require an increased number of acquisitions, leading to unreasonably long scan times.

To tackle this issue, we leveraged our own prototype MR sequence and product reconstruction server (Skope Technologies) in **Chapter 6** with field camera measurements to account for MR field perturbations. This, in turn, allowed us to acquire robust dMRI with spiral readouts, resulting in further echo time reduction. Successful deployment of advanced image reconstruction software with

monitoring of the MR field perturbations paved the way towards highly accurate prostate dMRI with minimised artefacts. Moreover, using high resolution spiral readout, we improved spatial resolution of the images capitalising on the fact that, for spiral readout that starts from the centre of k-space, the TE is independent of the image resolution.

To summarise, the deployed field monitoring relying on NMR sensors and the expanded encoding model for data reconstruction have jointly contributed to minimise artefacts in prostate dMRI, greatly improving data quality. The results from this dissertation will form the groundwork of future work dedicated to the design of new prostate dMRI experiments covering a much wider accessible parameter space, such as higher b-values, and improved sub-millimetre spatial resolutions. Such experiments will push quantitative dMRI of the prostate towards enhanced quality imaging with high microstructural accuracy and sensitivity.

Even though only four Connectom systems are operational worldwide, other advanced hardware systems have been proposed such as head-imaging dedicated systems, e.g., MAGNUS insert and Connectom 2.0. Recently, Siemens has introduced ultra-strong gradients in a commercial scanner called Cima.X capable of 200 mT/m gradient amplitude. Most importantly, this scanner also supports an open-source reconstruction framework (Open Recon) that enables more efficient data transfer from the scanner to the reconstruction unit (e.g., a product server such as Skope-i or an in-house reconstruction platform) and back to the scanner. The latest MR imaging system also offers improved shimming and duty cycle, allowing for the significant shortening of the time required for acquisition of multi-shell dMRI sequences. Importantly, Cima.X allows to run experiments without further restrictions from physiological monitors (PNS and cardiac watchdogs) in comparison to the currently used clinical MR machines.

In this initial work, reconstruction relies on the use of an expensive commercial product (i.e., the Skope field camera). Nonetheless, characterising the MR field using NMR probes is the gold-standard option and ensures the most reliable information about the MR system imperfections. While alternative less costly approaches, such as phantom-based methods relying on the scanner hardware directly, could be explored, they come at the cost of more tedious measurement procedures as those have to be performed multiple times with different parameters to obtain complete information. Nevertheless, regardless of the chosen method for collecting information about MR field properties, usually additional measurements are needed prior to data reconstruction.

From a clinical standpoint, the aforementioned advances are not yet ready to become part of clinical MR frameworks as they are currently too expensive and/or require too much additional scan time. Nevertheless, one can imagine the benefits they would bring if these limitations were alleviated in the future (please see **Chapter 8**, Future Directions). Determining the location of lesions could be made more accurate and precise, which is critical in radiotherapy treatment planning. Moreover, conspicuity of small lesions could be improved, especially in cases when information about those is lost due to artefacts originating from imperfections in the scanner hardware.

To conclude, even though the presented measurements rely on expensive hardware of limited

availability, we envision adoption of new hardware in the clinic in the next decades. This study provides first insights into what new information can be gleaned from new hardware and drive further development in the context of prostate cancer imaging. With better high-end MRI systems soon to be available worldwide, there will be opportunities to apply the results from this study and from any further research that this thesis has laid the groundwork for.

Chapter 8

Outlook

Contents

8.1 Future directions

Findings from this thesis provide a proof of the utility of the advanced dMRI using state-of-the-art MR hardware and reconstruction software in the prostate. As such, these results suggest a number of subsequent improvements.

As a part of our study, we explored the feasibility of high in-plane resolution spiral readout. However, the imaging slice thickness was quite big (5 mm), and thus, it remains as a shortfall in the dMRI protocols used in this study. In dMRI of the brain, super-resolution approaches have been proposed [Poot et al., 2013, Van Steenkiste et al., 2016, Vis et al., 2021]. Similar ideas could be explored to address this limitation in the prostate. Alternatively, reduced field-of-view imaging relying on RF design to excite only the inner volume of the tissue [Rieseberg et al., 2002] could be combined with a high in-plane resolution spiral. Fortunately, these solutions are available on newer MR system platforms as, e.g., ZOOMit^{PRO} (Siemens Healthineers). This would allow for even higher spatial resolution and significantly reduced measurement times.

Given the prominent role of diffusion contrast in clinical evaluation of prostate cancer, a future line of inquiry could investigate new microstructural MRI paradigms probing diffusion and T_2 in the same acquisition. This would provide a more complete picture of tissue and studies have shown promise in prostate albeit with non-optimised acquisition [Zhang et al., 2020]. Specifically, joint diffusion-T_2 experiments can better separate signal contributions from water trapped inside cells (including epithelium), extracellular/extravascular water (including lumen and stroma), and water in capillary blood [Palombo et al., 2020b]. Critically, previous studies suggest the existence of a short T_2 compartment that could reflect a difference in chemical composition between stroma and lumen [Storås et al., 2008] and characterising changes specific to stroma could potentially improve prediction of tumour agressiveness [Lawrence et al., 2020]. Unlocking shorter TEs by means of strong gradients and spiral readouts could help to access this previously-inaccessible measurement space. But this task is not as simple as mere collection of multitude of contrasts. Ideally one would like to maximse the amount of relevant information collected over the experiment time to minimise scan times and thus obtain a protocol that would be clinically feasible.

Finally, as an example of a future direction for research, that capitalises on all the work presented in earlier chapters, this chapter will close with a proof-of-concept of moving beyond traditional Stejskal-Tanner encoding to get more detailed characterisation of tissue microstructure in the prostate.

8.2 Towards comprehensive microstructure characterisation: B-tensor encoding with spiral readout

Introduction

In the field of microstructural MRI, b-tensor encoding has gained broad attention in recent years. Its main asset is the separability of the macro- and microscopic diffusion effects (Chapter 2, Section

2.5.2). In brief, the method relies on two pillars, namely, acquisition of diffusion contrasts at strong diffusion weighting and with encoding tensors of varying shapes. These measurements allow for exploration of non-Gaussian diffusion effects and separation of three main effects, namely microscopic diffusion anisotropy, isotropic heterogeneity, and orientation coherence.

Two research studies investigated the feasibility of b-tensor encoding in assessment of tissue heterogeneity of prostate cancer using clinical systems [Langbein et al., 2021, Nilsson et al., 2021]. The reported results demonstrated viability of the method in mapping macroscopic and microscopic heterogeneity of PCa. Importantly, the initial validation with histopathological data proves added value of new contrasts in characterisation of tissue properties undergoing changes in disease. However, ensuring high b-values, sufficient SNR of the data and high in-plane spatial resolution is a challenging task in itself due to hardware limitations of standard systems and long-established EPI readout employed in those studies.

In this proof of concept experiment, we build upon results in this thesis and our previous work [Mueller et al., 2021], and apply combined spiral readout with b-tensor encoding, capitalising on 300 mT/m gradient strength. The primary goal of this exploratory work is extend the dimension of diffusion encoding, and show high quality b-tensor encoded dMRI data enabled by better MR hardware, alternative readout trajectory and advanced reconstruction software. As a secondary objective, we want to address the limitations of the previous studies, i.e., large voxel sizes causing significant partial volume effects, and long echo times, which significantly reduce signal contributions from compartments with shorter T_2, the epithelium and stroma.

Methods

Study participants

One patient (age: 64 years, weight: 70 kg, height: 1.75 m) with confirmed prostatic adenocarcinoma: GS 3+3, two lesions - one in the PZ and one in the TZ, PSA level at 6.2 ng/ml at the age of the diagnosis in 2018, was scanned after providing written consent.

Data acquisition

The protocol was based on the experiment reported in Chapter 6, Section 6.2. Here, we repeat a few details briefly.

dMRI images were acquired on a 3T Connectom research-only scanner (Siemens Healthcare, Erlangen, Germany) using two surface coils.

Multi-echo GRE images were acquired for the estimation of static B_0 maps and receive coil sensitivities.

A prototype sequence with the flexibility of using arbitrary diffusion encodings and readouts was used to acquire dMRI images. The spiral readout used was as in Chapter 6, Section 8.2. dMRI images were acquired using user-defined free gradient waveforms [Sjölund et al., 2015] which were compensated for concomitant gradient effects [Szczepankiewicz et al., 2019]. Linear and spherical tensor encoding (LTE and STE, respectively), were not matched in their diffusion time

spectrum (Figure 8.1); the parameters for optimisation were: dephasing/rephasing gradient duration = 21.64 ms, pause time = 8.34 ms, Euclidean norm, with Maxwell-compensation but no first nor second gradient moment compensation. B-tensor acquisitions were performed along a set of non-collinear directions (n = [14, 8, 8, 10, 10, 10, 12, 12, 12]) distributed on a sphere at b = [0, 0.05, 0.2, 0.5, 0.8, 1.1, 1.5, 2, 3] ms/μm^2 ($G_{max} \approx 220$ mT/m, SR $<$ 60 T/m/s) and TE = 54.8 ms, TR = 3 s, in-plane resolution = 1.15 mm, slice thickness = 5 mm, and 18 slices without gap. The total scan time was 9 min and 50 s.

Structural MRI scans were acquired using a 2D T2-weighted TSE sequence in the axial plane (voxel size = 0.625 $\times$ 0.625 $\times$ 3 mm^3).

The magnetic field dynamics during the readout were monitored in separate experiment using a dynamic field-camera (Skope Magnetic Resonance Technologies) [Dietrich et al., 2016].

Data reconstruction

dMRI data were reconstructed using an expanded encoding model [Pruessmann et al., 2001, Wilm et al., 2011, 2015] including static B_0-inhomogeneities, coil sensitivities and the measured field dynamics [Bernstein et al., 1998, Vannesjo et al., 2016] using product reconstruction software (Skope-i, Skope Magnetic Resonance Technologies).

Data processing and analysis

dMRI images were denoised [Cordero-Grande et al., 2019], corrected for gradient nonlinearity induced distortions [Bammer et al., 2003, Jovicich et al., 2006], and powder-averaged [Arvidson, 1977,

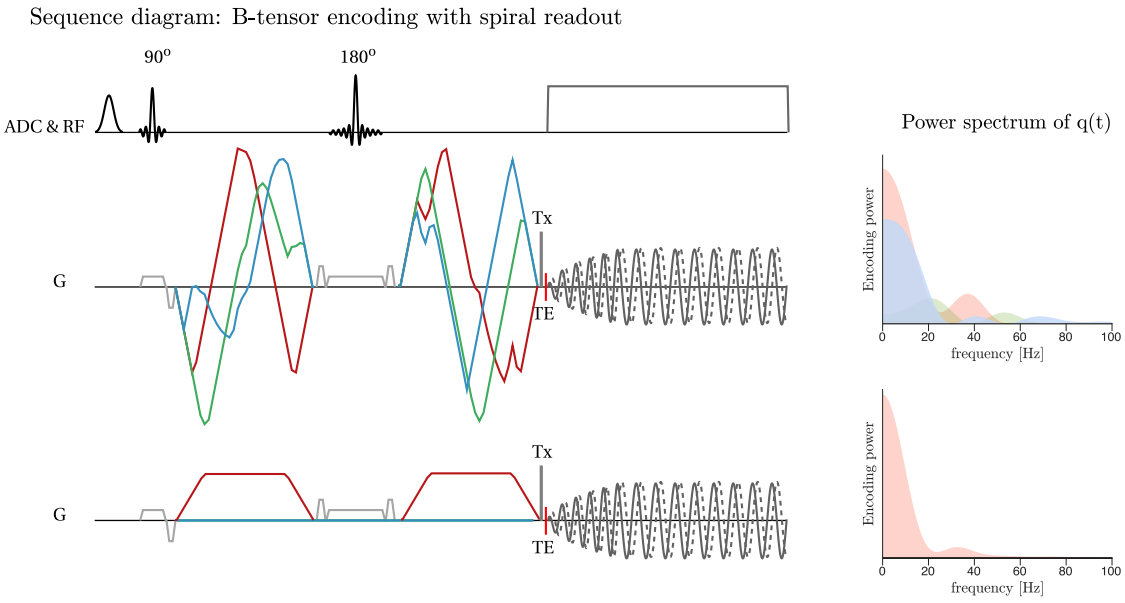

Figure 8.1: Prototype sequence with b-tensor encoding and spiral readout. Please note that diffusion gradients amplitudes are scaled to reflect differences in the maximum gradient amplitude used in the study for STE and LTE encodings. Importantly, gradient amplitudes of the spiral readout were also accordingly adjusted. Here, by G we denote G_x (X-axis), G_y (Y-axis) and G_z (Z-axis) gradients axes together.

Callaghan et al., 1979]. No smoothing nor motion correction was applied prior to further analysis.

We estimated features of the DTD. Using gamma distribution approximation [Lasič et al., 2014] (Chapter 2, Section 2.6.2), following maps were obtained: MD, MK_i, MK_a, and μFA. The analysis was performed using open-source software available at https://github.com/markus-nilsson/md-dmri (SHA-1 hash a57a2ee).

Results

The sequence diagram for STE and LTE encodings is shown in Figure 8.1 alongside with encoding power spectra of each shape of the b-tensor used in the protocol.

The data were evaluated and lesions were confirmed by the radiologist with 5 years of experience. Figure 8.2 shows dMRI images acquired at different b-values with LTE and STE. As expected, at

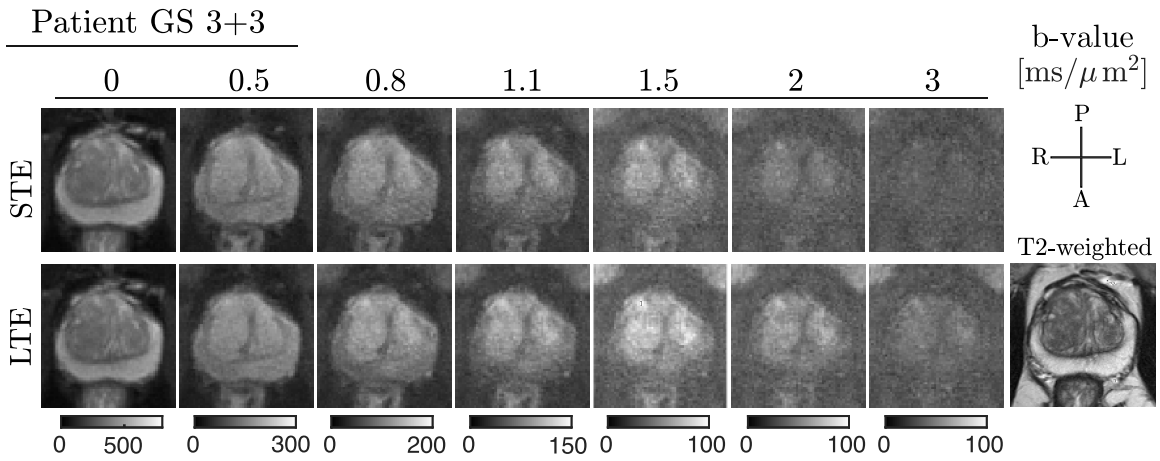

Figure 8.2: Overview of dMRI images acquired with LTE and STE - in rows - across wide range of b-values - in columns. For a comparison to an anatomical scan, a corresponding image slice of T2-weighted contrast is shown.

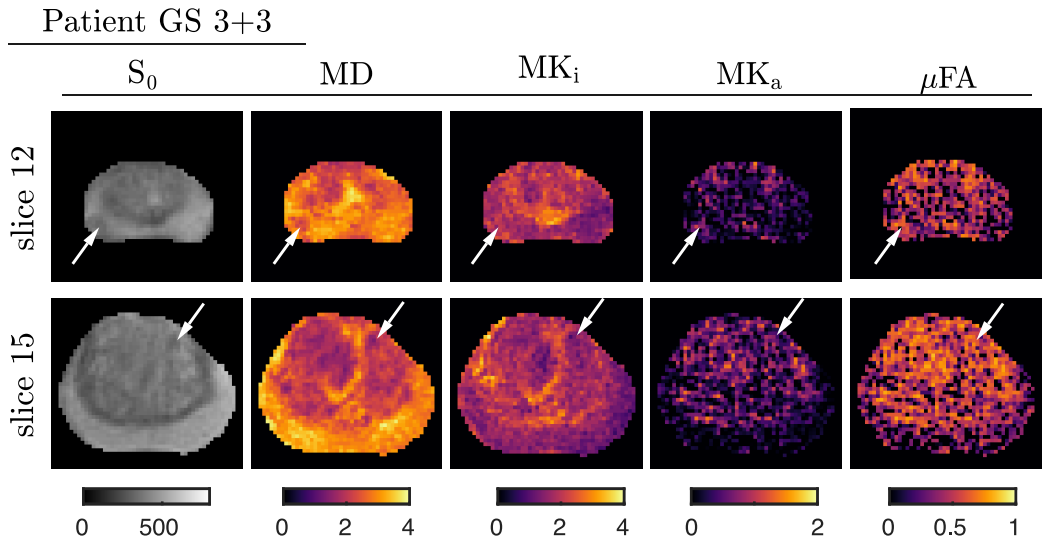

Figure 8.3: Overview of the parameter maps from fitting the DTD using gamma distribution approximation. The rows present results from two slices with suspected low-grade lesions. All the maps are unitless, except from MD, which is given in units of μm²/ms.

higher b-values, subtle differences across two b-tensor encodings are observed. Importantly, tissue edges on dMRI data are nicely preserved in comparison to the T2-weighted scan.

The data were jointly analysed to obtain parameters maps with excellent in-plane resolution as shown in Figure 8.3. Two of the maps are the most intense in the PZ (S_0 and MD), whereas the remaining ones (MK_i, MK_a, and μFA) are more intense in the TZ.

The PCa lesions are depicted with white arrows. Based on the clinical data, two lesions are identified: one in the right PZ in the apex, and second in the left TZ in the midgland. While the lesion in the PZ was straightforward to identify, the lesion in the TZ is more challenging to recognise. Nevertheless, as expected, in the lesions MD is lower than in the healthy tissue. MK_i, MK_a and μFA values are higher in the PZ lesion than in the other areas of the PZ (Figure 8.3, *top row*). Similar changes are observed in the lesions in the TZ (Figure 8.3, *bottom row*), however, opposite to observation in the PZ, those contrast less with the other healthy areas of the TZ.

Discussion and Conclusions

We demonstrate the feasibility of deriving microstructural measures, such as μFA, from free gradient waveform diffusion encodings with spiral readouts in the prostate using ultra-strong field gradients. The gain in TE and SNR that was recently demonstrated [Lee et al., 2021b] and, for our purposes, estimated in the prostate dMRI in PGSE experiment (Chapter 6), can be translated to free gradient waveforms. However, in this pilot experiment, we did not deploy high resolution spiral due to concerns regarding enhanced noise as reported in Chapter 6, Section 6.4.6.

The PZ showed lower values of MK_a than the TZ, suggesting that the TZ contains more elongated cells [Szczepankiewicz et al., 2016]. Therefore, the TZ can be interpreted as a region with considerable amount of stroma. Moreover, the cancerous lesion in the PZ shows higher values of both MK_i and MK_a with respect to surrounding healthy tissue. Those parameters could reflect undergoing changes in the epithelium, i.e., proliferation of cells having a wide range of diffusivities, and/or stroma, the presence of which increases microscopic kurtosis anisotropy (as also suggested by increased μFA). It is crucial to note that changes in stroma could also contribute to the heterogeneity in diffusion coefficients, i.e., increase MK_i.

The parameters maps from this proof of principle experiment align with the results reported in [Nilsson et al., 2021]. The estimated MD maps in both studies are higher than reported in the literature [Nezzo et al., 2016]. In our case, we hypothesise that this can be most likely attributed to the data analysis model. A separate analysis of low b-value LTE data using DTI representation corroborates this as it yields MD values 50% lower than with the gamma model. In addition, the estimated parameters maps depend on the TE. In our study, we obtained significantly lower TE (= 54.8 ms), which results in smaller attenuation of the signals from shorter T_2 compartments, the epithelium and stroma. Thus, the overall accuracy of the analysis model and the dependence of the MD, MK_i and MK_a on the TE should be further investigated as suggested in [Nilsson et al., 2021]. Lastly, in our work we address the issue with large voxel sizes which form a risk of conflating heterogenous diffusion on the microscopic scale with partial volume effects. In our datasets, higher in-plane resolution also benefits more accurate lesion delineation as confirmed by the radiologist.

Results from this pilot show that it is feasible to estimate DTD features and obtain plausible parameter maps at higher in-plane resolution, higher SNR and shorter TEs. Future studies will focus on a combination of b-tensor encoding with acquisitions at a range of different echo times to estimate accurately other properties of the different tissue components, such as volume fractions and T_2 values. In addition, those would also include correlative validation with histopathology as in [Langbein et al., 2021] as well as tailored diffusion encodings to explore effects of exchange and time dependence [Chakwizira et al., 2023, Wu et al., 2022]. This would validate the results obtained in previously-reported diffusion-relaxation correlation studies [Chatterjee et al., 2018, Zhang et al., 2020] and support deployment of new analysis frameworks relying on the bespoke multi-contrast prostate MRI protocols.

Appendix A

Supplementary Figures to Chapter 5

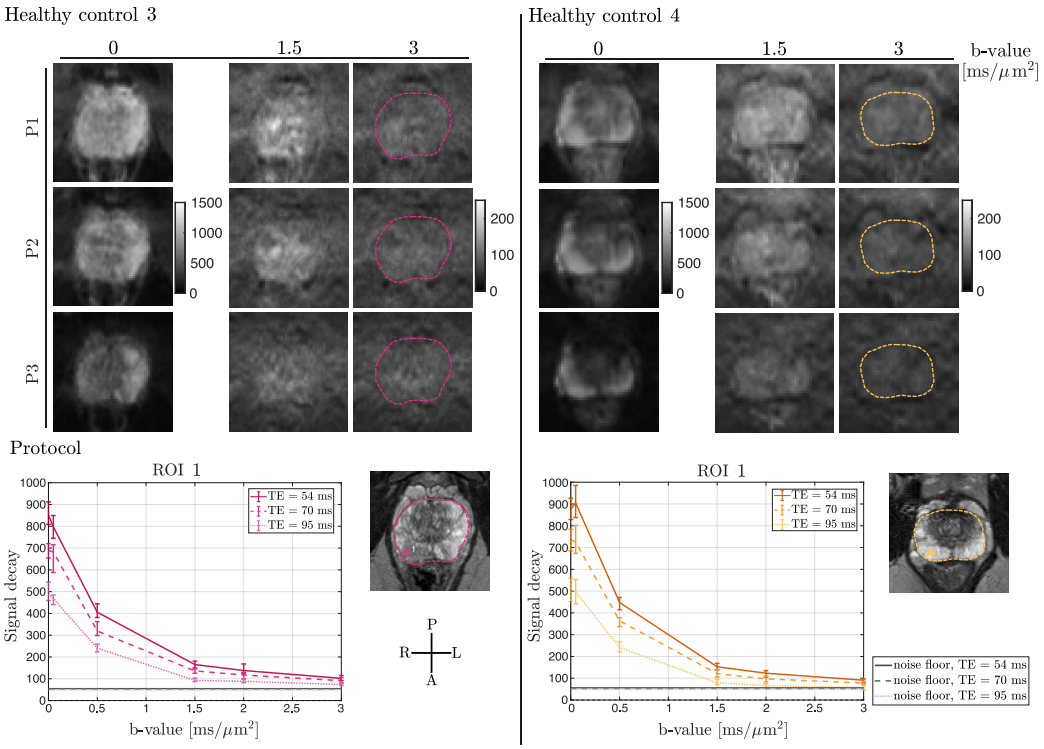

Figure A.1: Healthy control datasets. The direction-averaged diffusion signals of selected b-shell data: 300 mT/m (P1), 80 mT/m (P2) and 40 mT/m (P3) systems (*from top to bottom*) are presented. Based on the T2-weighted image (shown *bottom right* of each column), a prostate mask was drawn and overlaid on high b-value diffusion dataset. Signal decays (median with interquartile range) of the direction-averaged signals from ROIs drawn in the prostate gland (boxes depicted alongside 'ROI 1' plot) are shown. The gray lines represent the mean of the estimated noise floor in each ROI [Cordero-Grande et al., 2019]; in most cases, the lines from each ROI visually overlap.

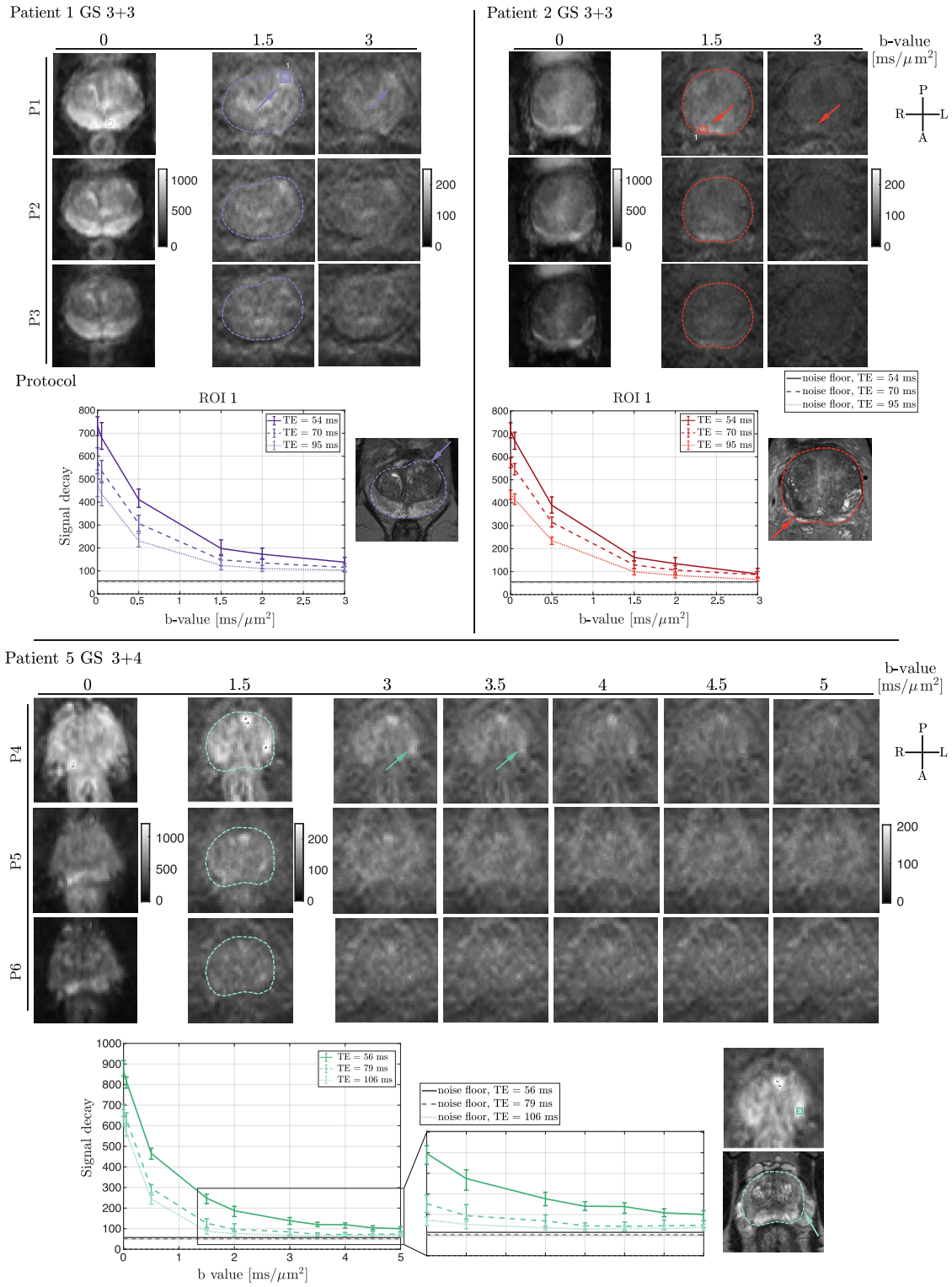

Figure A.2: Patient datasets (P1-P3 protocols - *top*, P4-P6 protocols with ultra-high b-value - *bottom*). The direction-averaged diffusion signals of selected b-shell data are presented for three patients. As in the case of healthy controls, a prostate mask was drawn on T2-weighted image and overlaid on high b-value diffusion dataset. Signal decays (median with interquartile range) of the direction-averaged signals from ROIs drawn in the cancerous lesions (boxes and arrows are depicting those lesions) are shown. The gray lines represent the mean of the estimated noise floor in each ROI [Cordero-Grande et al., 2019]; in most cases, the lines from each ROI visually overlap.

References

Abraham, N. E., Mendhiratta, N., and Taneja, S. S. (2015). Patterns of repeat prostate biopsy in contemporary clinical practice. *The Journal of urology*, 193(4):1178–1184.

Addy, N. O., Wu, H. H., and Nishimura, D. G. (2012). Simple method for MR gradient system characterization and k-space trajectory estimation. *Magnetic resonance in medicine*, 68(1):120–129.

Ahmed, H. U., Arya, M., Freeman, A., and Emberton, M. (2012). Do low-grade and low-volume prostate cancers bear the hallmarks of malignancy? *The Lancet oncology*, 13(11):e509–e517.

Ahmed, H. U., Bosaily, A. E.-S., Brown, L. C., Gabe, R., Kaplan, R., Parmar, M. K., Collaco-Moraes, Y., Ward, K., Hindley, R. G., Freeman, A., et al. (2017). Diagnostic accuracy of multi-parametric MRI and TRUS biopsy in prostate cancer (PROMIS): A paired validating confirmatory study. *The Lancet*, 389(10071):815–822.

Ahn, C., Kim, J., and Cho, Z. (1986). High-speed spiral-scan echo planar NMR imaging-I. *IEEE transactions on medical imaging*, 5(1):2–7.

Aldefeld, B. and Börnert, P. (1998). Effects of gradient anisotropy in MRI. *Magnetic resonance in medicine*, 39(4):606–614.

Alexander, A. L., Tsuruda, J. S., and Parker, D. L. (1997). Elimination of eddy current artifacts in diffusion-weighted echo-planar images: The use of bipolar gradients. *Magnetic Resonance in Medicine*, 38(6):1016–1021.

Alexander, D. C. (2008). A general framework for experiment design in diffusion MRI and its application in measuring direct tissue-microstructure features. *Magnetic Resonance in Medicine: An Official Journal of the International Society for Magnetic Resonance in Medicine*, 60(2):439–448.

Aliotta, E., Moulin, K., and Ennis, D. B. (2018). Eddy current–nulled convex optimized diffusion encoding (EN-CODE) for distortion-free diffusion tensor imaging with short echo times. *Magnetic resonance in medicine*, 79(2):663–672.

Andersson, J. L., Skare, S., and Ashburner, J. (2003). How to correct susceptibility distortions in spin-echo echo-planar images: Application to diffusion tensor imaging. *Neuroimage*, 20(2):870–888.

Andersson, J. L. and Sotiropoulos, S. N. (2016). An integrated approach to correction for off-resonance effects and subject movement in diffusion MR imaging. *Neuroimage*, 125:1063–1078.

Arvidson, C. (1977). Translational diffusion in model membranes studied by nuclear magnetic resonance. *International Journal of Quantum Chemistry*, 12(2):153_158.

Assaf, Y. and Cohen, Y. (1998). Non-mono-exponential attenuation of water andn-acetyl aspartate signals due to diffusion in brain tissue. *Journal of Magnetic Resonance*, 131(1):69–85.

Bammer, R., Markl, M., Barnett, A., Acar, B., Alley, M., Pelc, N., Glover, G., and Moseley, M. (2003). Analysis and generalized correction of the effect of spatial gradient field distortions in diffusion-weighted imaging. *Magnetic Resonance in Medicine: An Official Journal of the International Society for Magnetic Resonance in Medicine*, 50(3):560–569.

Barlow, H. B., Kohn, H. I., and Walsh, E. G. (1947). Visual sensations aroused by magnetic fields. *American Journal of Physiology-Legacy Content*, 148(2):372–375.

Barmet, C., Zanche, N. D., and Pruessmann, K. P. (2008). Spatiotemporal magnetic field monitoring for MR. *Magnetic Resonance in Medicine: An Official Journal of the International Society for Magnetic Resonance in Medicine*, 60(1):187–197.

Baron, C., Lebel, R., Wilman, A., and Beaulieu, C. (2012). The effect of concomitant gradient fields on diffusion tensor imaging. *Magnetic resonance in medicine*, 68(4):1190–1201.

Basser, P. J., Mattiello, J., and LeBihan, D. (1994). MR diffusion tensor spectroscopy and imaging. *Biophysical journal*, 66(1):259–267.

Baur, A. D., Hansen, C. M., Rogasch, J., Posch, H., Elezkurtaj, S., Maxeiner, A., Erb-Eigner, K., and Makowski, M. R. (2020). Evaluation of T1 relaxation time in prostate cancer and benign prostate tissue using a Modified Look-Locker inversion recovery sequence. *Scientific Reports*, 10(1):1–8.

Beaton, L., Bandula, S., Gaze, M. N., and Sharma, R. A. (2019). How rapid advances in imaging are defining the future of precision radiation oncology. *British journal of cancer*, 120(8):779–790.

Beaulieu, C. and Allen, P. S. (1994). Determinants of anisotropic water diffusion in nerves. *Magnetic resonance in medicine*, 31(4):394–400.

Bennett, H., Roberts, M., Doi, S., and Gardiner, R. (2016). The global burden of major infectious complications following prostate biopsy. *Epidemiology & Infection*, 144(8):1784–1791.

Bernstein, M. A., King, K. F., and Zhou, X. J. (2004). *Handbook of MRI pulse sequences*. Elsevier.

Bernstein, M. A., Zhou, X. J., Polzin, J. A., King, K. F., Ganin, A., Pelc, N. J., and Glover, G. H. (1998). Concomitant gradient terms in phase contrast MR: Analysis and correction. *Magnetic resonance in medicine*, 39(2):300–308.

Bloch, F. (1946). Nuclear induction. *Physical review*, 70(7-8):460.

Boesch, C., Gruetter, R., and Martin, E. (1991). Temporal and spatial analysis of fields generated by eddy currents in superconducting magnets: Optimization of corrections and quantitative characterization of magnet/gradient systems. *Magnetic resonance in medicine*, 20(2):268–284.

Boorjian, S. A., Karnes, R. J., Rangel, L. J., Bergstralh, E. J., and Blute, M. L. (2008). Mayo Clinic validation of the D'amico risk group classification for predicting survival following radical prostatectomy. *The Journal of urology*, 179(4):1354–1361.

Borofsky, S., George, A. K., Gaur, S., Bernardo, M., Greer, M. D., Mertan, F. V., Taffel, M., Moreno, V., Merino, M. J., Wood, B. J., et al. (2018). What are we missing? False-negative cancers at multiparametric MR imaging of the prostate. *Radiology*, 286(1):186.

Boss, M. A., Chenevert, T. L., Waterton, J. C., Morris, D. M., Ragheb, H., Jackson, A., deSouza, N., Collins, D. J., van Beers, B. E., Garteiser, P., et al. (2014). Temperature-controlled isotropic diffusion phantom with wide range of apparent diffusion coefficients for multicenter assessment of scanner repeatability and reproducibility. *Proc 22nd Int Soc Magnet Reson Med*, 4505.

Bourland, J., Nyenhuis, J., Mouchawar, G., Elabbady, T., Geddes, L., Schaefer, D., and Riehl, M. (1991). Physiologic indicators of high MRI gradient-induced fields.

Bratan, F., Melodelima, C., Souchon, R., Hoang Dinh, A., Mège-Lechevallier, F., Crouzet, S., Colombel, M., Gelet, A., and Rouvière, O. (2015). How accurate is multiparametric MR imaging in evaluation of prostate cancer volume? *Radiology*, 275(1):144–154.

Brindley, G. (1955). The site of electrical excitation of the human eye. *The Journal of physiology*, 127(1):189–200.

Brindley, G. S. and Lewin, W. S. (1968). The sensations produced by electrical stimulation of the visual cortex. *The Journal of physiology*, 196(2):479–493.

Brodsky, E. K., Klaers, J. L., Samsonov, A. A., Kijowski, R., and Block, W. F. (2013). Rapid measurement and correction of phase errors from B0 eddy currents: Impact on image quality for non-cartesian imaging. *Magnetic resonance in medicine*, 69(2):509–515.

Brown, R. (1828). XXVII. A brief account of microscopical observations made in the months of June, July and August 1827, on the particles contained in the pollen of plants; and on the general existence of active molecules in organic and inorganic bodies. *The philosophical magazine*, 4(21):161–173.

Brown, T. R., Kincaid, B., and Ugurbil, K. (1982). NMR chemical shift imaging in three dimensions. *Proceedings of the National Academy of Sciences*, 79(11):3523–3526.

Callaghan, P., Jolley, K., and Lelievre, J. (1979). Diffusion of water in the endosperm tissue of wheat grains as studied by pulsed field gradient nuclear magnetic resonance. *Biophysical journal*, 28(1):133–141.

Caverly, T. J., Hayward, R. A., Reamer, E., Zikmund-Fisher, B. J., Connochie, D., Heisler, M., and Fagerlin, A. (2016). Presentation of benefits and harms in US cancer screening and prevention guidelines: Systematic review. *JNCI: Journal of the National Cancer Institute*, 108(6).

Cercignani, M. and Alexander, D. C. (2006). Optimal acquisition schemes for in vivo quantitative magnetization transfer MRI. *Magnetic Resonance in Medicine: An Official Journal of the International Society for Magnetic Resonance in Medicine*, 56(4):803–810.

Chakwizira, A., Westin, C.-F., Brabec, J., Lasič, S., Knutsson, L., Szczepankiewicz, F., and Nilsson, M. (2023). Diffusion MRI with pulsed and free gradient waveforms: Effects of restricted diffusion and exchange. *NMR in Biomedicine*, 36(1):e4827.

Chatterjee, A., Antic, T., Gallan, A. J., Paner, G. P., Lin, L. I.-K., Karczmar, G. S., and Oto, A. (2022a). Histological validation of prostate tissue composition measurement using hybrid multidimensional MRI: Agreement with pathologists' measures. *Abdominal Radiology*, 47(2):801–813.

Chatterjee, A., Bourne, R. M., Wang, S., Devaraj, A., Gallan, A. J., Antic, T., Karczmar, G. S., and Oto, A. (2018). Diagnosis of prostate cancer with noninvasive estimation of prostate tissue composition by using hybrid multidimensional MR imaging: A feasibility study. *Radiology*, 287(3):864.

Chatterjee, A., Mercado, C., Bourne, R. M., Yousuf, A., Hess, B., Antic, T., Eggener, S., Oto, A., and Karczmar, G. S. (2022b). Validation of prostate tissue composition by using hybrid multidimensional MRI: Correlation with histologic findings. *Radiology*, 302(2):368–377.

Chatterjee, A., Thomas, S., and Oto, A. (2020). Prostate MR: Pitfalls and benign lesions. *Abdominal Radiology*, 45(7):2154–2164.

Chatterjee, A., Watson, G., Myint, E., Sved, P., McEntee, M., and Bourne, R. (2015). Changes in epithelium, stroma, and lumen space correlate more strongly with Gleason pattern and are stronger predictors of prostate ADC changes than cellularity metrics. *Radiology*, 277(3):751–762.

Chu, K. C. and Rutt, B. K. (1995). MR gradient coil heat dissipation. *Magnetic resonance in medicine*, 34(1):125–132.

Clayton, D. B., Elliott, M. A., Leigh, J. S., and Lenkinski, R. E. (2001). 1H spectroscopy without solvent suppression: Characterization of signal modulations at short echo times. *Journal of magnetic resonance*, 153(2):203–209.

Cleveland, G., Chang, D., Hazlewood, C., and Rorschach, H. (1976). Nuclear magnetic resonance measurement of skeletal muscle: Anisotrophy of the diffusion coefficient of the intracellular water. *Biophysical journal*, 16(9):1043–1053.

Cordero-Grande, L., Christiaens, D., Hutter, J., Price, A. N., and Hajnal, J. V. (2019). Complex diffusion-weighted image estimation via matrix recovery under general noise models. *Neuroimage*, 200:391–404.

Davids, M., Guérin, B., Klein, V., and Wald, L. L. (2020). Optimization of MRI gradient coils with explicit peripheral nerve stimulation constraints. *IEEE transactions on medical imaging*, 40(1):129–142.

Davids, M., Guérin, B., vom Endt, A., Schad, L. R., and Wald, L. L. (2019). Prediction of peripheral nerve stimulation thresholds of MRI gradient coils using coupled electromagnetic and neurodynamic simulations. *Magnetic resonance in medicine*, 81(1):686–701.

De Zanche, N., Barmet, C., Nordmeyer-Massner, J. A., and Pruessmann, K. P. (2008). Nmr probes for measuring magnetic fields and field dynamics in MR systems. *Magnetic Resonance in Medicine: An Official Journal of the International Society for Magnetic Resonance in Medicine*, 60(1):176–186.

Deshmane, A., Gulani, V., Griswold, M. A., and Seiberlich, N. (2012). Parallel MR imaging. *Journal of Magnetic Resonance Imaging*, 36(1):55–72.

Desouza, N., Riches, S., Vanas, N., Morgan, V., Ashley, S., Fisher, C., Payne, G., and Parker, C. (2008). Diffusion-weighted magnetic resonance imaging: A potential non-invasive marker of tumour aggressiveness in localized prostate cancer. *Clinical radiology*, 63(7):774–782.

DeSouza, N., Winfield, J., Waterton, J. C., Weller, A., Papoutsaki, M.-V., Doran, S., Collins, D., Fournier, L., Sullivan, D., Chenevert, T., et al. (2018). Implementing diffusion-weighted MRI for body imaging in prospective multicentre trials: Current considerations and future perspectives. *European radiology*, 28(3):1118–1131.

Dietrich, B. E., Brunner, D. O., Wilm, B. J., Barmet, C., Gross, S., Kasper, L., Haeberlin, M., Schmid, T., Vannesjo, S. J., and Pruessmann, K. P. (2016). A field camera for MR sequence monitoring and system analysis. *Magnetic resonance in medicine*, 75(4):1831–1840.

Doty, F. D. (1998). MRI gradient coil optimization. *Spatially Resolved Magnetic Resonance: Methods, Materials, Medicine, Biology, Rheology, Geology, Ecology, Hardware*, pages 647–674.

Duyn, J. H., Yang, Y., Frank, J. A., and van der Veen, J. W. (1998). Simple correction method for k-space trajectory deviations in MRI. *Journal of Magnetic Resonance*, 132(1):150–153.

Edelstein, W. A., Hedeen, R. A., Mallozzi, R. P., El-Hamamsy, S.-A., Ackermann, R. A., and Havens, T. J. (2002). Making MRI quieter. *Magnetic Resonance Imaging*, 20(2):155–163.

Eichner, C., Cauley, S. F., Cohen-Adad, J., Möller, H. E., Turner, R., Setsompop, K., and Wald, L. L. (2015). Real diffusion-weighted MRI enabling true signal averaging and increased diffusion contrast. *NeuroImage*, 122:373–384.

Einstein, A. (1905). Über die von der molekularkinetischen Theorie der wärme geforderte Bewegung von in ruhenden Flüssigkeiten suspendierten Teilchen. *Annalen der physik*, 4.

Engels, R. R., Israël, B., Padhani, A. R., and Barentsz, J. O. (2020). Multiparametric magnetic resonance imaging for the detection of clinically significant prostate cancer: What urologists need to know. Part 1: Acquisition. *European urology*, 77(4):457–468.

Epstein, J. I., Egevad, L., Amin, M. B., Delahunt, B., Srigley, J. R., and Humphrey, P. A. (2016). The 2014 International Society of Urological Pathology (ISUP) consensus conference on Gleason grading of prostatic carcinoma. *The American journal of surgical pathology*, 40(2):244–252.

Eriksson, S., Lasic, S., and Topgaard, D. (2013). Isotropic diffusion weighting in PGSE NMR by magic-angle spinning of the q-vector. *Journal of Magnetic Resonance*, 226:13–18.

Fan, Q., Eichner, C., Afzali, M., Mueller, L., Tax, C. M., Davids, M., Mahmutovic, M., Keil, B., Bilgic, B., Setsompop, K., et al. (2022). Mapping the human connectome using diffusion MRI at 300 mT/m gradient strength: Methodological advances and scientific impact. *NeuroImage*, 254:118958.

Foerster, B. U., Tomasi, D., and Caparelli, E. C. (2005). Magnetic field shift due to mechanical vibration in functional magnetic resonance imaging. *Magnetic Resonance in Medicine: An Official Journal of the International Society for Magnetic Resonance in Medicine*, 54(5):1261–1267.

Foo, T. K., Laskaris, E., Vermilyea, M., Xu, M., Thompson, P., Conte, G., Van Epps, C., Immer, C., Lee, S.-K., Tan, E. T., et al. (2018). Lightweight, compact, and high-performance 3 T MR system for imaging the brain and extremities. *Magnetic resonance in medicine*, 80(5):2232–2245.

Foo, T. K., Tan, E. T., Vermilyea, M. E., Hua, Y., Fiveland, E. W., Piel, J. E., Park, K., Ricci, J., Thompson, P. S., Graziani, D., et al. (2020). Highly efficient head-only magnetic field insert gradient coil for achieving simultaneous high gradient amplitude and slew rate at 3.0T (MAGNUS) for brain microstructure imaging. *Magnetic resonance in medicine*, 83(6):2356–2369.

Fourier, J. (1822). Theorie analytique de la chaleur, chez firmindidot, Paris.

Frankenhaeuser, B. and Huxley, A. (1964). The action potential in the myelinated nerve fibre of Xenopus laevis as computed on the basis of voltage clamp data. *The Journal of Physiology*, 171(2):302–315.

Freschi, F., Lopez, H. S., Smith, E., Tang, F., Repetto, M., and Crozier, S. (2016). Mixed-dimensional elements in transient thermal analysis of gradient coils. *Numerical Heat Transfer, Part A: Applications*, 69(3):265–282.

Friebe, B., Wollrab, A., Thormann, M., Fischbach, K., Ricke, J., Grueschow, M., Kropf, S., Fischbach, F., and Speck, O. (2015). Sensory perceptions of individuals exposed to the static field of a 7T MRI: A controlled blinded study. *Journal of Magnetic Resonance Imaging*, 41(6):1675–1681.

Frisken, B. J. (2001). Revisiting the method of cumulants for the analysis of dynamic light-scattering data. *Applied optics*, 40(24):4087–4091.

Genc, S., Tax, C. M., Raven, E. P., Chamberland, M., Parker, G. D., and Jones, D. K. (2020). Impact of b-value on estimates of apparent fibre density. *Human Brain Mapping*.

Giganti, F., Allen, C., Emberton, M., Moore, C. M., Kasivisvanathan, V., Group, P. S., et al. (2020). Prostate imaging quality (PI-QUAL): A new quality control scoring system for multiparametric magnetic resonance imaging of the prostate from the PRECISION trial. *European urology oncology*, 3(5):615–619.

Giganti, F., Kirkham, A., Kasivisvanathan, V., Papoutsaki, M.-V., Punwani, S., Emberton, M., Moore, C. M., and Allen, C. (2021). Understanding PI-QUAL for prostate MRI quality: A practical primer for radiologists. *Insights Into Imaging*, 12(1):1–19.

Gleason, D. F. (1966). Classification of prostatic carcinomas. *Cancer Chemother. Rep.*, 50:125–128.

Glover, G. H. (2012). Spiral imaging in fMRI. *Neuroimage*, 62(2):706–712.

Griswold, M. A., Jakob, P. M., Heidemann, R. M., Nittka, M., Jellus, V., Wang, J., Kiefer, B., and Haase, A. (2002). Generalized autocalibrating partially parallel acquisitions (GRAPPA). *Magnetic Resonance in Medicine: An Official Journal of the International Society for Magnetic Resonance in Medicine*, 47(6):1202–1210.

Gruetter, R. and Boesch, C. (1992). Fast, noniterative shimming of spatially localized signals. In vivo analysis of the magnetic field along axes. *Journal of Magnetic Resonance (1969)*, 96(2):323–334.

Grüsser, O.-J. and Hagner, M. (1990). On the history of deformation phosphenes and the idea of internal light generated in the eye for the purpose of vision. In *History of Ophthalmology*, pages 57–85. Springer.

Gudbjartsson, H. and Patz, S. (1995). The rician distribution of noisy MRI data. *Magnetic resonance in medicine*, 34(6):910–914.

Guo, A. C., Cummings, T. J., Dash, R. C., and Provenzale, J. M. (2002). Lymphomas and high-grade astrocytomas: Comparison of water diffusibility and histologic characteristics. *Radiology*, 224(1):177–183.

Guo, F., De Luca, A., Parker, G., Jones, D. K., Viergever, M. A., Leemans, A., and Tax, C. M. (2021). The effect of gradient nonlinearities on fiber orientation estimates from spherical

deconvolution of diffusion magnetic resonance imaging data. *Human Brain Mapping*, 42(2):367–383.

Hahn, E. L. (1950). Spin echoes. *Physical review*, 80(4):580.

Ham, C., Engels, J., Van de Wiel, G., and Machielsen, A. (1997). Peripheral nerve stimulation during MRI: Effects of high gradient amplitudes and switching rates. *Journal of Magnetic Resonance Imaging*, 7(5):933–937.

Harvey, P. R. (1999). The modular (twin) gradient coil—high resolution, high contrast, diffusion weighted EPI at 1.0 Tesla. *Magnetic Resonance Materials in Physics, Biology and Medicine*, 8(1):43–47.

Harvey, P. R. and Mansfield, P. (1994). Avoiding peripheral nerve stimulation: Gradient waveform criteria for optimum resolution in echo-planar imaging. *Magnetic resonance in medicine*, 32(2):236–241.

Haselgrove, J. C. and Moore, J. R. (1996). Correction for distortion of echo-planar images used to calculate the apparent diffusion coefficient. *Magnetic Resonance in Medicine*, 36(6):960–964.

Hebrank, F. X., Gebhardt, M., et al. (2000). SAFE model—a new method for predicting peripheral nerve stimulation in MRI. In *Proc Intl Soc Mag Res Med*, volume 8, page 2007.

Hedeen, R. A. and Edelstein, W. A. (1997). Characterization and prediction of gradient acoustic noise in MR imagers. *Magnetic Resonance in Medicine*, 37(1):7–10.

Heid, O. (1997). Robust EPI phase correction. *Proceedings of the ISMRM, Vancouver*.

Hennel, F., Girard, F., and Loenneker, T. (1999). "Silent" MRI with soft gradient pulses. *Magnetic Resonance in Medicine: An Official Journal of the International Society for Magnetic Resonance in Medicine*, 42(1):6–10.

Hodgkin, A. L. and Huxley, A. F. (1952). A quantitative description of membrane current and its application to conduction and excitation in nerve. *The Journal of Physiology*, 117(4):500–544.

Huang, S. Y., Tian, Q., Fan, Q., Witzel, T., Wichtmann, B., McNab, J. A., Bireley, J. D., Machado, N., Klawiter, E. C., Mekkaoui, C., et al. (2019). High-gradient diffusion MRI reveals distinct estimates of axon diameter index within different white matter tracts in the in vivo human brain. *Brain Structure and Function*, pages 1–15.

Huang, S. Y., Witzel, T., Keil, B., Scholz, A., Davids, M., Dietz, P., Rummert, E., Ramb, R., Kirsch, J. E., Yendiki, A., et al. (2021). Connectome 2.0: Developing the next-generation ultra-high gradient strength human MRI scanner for bridging studies of the micro-, meso-and macro-connectome. *NeuroImage*, 243:118530.

Huynh, K. M., Chang, W.-T., Chung, S. H., Chen, Y., Lee, Y., and Yap, P.-T. (2021). Noise mapping and removal in complex-valued multi-channel MRI via optimal shrinkage of singular values. In *International Conference on Medical Image Computing and Computer-Assisted Intervention*, pages 191–200. Springer.

IEC 60601-2-33, . (2015). Medical electrical equipment—part 2-33: Particular requirements for the basic safety and essential performance of magnetic resonance equipment for medical diagnosis.

International Commission on Non-Ionizing Radiation Protection et al. (2010). Guidelines for limiting exposure to time-varying electric and magnetic fields (1 Hz to 100 kHz). *Health physics*, 99(6):818–836.

Irfanoglu, M. O., Walker, L., Sarlls, J., Marenco, S., and Pierpaoli, C. (2012). Effects of image distortions originating from susceptibility variations and concomitant fields on diffusion MRI tractography results. *Neuroimage*, 61(1):275–288.

Irnich, W. and Hebrank, F. X. (2009). Stimulation threshold comparison of time-varying magnetic pulses with different waveforms. *Journal of Magnetic Resonance Imaging: An Official Journal of the International Society for Magnetic Resonance in Medicine*, 29(1):229–236.

Irwin, D., Rush, S., Evering, R., Lepeschkin, E., Montgomery, D., and Weggel, R. (1970). Stimulation of cardiac muscle by a time-varying magnetic field. *IEEE Transactions on Magnetics*, 6(2):321–322.

Jehenson, P., Westphal, M., and Schuff, N. (1990). Analytical method for the compensation of eddy-current effects induced by pulsed magnetic field gradients in NMR systems. *Journal of Magnetic Resonance (1969)*, 90(2):264–278.

Jelescu, I. O., Veraart, J., Fieremans, E., and Novikov, D. S. (2016). Degeneracy in model parameter estimation for multi-compartmental diffusion in neuronal tissue. *NMR in Biomedicine*, 29(1):33–47.

Jezzard, P. and Balaban, R. S. (1995). Correction for geometric distortion in echo planar images from B0 field variations. *Magnetic resonance in medicine*, 34(1):65–73.

Jiang, X., Li, H., Xie, J., McKinley, E. T., Zhao, P., Gore, J. C., and Xu, J. (2017). In vivo imaging of cancer cell size and cellularity using temporal diffusion spectroscopy. *Magnetic resonance in medicine*, 78(1):156–164.

Jiang, X., Li, H., Xie, J., Zhao, P., Gore, J. C., and Xu, J. (2016). Quantification of cell size using temporal diffusion spectroscopy. *Magnetic resonance in medicine*, 75(3):1076–1085.

Johnson, D. C., Raman, S. S., Mirak, S. A., Kwan, L., Bajgiran, A. M., Hsu, W., Maehara, C. K., Ahuja, P., Faiena, I., Pooli, A., et al. (2019). Detection of individual prostate cancer foci via multiparametric magnetic resonance imaging. *European urology*, 75(5):712–720.

Johnston, E. W., Bonet-Carne, E., Ferizi, U., Yvernault, B., Pye, H., Patel, D., Clemente, J., Piga, W., Heavey, S., Sidhu, H. S., et al. (2019). VERDICT MRI for prostate cancer: Intracellular volume fraction versus apparent diffusion coefficient. *Radiology*, 291(2):391–397.

Jones, D. K. (2004). The effect of gradient sampling schemes on measures derived from diffusion tensor MRI: A Monte Carlo study. *Magnetic Resonance in Medicine: An Official Journal of the International Society for Magnetic Resonance in Medicine*, 51(4):807–815.

Jones, D. K., Alexander, D. C., Bowtell, R., Cercignani, M., Dell'Acqua, F., McHugh, D. J., Miller, K. L., Palombo, M., Parker, G. J., Rudrapatna, U., et al. (2018). Microstructural imaging of the human brain with a 'super-scanner': 10 key advantages of ultra-strong gradients for diffusion MRI. *NeuroImage*, 182:8–38.

Jones, D. K. and Basser, P. J. (2004). "Squashing peanuts and smashing pumpkins": How noise distorts diffusion-weighted MR data. *Magnetic Resonance in Medicine: An Official Journal of the International Society for Magnetic Resonance in Medicine*, 52(5):979–993.

Jovicich, J., Czanner, S., Greve, D., Haley, E., van Der Kouwe, A., Gollub, R., Kennedy, D., Schmitt, F., Brown, G., MacFall, J., et al. (2006). Reliability in multi-site structural MRI studies: Effects of gradient non-linearity correction on phantom and human data. *Neuroimage*, 30(2):436–443.

Kale, S. C., Chen, X. J., and Henkelman, R. M. (2009). Trading off SNR and resolution in MR images. *NMR in Biomedicine: An International Journal Devoted to the Development and Application of Magnetic Resonance In vivo*, 22(5):488–494.

Kale, S. C., Lerch, J. P., Henkelman, R. M., and Chen, X. J. (2008). Optimization of the SNR-resolution tradeoff for registration of magnetic resonance images. *Human brain mapping*, 29(10):1147–1158.

Kangarlu, A., Baudendistel, K., Heverhagen, J., and Knopp, M. (2004). Clinical high-and ultrahigh-field MR and its interaction with biological systems. *Der Radiologe*, 44(1):19.

Kasper, L., Bollmann, S., Vannesjo, S. J., Gross, S., Haeberlin, M., Dietrich, B. E., and Pruessmann, K. P. (2015). Monitoring, analysis, and correction of magnetic field fluctuations in echo planar imaging time series. *Magnetic resonance in medicine*, 74(2):396–409.

Keenan, K. E., Ainslie, M., Barker, A. J., Boss, M. A., Cecil, K. M., Charles, C., Chenevert, T. L., Clarke, L., Evelhoch, J. L., Finn, P., et al. (2018). Quantitative magnetic resonance imaging phantoms: A review and the need for a system phantom. *Magnetic resonance in medicine*, 79(1):48–61.

Kessels, P. (1996). Understanding mechanical vibrations in MRI scanners. *DCT rapporten*, 1996.

Kimmlingen, R. (2017). Pioneers of Connectome Gradients. *Magnetom FLASH*, 68(2):122–136.

Kiselev, V. G. (2010). The cumulant expansion: An overarching mathematical framework for understanding diffusion NMR. *Diffusion MRI*, pages 152–168.

Kleban, E., Tax, C. M., Rudrapatna, U. S., Jones, D. K., and Bowtell, R. (2020). Strong diffusion gradients allow the separation of intra-and extra-axonal gradient-echo signals in the human brain. *NeuroImage*, page 116793.

Klein, V., Davids, M., Schad, L. R., Wald, L. L., and Guérin, B. (2021). Investigating cardiac stimulation limits of MRI gradient coils using electromagnetic and electrophysiological simulations in human and canine body models. *Magnetic resonance in medicine*, 85(2):1047–1061.

Koay, C. G., Özarslan, E., and Pierpaoli, C. (2009). Probabilistic identification and estimation of noise (PIESNO): A self-consistent approach and its applications in MRI. *Journal of magnetic resonance*, 199(1):94–103.

Koch, M. and Norris, D. G. (2000). An assessment of eddy current sensitivity and correction in single-shot diffusion-weighted imaging. *Physics in Medicine & Biology*, 45(12):3821.

Koppel, D. E. (1972). Analysis of macromolecular polydispersity in intensity correlation spectroscopy: The method of cumulants. *The Journal of Chemical Physics*, 57(11):4814–4820.

Kweldam, C., van Leenders, G., and van der Kwast, T. (2019). Grading of prostate cancer: A work in progress. *Histopathology*, 74(1):146–160.

Kyriazi, S., Blackledge, M., Collins, D. J., and Desouza, N. M. (2010). Optimising diffusion-weighted imaging in the abdomen and pelvis: Comparison of image quality between monopolar and bipolar single-shot spin-echo echo-planar sequences. *European radiology*, 20(10):2422–2431.

Lampinen, B., Szczepankiewicz, F., Mårtensson, J., van Westen, D., Hansson, O., Westin, C.-F., and Nilsson, M. (2020). Towards unconstrained compartment modeling in white matter using diffusion-relaxation MRI with tensor-valued diffusion encoding. *Magnetic resonance in medicine*, 84(3):1605–1623.

Langbein, B. J., Szczepankiewicz, F., Westin, C.-F., Bay, C., Maier, S. E., Kibel, A. S., Tempany, C. M., and Fennessy, F. M. (2021). A pilot study of multidimensional diffusion MRI for assessment of tissue heterogeneity in prostate cancer. *Investigative radiology*, 56(12):845–853.

Langer, D. L., van der Kwast, T. H., Evans, A. J., Sun, L., Yaffe, M. J., Trachtenberg, J., and Haider, M. A. (2008). Intermixed normal tissue within prostate cancer: Effect on MR imaging measurements of apparent diffusion coefficient and T2—sparse versus dense cancers. *Radiology*, 249(3):900–908.

Lasič, S., Szczepankiewicz, F., Eriksson, S., Nilsson, M., and Topgaard, D. (2014). Microanisotropy imaging: Quantification of microscopic diffusion anisotropy and orientational order parameter by diffusion MRI with magic-angle spinning of the q-vector. *Frontiers in Physics*, 2:11.

Latour, L. L., Svoboda, K., Mitra, P. P., and Sotak, C. H. (1994). Time-dependent diffusion of water in a biological model system. *Proceedings of the National Academy of Sciences*, 91(4):1229–1233.

Lawrence, M. G., Pidsley, R., Niranjan, B., Papargiris, M., Pereira, B. A., Richards, M., Teng, L., Norden, S., Ryan, A., Frydenberg, M., et al. (2020). Alterations in the methylome of the stromal tumour microenvironment signal the presence and severity of prostate cancer. *Clinical Epigenetics*, 12(1):1–18.

Le Bihan, D., Breton, E., Lallemand, D., Grenier, P., Cabanis, E., and Laval-Jeantet, M. (1986). MR imaging of intravoxel incoherent motions: Application to diffusion and perfusion in neurologic disorders. *Radiology*, 161(2):401–407.

Lee, C. H. (2019). Quantitative T2-mapping using MRI for detection of prostate malignancy: A systematic review of the literature. *Acta Radiologica*, 60(9):1181–1189.

Lee, H.-H., Novikov, D. S., and Fieremans, E. (2021a). Removal of partial Fourier-induced Gibbs (RPG) ringing artifacts in MRI. *Magnetic Resonance in Medicine*, 86(5):2733–2750.

Lee, M. S., Moon, M. H., Kim, Y. A., Sung, C. K., Woo, H., Jeong, H., and Son, H. (2018). Is Prostate Imaging Reporting and Data System Version 2 sufficiently discovering clinically significant prostate cancer? Per-lesion radiology-pathology correlation study. *American Journal of Roentgenology*, 211(1):114–120.

Lee, Y., Wilm, B. J., Brunner, D. O., Gross, S., Schmid, T., Nagy, Z., and Pruessmann, K. P. (2021b). On the signal-to-noise ratio benefit of spiral acquisition in diffusion MRI. *Magnetic resonance in medicine*, 85(4):1924–1937.

Lemberskiy, G., Fieremans, E., Veraart, J., Deng, F.-M., Rosenkrantz, A. B., and Novikov, D. S. (2018). Characterization of prostate microstructure using water diffusion and NMR relaxation. *Frontiers in physics*, 6:91.

Lemberskiy, G., Rosenkrantz, A. B., Veraart, J., Taneja, S. S., Novikov, D. S., and Fieremans, E. (2017). Time-dependent diffusion in prostate cancer. *Investigative radiology*, 52(7):405–411.

Li, W., Mechefske, C., Gazdzinski, C., and Rutt, B. (2004). Acoustic noise analysis and prediction in a 4-T MRI scanner. *Concepts in Magnetic Resonance Part B: Magnetic Resonance Engineering: An Educational Journal*, 21(1):19–25.

Likes, R. S. (1981). Moving gradient zeugmatography. Technical report.

Ljunggren, S. (1983). Imaging methods. *Journal of magnetic resonance*, 54:338–343.

Lövsund, P., Öberg, P., Nilsson, S., and Reuter, T. (1980). Magnetophosphenes: A quantitative analysis of thresholds. *Medical and Biological Engineering and Computing*, 18(3):326–334.

Lu, H., Jensen, J. H., Ramani, A., and Helpern, J. A. (2006). Three-dimensional characterization of non-gaussian water diffusion in humans using diffusion kurtosis imaging. *NMR in Biomedicine: An International Journal Devoted to the Development and Application of Magnetic Resonance In vivo*, 19(2):236–247.

Lundell, H. and Lasič, S. (2020). Diffusion encoding with general gradient waveforms. *Advanced Diffusion Encoding Methods in MRI*, 24:12.

Lustig, M., Kim, S.-J., and Pauly, J. M. (2008). A fast method for designing time-optimal gradient waveforms for arbitrary k-space trajectories. *IEEE transactions on medical imaging*, 27(6):866–873.

Magi-Galluzzi, C., Montironi, R., and Epstein, J. I. (2016). Contemporary Gleason grading and novel Grade Groups in clinical practice. *Current opinion in urology*, 26(5):488–492.

Mansfield, P., Glover, P. M., and Beaumont, J. (1998). Sound generation in gradient coil structures for MRI. *Magnetic resonance in medicine*, 39(4):539–550.

Mansfield, P. and Harvey, P. (1993). Limits to neural stimulation in echo-planar imaging. *Magnetic resonance in medicine*, 29(6):746–758.

Marg, E. (1991). Magnetostimulation of vision: Direct noninvasive stimulation of the retina and the visual brain. *Optometry and vision science: official publication of the American Academy of Optometry*, 68(6):427–440.

Mattiello, J., Basser, P. J., and Le Bihan, D. (1997). The b-matrix in diffusion tensor echo-planar imaging. *Magnetic Resonance in Medicine*, 37(2):292–300.

McCurdy, C. M., Louka, A. M., Handler, W. B., and Chronik, B. A. (2020). Magneto-phosphenes in head-only gradient coils. *Society Mag. Res. Medicine, Proceedings of the 29th Annual Meeting. Paris: Soc Mag Res in Medicine*.

McNab, J. A., Edlow, B. L., Witzel, T., Huang, S. Y., Bhat, H., Heberlein, K., Feiweier, T., Liu, K., Keil, B., Cohen-Adad, J., et al. (2013). The Human Connectome Project and beyond: Initial applications of 300 mT/m gradients. *Neuroimage*, 80:234–245.

McNeal, D. R. (1976). Analysis of a model for excitation of myelinated nerve. *IEEE Transactions on Biomedical Engineering*, (4):329–337.

McNeal, J. (1975). Development and comparative anatomy of the prostate. *Benign prostatic hyperplasia*, pages 76–1113.

McNeal, J. (1984). Anatomy of the prostate and morphogenesis of BPH. *Progress in clinical and biological research*, 145:27–53.

McNeal, J. E. (1968). Regional morphology and pathology of the prostate. *American journal of clinical pathology*, 49(3):347–357.

McNeal, J. E. (1972). The prostate and prostatic urethra: A morphologic synthesis. *The Journal of urology*, 107(6):1008–1016.

McNeal, J. E. (1978). Origin and evolution of benign prostatic enlargement. *Investigative urology*, 15(4):340–345.

McNeal, J. E., Redwine, E. A., Freiha, F. S., and Stamey, T. A. (1988). Zonal distribution of prostatic adenocarcinoma: Correlation with histologic pattern and direction of spread. *The American journal of surgical pathology*, 12(12):897–906.

Mechefske, C., Yao, G., Li, W., Gazdzinski, C., and Rutt, B. (2004). Modal analysis and acoustic noise characterization of a 4T MRI gradient coil insert. *Concepts in Magnetic Resonance Part B: Magnetic Resonance Engineering: An Educational Journal*, 22(1):37–49.

Medved, M., Soylu-Boy, F. N., Karademir, I., Sethi, I., Yousuf, A., Karczmar, G. S., and Oto, A. (2014). High-resolution diffusion-weighted imaging of the prostate. *American Journal of Roentgenology*, 203(1):85–90.

Mesri, H. Y., David, S., Viergever, M. A., and Leemans, A. (2020). The adverse effect of gradient nonlinearities on diffusion MRI: From voxels to group studies. *NeuroImage*, 205:116127.

Mitra, P. P., Sen, P. N., Schwartz, L. M., and Le Doussal, P. (1992). Diffusion propagator as a probe of the structure of porous media. *Physical review letters*, 68(24):3555.

Molendowska, M., Foley, k. G., Palombo, M., Fasano, F., Jones, D. K., Alexander, D. C., Panagiotaki, E., and Tax, C. M. (2022). 300 mT/m diffusion MRI beyond the brain: Probing restricted diffusion in prostate cancer. *Proceedings of the International Society for Magnetic Resonance in Medicine, 2022. Presented at the Diffusion Workshop ISMRM*.

Morez, J., Szczepankiewicz, F., den Dekker, A. J., Vanhevel, F., Sijbers, J., and Jeurissen, B. (2022). Optimal experimental design and estimation for q-space trajectory imaging. *Human Brain Mapping*.

Morgan, P. S., Bowtell, R. W., McIntyre, D. J., and Worthington, B. S. (2004). Correction of spatial distortion in EPI due to inhomogeneous static magnetic fields using the reversed gradient method. *Journal of Magnetic Resonance Imaging: An Official Journal of the International Society for Magnetic Resonance in Medicine*, 19(4):499–507.

Mowatt, G., Scotland, G., Boachie, C., Cruickshank, M., Ford, J., Fraser, C., Kurban, L., Lam, T., Padhani, A., Royle, J., et al. (2013). The diagnostic accuracy and cost-effectiveness of magnetic resonance spectroscopy and enhanced magnetic resonance imaging techniques in aiding the localisation of prostate abnormalities for biopsy: A systematic review and economic evaluation.

Mueller, L., Afzali, M., Molendowska, M., Tax, C. M., Kleban, E., Fasano, F., Rudrapatna, S. U., and Jones, D. K. (2021). Boosting the SNR-efficiency of free gradient waveform diffusion MRI using spiral readouts and ultra-strong gradients. *Society Mag. Res. Medicine, Proceedings of the 29th Annual Meeting. Paris: Soc Mag Res in Medicine*.

Mueller, L., Wetscherek, A., Kuder, T. A., and Laun, F. B. (2017). Eddy current compensated double diffusion encoded (DDE) MRI. *Magnetic Resonance in Medicine*, 77(1):328–335.

Nezzo, M., Di Trani, M., Caporale, A., Miano, R., Mauriello, A., Bove, P., Capuani, S., and Manenti, G. (2016). Mean diffusivity discriminates between prostate cancer with grade group 1&2 and grade groups equal to or greater than 3. *European Journal of Radiology*, 85(10):1794–1801.

Nguyen, C., Sharif-Afshar, A.-R., Fan, Z., Xie, Y., Wilson, S., Bi, X., Payor, L., Saouaf, R., Kim, H., and Li, D. (2016). 3D high-resolution diffusion-weighted MRI at 3T: Preliminary application in prostate cancer patients undergoing active surveillance protocol for low-risk prostate cancer. *Magnetic resonance in medicine*, 75(2):616–626.

Nilsson, M., Eklund, G., Szczepankiewicz, F., Skorpil, M., Bryskhe, K., Westin, C.-F., Lindh, C., Blomqvist, L., and Jäderling, F. (2021). Mapping prostatic microscopic anisotropy using linear and spherical b-tensor encoding: A preliminary study. *Magnetic Resonance in Medicine*, 86(4):2025–2033.

Nilsson, M., Lasič, S., Drobnjak, I., Topgaard, D., and Westin, C.-F. (2017). Resolution limit of cylinder diameter estimation by diffusion MRI: The impact of gradient waveform and orientation dispersion. *NMR in Biomedicine*, 30(7):e3711.

Nilsson, M., Szczepankiewicz, F., van Westen, D., and Hansson, O. (2015). Extrapolation-based references improve motion and eddy-current correction of high b-value DWI data: Application in Parkinson's disease dementia. *PloS one*, 10(11):e0141825.

Novikov, D. S., Fieremans, E., Jespersen, S. N., and Kiselev, V. G. (2019). Quantifying brain microstructure with diffusion MRI: Theory and parameter estimation. *NMR in Biomedicine*, 32(4):e3998.

Palombo, M., Ianus, A., Guerreri, M., Nunes, D., Alexander, D. C., Shemesh, N., and Zhang, H. (2020a). SANDI: A compartment-based model for non-invasive apparent soma and neurite imaging by diffusion MRI. *Neuroimage*, 215:116835.

Palombo, M., Singh, S., Whitaker, H., Punwani, S., Alexander, D. C., and Panagiotaki, E. (2020b). Relaxed-VERDICT: Decoupling relaxation and diffusion for comprehensive microstructure characterization of prostate cancer. *Proc of International Society for Magnetic Resonance in Medicine (ISMRM)*.

Panagiotaki, E., Chan, R. W., Dikaios, N., Ahmed, H. U., O'Callaghan, J., Freeman, A., Atkinson, D., Punwani, S., Hawkes, D. J., and Alexander, D. C. (2015). Microstructural characterization of normal and malignant human prostate tissue with vascular, extracellular, and restricted diffusion for cytometry in tumours magnetic resonance imaging. *Investigative radiology*, 50(4):218–227.

Paquette, M., Tax, C., Eichner, C., and Anwander, A. (2020). Impact of gradient non-linearities on b-tensor diffusion encoding. In *Proc. 28th Annual Meeting of the ISMRM, Online*, page 4412.

Patzig, F., Wilm, B., and Pruessmann, K. P. (2021). Off-resonance self-correction by implicit B0-encoding. In *Proc Intl Soc Mag Res Med*.

Pierpaoli, C. (2010). Artifacts in diffusion MRI. *Diffusion MRI: theory, methods and applications*, pages 303–318.

Pierpaoli, C., Sarlls, J., Nevo, U., Basser, P. J., and Horkay, F. (2009). Polyvinylpyrrolidone (PVP) water solutions as isotropic phantoms for diffusion MRI studies. In *Proc Intl Soc Magn Reson Med*, volume 17, page 1414.

Polk, C. (1995). Biological effects of nonionizing electromagnetic fields. *Handbook of biomedical engineering*.

Poot, D. H., Jeurissen, B., Bastiaensen, Y., Veraart, J., Van Hecke, W., Parizel, P. M., and Sijbers, J. (2013). Super-resolution for multislice diffusion tensor imaging. *Magnetic resonance in medicine*, 69(1):103–113.

Priester, A., Natarajan, S., Khoshnoodi, P., Margolis, D. J., Raman, S. S., Reiter, R. E., Huang, J., Grundfest, W., and Marks, L. S. (2017). Magnetic resonance imaging underestimation of prostate cancer geometry: Use of patient specific molds to correlate images with whole mount pathology. *The Journal of urology*, 197(2):320–326.

Pruessmann, K. P., Weiger, M., Börnert, P., and Boesiger, P. (2001). Advances in sensitivity encoding with arbitrary k-space trajectories. *Magnetic Resonance in Medicine: An Official Journal of the International Society for Magnetic Resonance in Medicine*, 46(4):638–651.

Pruessmann, K. P., Weiger, M., Scheidegger, M. B., and Boesiger, P. (1999). SENSE: Sensitivity encoding for fast MRI. *Magnetic Resonance in Medicine: An Official Journal of the International Society for Magnetic Resonance in Medicine*, 42(5):952–962.

Rahmer, J., Mazurkewitz, P., Börnert, P., and Nielsen, T. (2019). Rapid acquisition of the 3D MRI gradient impulse response function using a simple phantom measurement. *Magnetic Resonance in Medicine*, 82(6):2146–2159.

Rattay, F. (1986). Analysis of models for external stimulation of axons. *IEEE Transactions on Biomedical Engineering*, (10):974–977.

Reese, T. G., Heid, O., Weisskoff, R., and Wedeen, V. (2003). Reduction of eddy-current-induced distortion in diffusion MRI using a twice-refocused spin echo. *Magnetic Resonance in Medicine: An Official Journal of the International Society for Magnetic Resonance in Medicine*, 49(1):177–182.

Reilly, J. (1989). Peripheral nerve stimulation by induced electric currents: Exposure to time-varying magnetic fields. *Medical and Biological Engineering and Computing*, 27(2):101.

Reilly, J. (1990). Peripheral nerve and cardiac excitation by time varying magnetic fields: A comparison of thresholds. *Final report Metatec MT90-100, submitted to the Food and Drug Administration*.

Reilly, J. P., Freeman, V. T., and Larkin, W. D. (1985). Sensory effects of transient electrical stimulation-evaluation with a neuroelectric model. *IEEE Transactions on Biomedical Engineering*, (12):1001–1011.

Reynaud, O. (2017). Time-dependent diffusion MRI in cancer: Tissue modeling and applications. *Frontiers in Physics*, 5:58.

Rieseberg, S., Frahm, J., and Finsterbusch, J. (2002). Two-dimensional spatially-selective RF excitation pulses in echo-planar imaging. *Magnetic Resonance in Medicine: An Official Journal of the International Society for Magnetic Resonance in Medicine*, 47(6):1186–1193.

Robison, R. K., Li, Z., Wang, D., Ooi, M. B., and Pipe, J. G. (2019). Correction of B0 eddy current effects in spiral MRI. *Magnetic resonance in medicine*, 81(4):2501–2513.

Robson, P. M., Grant, A. K., Madhuranthakam, A. J., Lattanzi, R., Sodickson, D. K., and McKenzie, C. A. (2008). Comprehensive quantification of signal-to-noise ratio and g-factor for image-based and k-space-based parallel imaging reconstructions. *Magnetic Resonance in Medicine: An Official Journal of the International Society for Magnetic Resonance in Medicine*, 60(4):895–907.

Röding, M., Bernin, D., Jonasson, J., Särkkä, A., Topgaard, D., Rudemo, M., and Nydén, M. (2012). The gamma distribution model for pulsed-field gradient NMR studies of molecular-weight distributions of polymers. *Journal of magnetic resonance*, 222:105–111.

Rudrapatna, U., Parker, G. D., Roberts, J., and Jones, D. K. (2021). A comparative study of gradient nonlinearity correction strategies for processing diffusion data obtained with ultra-strong gradient MRI scanners. *Magnetic resonance in medicine*, 85(2):1104–1113.

Sabaté, J. A., Wang, R. R., Tao, F., and Chi, S. (2015). Magnetic resonance imaging power: High-performance MVA gradient drivers. *IEEE Journal of Emerging and Selected Topics in Power Electronics*, 4(1):280–292.

Sahoo, P., Rockne, R. C., Jung, A., Gupta, P. K., Rathore, R. K., and Gupta, R. K. (2020). Synthetic Apparent Diffusion Coefficient for High b-Value Diffusion-Weighted MRI in Prostate. *Prostate cancer*, 2020.

Sairanen, V., Leemans, A., and Tax, C. M. (2018). Fast and accurate Slicewise OutLIer Detection (SOLID) with informed model estimation for diffusion MRI data. *Neuroimage*, 181:331–346.

Salomir, R., de Senneville, B. D., and Moonen, C. T. (2003). A fast calculation method for magnetic field inhomogeneity due to an arbitrary distribution of bulk susceptibility. *Concepts in Magnetic Resonance Part B: Magnetic Resonance Engineering: An Educational Journal*, 19(1):26–34.

Schaefer, D. J., Bourland, J. D., and Nyenhuis, J. A. (2000). Review of patient safety in time-varying gradient fields. *Journal of magnetic resonance imaging*, 12(1):20–29.

Schenck, J. F. (1992). Health and physiological effects of human exposure to whole-body four-tesla magnetic fields during MRI. *Annals of the New York Academy of Sciences*, 649(1):285–301.

Schenck, J. F. (2000). Safety of strong, static magnetic fields. *Journal of magnetic resonance imaging*, 12(1):2–19.

Schutter, D. J. and Hortensius, R. (2010). Retinal origin of phosphenes to transcranial alternating current stimulation. *Clinical Neurophysiology*, 121(7):1080–1084.

Schwiedrzik, C. M. (2009). Retina or visual cortex? The site of phosphene induction by transcranial alternating current stimulation. *Frontiers in integrative neuroscience*, 3:6.

Sen, P. N. (2004). Time-dependent diffusion coefficient as a probe of geometry. *Concepts in Magnetic Resonance Part A: An Educational Journal*, 23(1):1–21.

Sen, S., Valindria, V., Slator, P. J., Pye, H., Grey, A., Freeman, A., Moore, C., Whitaker, H., Punwani, S., Singh, S., et al. (2022). Differentiating false positive lesions from clinically significant cancer and normal prostate tissue using VERDICT MRI and other diffusion models.

Setsompop, K., Gagoski, B. A., Polimeni, J. R., Witzel, T., Wedeen, V. J., and Wald, L. L. (2012). Blipped-controlled aliasing in parallel imaging for simultaneous multislice echo planar imaging with reduced g-factor penalty. *Magnetic resonance in medicine*, 67(5):1210–1224.

Setsompop, K., Kimmlingen, R., Eberlein, E., Witzel, T., Cohen-Adad, J., McNab, J. A., Keil, B., Tisdall, M. D., Hoecht, P., Dietz, P., et al. (2013). Pushing the limits of in vivo diffusion MRI for the Human Connectome Project. *Neuroimage*, 80:220–233.

Shaish, H., Kang, S. K., and Rosenkrantz, A. B. (2017). The utility of quantitative ADC values for differentiating high-risk from low-risk prostate cancer: A systematic review and meta-analysis. *Abdominal Radiology*, 42(1):260–270.

Shewchuk, J. R. et al. (1994). An introduction to the conjugate gradient method without the agonizing pain.

Singh, S., Rogers, H., Kanber, B., Clemente, J., Pye, H., Johnston, E. W., Parry, T., Grey, A., Dinneen, E., Shaw, G., et al. (2022). Avoiding unnecessary biopsy after multiparametric prostate MRI with VERDICT analysis: The INNOVATE study. *Radiology*, page 212536.

Sjölund, J., Szczepankiewicz, F., Nilsson, M., Topgaard, D., Westin, C.-F., and Knutsson, H. (2015). Constrained optimization of gradient waveforms for generalized diffusion encoding. *Journal of magnetic resonance*, 261:157–168.

Slator, P. J., Hutter, J., Ianus, A., Panagiotaki, E., Rutherford, M. A., Hajnal, J. V., and Alexander, D. C. (2019). A framework for calculating time-efficient diffusion MRI protocols for anisotropic IVIM and an application in the placenta. In *International Conference on Medical Image Computing and Computer-Assisted Intervention*, pages 251–263. Springer.

Stanisz, G. J., Wright, G. A., Henkelman, R. M., and Szafer, A. (1997). An analytical model of restricted diffusion in bovine optic nerve. *Magnetic Resonance in Medicine*, 37(1):103–111.

Stehling, M. K., Turner, R., and Mansfield, P. (1991). Echo-planar imaging: Magnetic resonance imaging in a fraction of a second. *Science*, 254(5028):43–50.

Stejskal, E. O. and Tanner, J. E. (1965). Spin diffusion measurements: Spin echoes in the presence of a time-dependent field gradient. *The journal of chemical physics*, 42(1):288–292.

Storås, T. H., Gjesdal, K.-I., Gadmar, Ø. B., Geitung, J. T., and Kløw, N.-E. (2008). Prostate magnetic resonance imaging: Multiexponential T2 decay in prostate tissue. *Journal of Magnetic Resonance Imaging: An Official Journal of the International Society for Magnetic Resonance in Medicine*, 28(5):1166–1172.

Sutton, B. P., Noll, D. C., and Fessler, J. A. (2004). Dynamic field map estimation using a spiral-in/spiral-out acquisition. *Magnetic Resonance in Medicine: An Official Journal of the International Society for Magnetic Resonance in Medicine*, 51(6):1194–1204.

Szczepankiewicz, F., van Westen, D., Englund, E., Westin, C.-F., Ståhlberg, F., Lätt, J., Sundgren, P. C., and Nilsson, M. (2016). The link between diffusion MRI and tumor heterogeneity: Mapping cell eccentricity and density by diffusional variance decomposition (DIVIDE). *Neuroimage*, 142:522–532.

Szczepankiewicz, F., Westin, C.-F., and Nilsson, M. (2019). Maxwell-compensated design of asymmetric gradient waveforms for tensor-valued diffusion encoding. *Magnetic resonance in medicine*, 82(4):1424–1437.

Tan, E. T., Hua, Y., Fiveland, E. W., Vermilyea, M. E., Piel, J. E., Park, K. J., Ho, V. B., and Foo, T. K. (2020). Peripheral nerve stimulation limits of a high amplitude and slew rate magnetic field gradient coil for neuroimaging. *Magnetic Resonance in Medicine*, 83(1):352–366.

Tang, L. and Zhou, X. J. (2019). Diffusion MRI of cancer: From low to high b-values. *Journal of Magnetic Resonance Imaging*, 49(1):23–40.

Tanner, J. (1979). Self diffusion of water in frog muscle. *Biophysical journal*, 28(1):107–116.

Tao, S., Trzasko, J. D., Shu, Y., Huston III, J., and Bernstein, M. A. (2015). Integrated image reconstruction and gradient nonlinearity correction. *Magnetic resonance in medicine*, 74(4):1019–1031.

Tax, C. M., Bastiani, M., Veraart, J., Garyfallidis, E., and Irfanoglu, M. O. (2022). What's new and what's next in diffusion MRI preprocessing. *NeuroImage*, 249:118830.

Tax, C. M., Szczepankiewicz, F., Nilsson, M., and Jones, D. K. (2020). The dot-compartment revealed? Diffusion MRI with ultra-strong gradients and spherical tensor encoding in the living human brain. *NeuroImage*, page 116534.

Thompson, J., Van Leeuwen, P., Moses, D., Shnier, R., Brenner, P., Delprado, W., Pulbrook, M., Böhm, M., Haynes, A. M., Hayen, A., et al. (2016). The diagnostic performance of multiparametric magnetic resonance imaging to detect significant prostate cancer. *The Journal of urology*, 195(5):1428–1435.

Tong, A., Lemberskiy, G., Huang, C., Shanbhogue, K., Feiweier, T., and Rosenkrantz, A. B. (2019). Exploratory study of geometric distortion correction of prostate diffusion-weighted imaging using B0 map acquisition. *Journal of Magnetic Resonance Imaging*, 50(5):1614–1619.

Topgaard, D. (2017). Multidimensional diffusion MRI. *Journal of magnetic resonance*, 275:98–113.

Turkbey, B., Rosenkrantz, A. B., Haider, M. A., Padhani, A. R., Villeirs, G., Macura, K. J., Tempany, C. M., Choyke, P. L., Cornud, F., Margolis, D. J., et al. (2019). Prostate imaging reporting and data system version 2.1: 2019 update of prostate imaging reporting and data system version 2. *European urology*, 76(3):340–351.

Turner, R. (1986). A target field approach to optimal coil design. *Journal of physics D: Applied physics*, 19(8):L147.

Usman, M., Kakkar, L., Kirkham, A., Arridge, S., and Atkinson, D. (2019). Model-based reconstruction framework for correction of signal pile-up and geometric distortions in prostate diffusion MRI. *Magnetic resonance in medicine*, 81(3):1979–1992.

Usman, M., Kakkar, L., Matakos, A., Kirkham, A., Arridge, S., and Atkinson, D. (2020). Joint B0 and image estimation integrated with model based reconstruction for field map update and distortion correction in prostate diffusion MRI. *Magnetic resonance imaging*, 65:90–99.

Valsamis, J. J., Dubovan, P. I., and Baron, C. A. (2022). Characterization and correction of time-varying eddy currents for diffusion MRI. *Magnetic Resonance in Medicine*, 87(5):2209–2223.

van der Leest, M., Cornel, E., Israël, B., Hendriks, R., Padhani, A. R., Hoogenboom, M., Zamecnik, P., Bakker, D., Setiasti, A. Y., Veltman, J., et al. (2019). Head-to-head comparison of

transrectal ultrasound-guided prostate biopsy versus multiparametric prostate resonance imaging with subsequent magnetic resonance-guided biopsy in biopsy-naive men with elevated prostate-specific antigen: A large prospective multicenter clinical study. *European urology*, 75(4):570–578.

van Gorkum, R. J., Guenthner, C., Koethe, A., Stoeck, C. T., and Kozerke, S. (2022). Characterization and correction of diffusion gradient-induced eddy currents in second-order motion-compensated echo-planar and spiral cardiac DTI. *Magnetic Resonance in Medicine*, 88(6):2378–2394.

van Houdt, P. J., Ghobadi, G., Schoots, I. G., Heijmink, S. W., de Jong, J., van der Poel, H. G., Pos, F. J., Rylander, S., Bentzen, L., Haustermans, K., et al. (2020). Histopathological features of MRI-invisible regions of prostate cancer lesions. *Journal of Magnetic Resonance Imaging*, 51(4):1235–1246.

Van Steenkiste, G., Jeurissen, B., Veraart, J., Den Dekker, A. J., Parizel, P. M., Poot, D. H., and Sijbers, J. (2016). Super-resolution reconstruction of diffusion parameters from diffusion-weighted images with different slice orientations. *Magnetic resonance in medicine*, 75(1):181–195.

Van Vaals, J. and Bergman, A. (1990). Optimization of eddy-current compensation. *Journal of Magnetic Resonance (1969)*, 90(1):52–70.

Vannesjo, S. J., Graedel, N. N., Kasper, L., Gross, S., Busch, J., Haeberlin, M., Barmet, C., and Pruessmann, K. P. (2016). Image reconstruction using a gradient impulse response model for trajectory prediction. *Magnetic resonance in medicine*, 76(1):45–58.

Vannesjo, S. J., Haeberlin, M., Kasper, L., Pavan, M., Wilm, B. J., Barmet, C., and Pruessmann, K. P. (2013). Gradient system characterization by impulse response measurements with a dynamic field camera. *Magnetic resonance in medicine*, 69(2):583–593.

Vargas, H. A., Akin, O., Franiel, T., Mazaheri, Y., Zheng, J., Moskowitz, C., Udo, K., Eastham, J., and Hricak, H. (2011). Diffusion-weighted endorectal MR imaging at 3T for prostate cancer: Tumor detection and assessment of aggressiveness. *Radiology*, 259(3):775.

Veraart, J., Sijbers, J., Sunaert, S., Leemans, A., and Jeurissen, B. (2013). Weighted linear least squares estimation of diffusion MRI parameters: Strengths, limitations, and pitfalls. *Neuroimage*, 81:335–346.

Veraart, J., Van Hecke, W., and Sijbers, J. (2011). Constrained maximum likelihood estimation of the diffusion kurtosis tensor using a Rician noise model. *Magnetic resonance in medicine*, 66(3):678–686.

Versteeg, E., van der Velden, T., Hendrikse, J., Klomp, D., and Siero, J. (2020). Dual axis gradient insert for supersonic MRI. *Society Mag. Res. Medicine, Proceedings of the 29th Annual Meeting. Paris: Soc Mag Res in Medicine*.

Versteeg, E., van der Velden, T. A., van Leeuwen, C. C., Borgo, M., Huijing, E. R., Hendriks, A. D., Hendrikse, J., Klomp, D. W., and Siero, J. C. (2021). A plug-and-play, lightweight, single-axis gradient insert design for increasing spatiotemporal resolution in echo planar imaging-based brain imaging. *NMR in Biomedicine*, page e4499.

Vis, G., Nilsson, M., Westin, C.-F., and Szczepankiewicz, F. (2021). Accuracy and precision in super-resolution MRI: Enabling spherical tensor diffusion encoding at ultra-high b-values and high resolution. *NeuroImage*, 245:118673.

Wagner, F., Laun, F. B., Kuder, T. A., Mlynarska, A., Maier, F., Faust, J., Demberg, K., Lindemann, L., Rivkin, B., Nagel, A. M., et al. (2017). Temperature and concentration calibration of aqueous polyvinylpyrrolidone (PVP) solutions for isotropic diffusion MRI phantoms. *PloS one*, 12(6):e0179276.

Wang, L., Lu, B., He, M., Wang, Y., Wang, Z., and Du, L. (2022). Prostate cancer incidence and mortality: Global status and temporal trends in 89 countries from 2000 to 2019. *Frontiers in Public Health*, 10:811044.

Wang, Z., Bovik, A. C., Sheikh, H. R., and Simoncelli, E. P. (2004). Image quality assessment: From error visibility to structural similarity. *IEEE transactions on image processing*, 13(4):600–612.

Webb, A. G. (2016). *Magnetic resonance technology: Hardware and system component design*. Royal Society of Chemistry.

Webster, K. and Ro, T. (2017). Retinal and visual cortex distance from transcranial magnetic stimulation of the vertex affects phosphene perception. *Experimental brain research*, 235(9):2857–2866.

Weiger, M., Overweg, J., Rösler, M. B., Froidevaux, R., Hennel, F., Wilm, B. J., Penn, A., Sturzenegger, U., Schuth, W., Mathlener, M., et al. (2018). A high-performance gradient insert for rapid and short-T2 imaging at full duty cycle. *Magnetic resonance in medicine*, 79(6):3256–3266.

Weinreb, J. C., Barentsz, J. O., Choyke, P. L., Cornud, F., Haider, M. A., Macura, K. J., Margolis, D., Schnall, M. D., Shtern, F., Tempany, C. M., et al. (2016). PI-RADS prostate imaging–reporting and data system: 2015, version 2. *European urology*, 69(1):16–40.

Weintraub, M. I., Khoury, A., and Cole, S. P. (2007). Biologic effects of 3 Tesla (T) MR imaging comparing traditional 1.5 T and 0.6 T in 1023 consecutive outpatients. *Journal of Neuroimaging*, 17(3):241–245.

Weiss, G. (1901). Sur la possibilite de rendre comparables entre eux les appareils servant a l'excitation electrique. *Archives Italiennes de Biologie*, 35:413–446.

Westin, C.-F., Knutsson, H., Pasternak, O., Szczepankiewicz, F., Özarslan, E., van Westen, D., Mattisson, C., Bogren, M., O'Donnell, L. J., Kubicki, M., et al. (2016). Q-space trajectory imaging for multidimensional diffusion MRI of the human brain. *Neuroimage*, 135:345–362.

While, P. T., Forbes, L. K., and Crozier, S. (2010). Calculating temperature distributions for gradient coils. *Concepts in Magnetic Resonance Part B: Magnetic Resonance Engineering*, 37(3):146–159.

While, P. T., Poole, M. S., Forbes, L. K., and Crozier, S. (2013). Minimum maximum temperature gradient coil design. *Magnetic Resonance in Medicine*, 70(2):584–594.

WHO et al. (2006). Environmental health criteria 232. Static fields. *World Health Organization: Geneva, Switzerland*.

Wilm, B. J., Barmet, C., Pavan, M., and Pruessmann, K. P. (2011). Higher order reconstruction for MRI in the presence of spatiotemporal field perturbations. *Magnetic resonance in medicine*, 65(6):1690–1701.

Wilm, B. J., Nagy, Z., Barmet, C., Vannesjo, S. J., Kasper, L., Haeberlin, M., Gross, S., Dietrich, B. E., Brunner, D. O., Schmid, T., et al. (2015). Diffusion MRI with concurrent magnetic field monitoring. *Magnetic resonance in medicine*, 74(4):925–933.

Winkler, S. A., Schmitt, F., Landes, H., de Bever, J., Wade, T., Alejski, A., and Rutt, B. K. (2018). Gradient and shim technologies for ultra high field MRI. *NeuroImage*, 168:59–70.

Wu, D., Jiang, K., Li, H., Zhang, Z., Ba, R., Zhang, Y., Hsu, Y.-C., Sun, Y., and Zhang, Y.-D. (2022). Time-dependent diffusion MRI for quantitative microstructural mapping of prostate cancer. *Radiology*, 303(3):578–587.

Wu, L.-M., Zhou, B., Lu, Q., Suo, S.-T., Liu, Q., Hu, J., Haccke, E., Chen, X.-X., and Xu, J.-R. (2016). T2* relaxation time in the detection and assessment of aggressiveness of peripheral zone cancer in comparison with diffusion-weighted imaging. *Clinical Radiology*, 71(4):356–362.

Wu, Y., Chronik, B. A., Bowen, C., Mechefske, C. K., and Rutt, B. K. (2000). Gradient-induced acoustic and magnetic field fluctuations in a 4T whole-body MR imager. *Magnetic resonance in medicine*, 44(4):532–536.

Yamasaki, F., Kurisu, K., Satoh, K., Arita, K., Sugiyama, K., Ohtaki, M., Takaba, J., Tominaga, A., Hanaya, R., Yoshioka, H., et al. (2005). Apparent diffusion coefficient of human brain tumors at MR imaging. *Radiology*, 235(3):985–991.

Yang, G. and McNab, J. A. (2019). Eddy current nulled constrained optimization of isotropic diffusion encoding gradient waveforms. *Magnetic resonance in medicine*, 81(3):1818–1832.

Yoshikawa, M. I., Ohsumi, S., Sugata, S., Kataoka, M., Takashima, S., Mochizuki, T., Ikura, H., and Imai, Y. (2008). Relation between cancer cellularity and apparent diffusion coefficient values

using diffusion-weighted magnetic resonance imaging in breast cancer. *Radiation medicine*, 26(4):222–226.

Zahneisen, B., Hugger, T., Lee, K. J., LeVan, P., Reisert, M., Lee, H.-L., Assländer, J., Zaitsev, M., and Hennig, J. (2012). Single shot concentric shells trajectories for ultra fast fMRI. *Magnetic resonance in medicine*, 68(2):484–494.

Zelhof, B., Pickles, M., Liney, G., Gibbs, P., Rodrigues, G., Kraus, S., and Turnbull, L. (2009). Correlation of diffusion-weighted magnetic resonance data with cellularity in prostate cancer. *BJU international*, 103(7):883–888.

Zhang, L., Tang, M., Chen, S., Lei, X., Zhang, X., and Huan, Y. (2017a). A meta-analysis of use of Prostate Imaging Reporting and Data System Version 2 (PI-RADS V2) with multiparametric MR imaging for the detection of prostate cancer. *European radiology*, 27(12):5204–5214.

Zhang, Q., Coolen, B. F., Versluis, M. J., Strijkers, G. J., and Nederveen, A. J. (2017b). Diffusion-prepared stimulated-echo turbo spin echo (DPsti-TSE): An eddy current-insensitive sequence for three-dimensional high-resolution and undistorted diffusion-weighted imaging. *NMR in Biomedicine*, 30(7):e3719.

Zhang, Z., Wu, H. H., Priester, A., Magyar, C., Afshari Mirak, S., Shakeri, S., Mohammadian Bajgiran, A., Hosseiny, M., Azadikhah, A., Sung, K., et al. (2020). Prostate microstructure in prostate cancer using 3-T MRI with diffusion-relaxation correlation spectrum imaging: Validation with whole-mount digital histopathology. *Radiology*, 296(2):348–355.